X-33 Computational Aeroheating/Aerodynamic Predictions and Comparisons With Experimental Data

Brian R. Hollis, Richard A. Thompson, Scott A. Berry, Thomas J. Horvath, Kelly J. Murphy,
Robert J. Nowak, and Stephen J. Alter
Langley Research Center, Hampton, Virginia

The NASA STI Program Office . . . in Profile

Since its founding, NASA has been dedicated to the advancement of aeronautics and space science. The NASA Scientific and Technical Information (STI) Program Office plays a key part in helping NASA maintain this important role.

The NASA STI Program Office is operated by Langley Research Center, the lead center for NASA's scientific and technical information. The NASA STI Program Office provides access to the NASA STI Database, the largest collection of aeronautical and space science STI in the world. The Program Office is also NASA's institutional mechanism for disseminating the results of its research and development activities. These results are published by NASA in the NASA STI Report Series, which includes the following report types:

- TECHNICAL PUBLICATION. Reports of completed research or a major significant phase of research that present the results of NASA programs and include extensive data or theoretical analysis. Includes compilations of significant scientific and technical data and information deemed to be of continuing reference value. NASA counterpart of peer-reviewed formal professional papers, but having less stringent limitations on manuscript length and extent of graphic presentations.

- TECHNICAL MEMORANDUM. Scientific and technical findings that are preliminary or of specialized interest, e.g., quick release reports, working papers, and bibliographies that contain minimal annotation. Does not contain extensive analysis.

- CONTRACTOR REPORT. Scientific and technical findings by NASA-sponsored contractors and grantees.

- CONFERENCE PUBLICATION. Collected papers from scientific and technical conferences, symposia, seminars, or other meetings sponsored or co-sponsored by NASA.

- SPECIAL PUBLICATION. Scientific, technical, or historical information from NASA programs, projects, and missions, often concerned with subjects having substantial public interest.

TECHNICAL TRANSLATION. English-language translations of foreign scientific and technical material pertinent to NASA's mission.

Specialized services that complement the STI Program Office's diverse offerings include creating custom thesauri, building customized databases, organizing and publishing research results . . . even providing videos.

For more information about the NASA STI Program Office, see the following:

- Access the NASA STI Program Home Page at *http://www.sti.nasa.gov*

- Email your question via the Internet to help@sti.nasa.gov

- Fax your question to the NASA STI Help Desk at (301) 621-0134

- Telephone the NASA STI Help Desk at (301) 621-0390

- Write to:
  NASA STI Help Desk
  NASA Center for AeroSpace Information
  7121 Standard Drive
  Hanover, MD 21076-1320

X-33 Computational Aeroheating/Aerodynamic Predictions and Comparisons With Experimental Data

Brian R. Hollis, Richard A. Thompson, Scott A. Berry, Thomas J. Horvath, Kelly J. Murphy, Robert J. Nowak, and Stephen J. Alter
Langley Research Center, Hampton, Virginia

May 2003

Acknowledgments

Contents

List of Tables

List of Figures

vi

Abstract

This report details a computational fluid dynamics study conducted in support of the phase II development of the X-33 vehicle. Aerodynamic and aeroheating predictions were generated for the X-33 vehicle at both flight and wind-tunnel test conditions using two finite-volume, Navier-Stokes solvers. Aerodynamic computations were performed at Mach 6 and Mach 10 wind-tunnel conditions for angles of attack from 10° to 50° with body-flap deflections of 0° to 20°. Additional aerodynamic computations were performed over a parametric range of free-stream conditions at Mach numbers of 4 to 10 and angles of attack from 10° to 50°. Laminar and turbulent wind-tunnel aeroheating computations were performed at Mach 6 for angles of attack of 20° to 40° with body-flap deflections of 0° to 20°. Aeroheating computations were performed at four flight conditions with Mach numbers of 6.6 to 8.9 and angles of attack of 10° to 40°. Surface heating and pressure distributions, surface streamlines, flow field information, and aerodynamic coefficients from these computations are presented, and comparisons are made with wind-tunnel data.

Introduction

The Access to Space Study conducted by NASA recommended the development of a fully Reusable Launch Vehicle (RLV) to provide a next-generation launch capability at greatly reduced cost (refs. 1–4). This recommendation led to the RLV/X-33 technology program, an industry-led effort in which NASA was a main partner. The X-33 was to serve as a subscale technology demonstrator for a full-scale Single-Stage-to-Orbit (SSTO) RLV. Following a phase I industry competition among several aerospace companies, the Lockheed-Martin lifting-body concept was selected by NASA for award of the phase II contract to design, develop, and construct an X-33 flight vehicle. The Lockheed-Martin X-33 design (ref. 5), shown in figure 1, is a subscale version of an RLV and incorporates a delta-shape lifting-body planform, symmetric canted fins, twin vertical tails and dual body flaps for aerodynamic control, and a linear aerospike engine for propulsion. The X-33 was intended to prove the feasibility of the SSTO-RLV concept through demonstration of key design and operational aspects of the vehicle; however, technical and cost concerns led to the termination of the project in 2001. The purpose of this report is to archive X-33 computational aeroheating and aerodynamic data generated at Langley Research Center (LaRC) during the X-33 program and document lessons learned for future reference.

As part of the X-33 industry-government partnership, LaRC was tasked to provide aerodynamic performance data, surface aeroheating distributions, and boundary-layer transition correlations to Lockheed-Martin to support phase II aerodynamic and aerothermodynamic design and development. In order to provide these data, a synergistic experimental/computational research program was conducted. Early results from the LaRC X-33 research program are found in references 6 and 7. In those works, data from preliminary phase II aeroheating wind-tunnel tests were presented and compared with laminar and turbulent predictions generated using both a Navier-Stokes solver and a boundary-layer engineering code. These early results were used to formulate and support the use of Re_θ/M_e criteria for predicting transition onset on the X-33 or the full-scale RLV in flight. Subsequently, additional wind-tunnel tests and computations were performed to supplement the original database with more detailed results and to accommodate design changes to the original X-33 configuration. Key results of this work have been summarized in papers by Berry, Hollis, Horvath, Murphy, and Thompson (refs. 8–14).

In the present paper, laminar and turbulent Navier-Stokes predictions for the aeroheating environment of the X-33 configuration at hypersonic wind-tunnel test conditions are presented and compared with experimental data from references 8, 9, and 12.

Computational issues including grid resolution and adaption, turbulence modeling, and inviscid flux formulations are also discussed. Aeroheating environment computations for selected flight conditions are also presented. Predicted aerodynamic coefficients for wind-tunnel conditions are compared with experimental data from reference 13, and aerodynamic predictions are presented for a parametric range of Mach numbers and angles of attack.

Symbols

A^+ constant in Baldwin-Lomax model

$(A^+)_{comp}$ variable in Baldwin-Lomax model

B_{ref} reference wing span, m

C_A axial force coefficient

C_{CP} constant in Baldwin-Lomax model, 1.6

C_D drag coefficient

C_{KLEB} constant in Baldwin-Lomax model, 0.3

C_L lift coefficient

C_N normal force coefficient

C_m pitching moment coefficient

D damping factor in Baldwin-Lomax model

F vorticity function in Baldwin-Lomax model

F_{KLEB} Klebanoff's intermittency factor

H_{AW} adiabatic wall enthalpy, J/kg

H_w wall enthalpy, J/kg

H_0 total enthalpy, J/kg

h heat transfer coefficient, kg/m^2/s, $h = \dot{q}/(H_{AW} - H_w)$

h_{FR} Fay-Riddell heating coefficient, kg/m^2/s

K_v von Karman constant, 0.4

L, L_{ref} reference length, m

L/D lift-to-drag ratio

l_{mix} mixing length, m

M Mach number

M_e edge Mach number

M_∞ free-stream Mach number

n normal distance from wall, m

n^+ normalized coordinate parameter

$p_{0,2}$ pitot pressure, N/m^2

p_∞ free-stream pressure, N/m^2

$\dot{q}$ heat transfer rate, W/m^2

R nose radius, m

Re_∞ free-stream unit Reynolds number, 1/m or 1/ft

Re_L free-stream Reynolds number based on body length

Re_θ momentum thickness Reynolds number

S_{ref} reference area, m^2

T_∞ free-stream temperature, K

U_∞ free-stream velocity, m/s

u,v,w Cartesian velocity components

X,Y,Z coordinate system, m

α angle of attack, deg

δ_{BF} body-flap deflection, deg

μ laminar viscosity, kg/m/s

$\mu_{t,i}$ inner-layer eddy viscosity, kg/m/s

$\mu_{t,o}$	outer-layer eddy viscosity, kg/m/s
ρ_∞	free-stream density, kg/m^3
τ	shear stress, kg/m/s^2
ω	vorticity, 1/s

Subscripts

AW	adiabatic wall
BF	body flap
comp	compressible
FR	Fay-Riddell
max	maximum
min	minimum
n	nose
ref	reference
w	wall
∞	free stream

Abbreviations

CCD	charge coupled device
CFD	computational fluid dynamics
C.G.	center of gravity
GASP	General Aerodynamic Simulation Program
LAURA	Langley Aerothermodynamic Upwind Relaxation Algorithm
RLV	Reusable Launch Vehicle
SSTO	Single-Stage-to-Orbit
TPS	thermal protection system
TVD	total variation diminishing
UV	ultraviolet
VGM	Volume Grid Manipulator

Vehicle Geometry

The X-33 has a lifting-body delta planform, twin vertical tails, canted fins, and body flaps, and is powered by two linear aerospike engines (fig. 2). Configuration evolution from the phase I design to the most recent phase II design is discussed in references 7 and 12. Computational results presented in this paper are based on the F-Loft, Rev-F configuration (Lockheed designation 604B002F), which has a length of 19.3 m (63.2 ft) and a maximum span across the canted fins of 23.2 m (76.1 ft). The sweep of the delta planform is 70°, and the cant of the fins is 20° with a 40.2° sweep and −8.58° incidence angle. Reference dimensions for aerodynamic coefficients are listed in table 1.

Experimental results referenced in this paper were obtained with the F-Loft, Rev-F and F-Loft, Rev-G (Lockheed designation 604B0002G) configurations. The Rev-G configuration is identical to the Rev-F configuration except for the addition of small protrusions on the leeward surface near the vertical fins to accommodate internal configuration modifications and slight changes to the fillets between the body and canted fins. The configuration differences between Rev-F and Rev-G should have little or no effect on the hypersonic characteristics discussed in this work.

Computational Methods

Numerical Algorithms

Two Navier-Stokes codes, GASP (General Aerodynamic Simulation Program) v. 3.2.3 and LAURA (Langley Aerothermodynamic Upwind Relaxation Algorithm) v. 4.4, were employed in this study to predict the aerodynamic and aeroheating characteristics of the X-33 vehicle. Laminar, perfect-gas computations were performed at wind-tunnel test conditions using both codes, and additional turbulent, perfect-gas wind-tunnel computations were performed with GASP. Both codes were used to generate aeroheating results for flight conditions. For flight cases, GASP was run in a laminar equilibrium mode and LAURA was run in a laminar nonequilibrium mode.

Additionally, GASP was run in a laminar, perfect-gas mode for a series of computations in a parametric M-α space.

The GASP code is a three-dimensional, finite-volume Navier-Stokes solver that incorporates numerous flux formulations, thermochemical models, turbulence models, and time integration methods (ref. 15). The Jacobi scheme was used for time integration. As will be detailed in a later section, a third-order, upwind biased, min-mod limited scheme, which consisted of a Roe flux formulation (ref. 16) in the body-normal direction and a van Leer formulation (ref. 17) in the other two directions, was employed to represent the inviscid fluxes. Full viscous terms were retained for all three directions and modeled with second-order central differences. The turbulent computations were performed using the algebraic Baldwin-Lomax model (ref. 18) with the pressure gradient and compressibility corrections detailed in references 19 and 20, and the entire flow field was treated as turbulent.

The LAURA code is a three-dimensional Navier-Stokes solver that includes perfect-gas, equilibrium, and nonequilibrium air models (refs. 21 and 22). Time integration is carried out through a point-relaxation scheme. Roe averaging with Harten's entropy fix (ref. 23) and Yee's Symmetric Total Variation Diminishing limiter (ref. 24) is used for inviscid fluxes and a second-order scheme is employed for viscous fluxes.

Free-Stream and Boundary Conditions

Free-stream conditions for the flight cases were taken from the Michael 9A-8 trajectory, which was current at the time this work was performed. This trajectory is shown in figure 3. Case 1 corresponds to the peak heating point on the trajectory (for a laminar reference hemisphere), while cases 2–4 match the angles of attack at which the wind-tunnel aeroheating tests were performed. The free-stream conditions for these cases are listed in table 2. For these flight cases, a radiative equilibrium temperature wall boundary condition with an emissivity of 0.85 was specified. For the LAURA nonequilibrium flight computations, a fully catalytic wall boundary condition was used.

Wind-tunnel cases were run at various angles of attack at representative operating conditions of the

Langley 20-Inch Mach 6 Air Tunnel and Langley 31-Inch Mach 10 Air Tunnel. These conditions are listed in table 3. Note that Reynolds numbers are listed in English units in addition to metric as these units are commonly used to refer to the operating points of the tunnels. For the wind-tunnel cases, a uniform, ambient 300 K wall temperature boundary condition was imposed. The use of a constant wall temperature is valid because the experimental and computational heating results are reported in terms of a nondimensional heat transfer ratio h/h_{FR}, which takes into account surface temperature variations with time; the surface temperature rise during a wind-tunnel run is not large enough to affect the flow field.

Computations were also performed across a parametric M-α space in order to investigate the effects of these variables upon the aerodynamic performance of the X-33. The parametric space encompassed Mach numbers of 4.0 to 10.0 and angles of attack of 10° to 50°. The Reynolds number was fixed at 6.59×10^6/m (2.01×10^6/ft) while free-stream temperatures were obtained by interpolating between the nominal operating temperatures of the Mach 6 and Mach 10 wind tunnels. Free-stream conditions for these cases are listed in table 4, and the uniform 300 K wall temperature boundary condition was again imposed on the computations.

Grid Generation, Resolution, and Adaptation

A single-block grid that excluded the engine and wake and a multiple-block, full-wake grid (1 block around the vehicle and 15 blocks around the engines and wake) were generated for X-33 computations (ref. 25). Three grid scales were employed: a full-scale grid for the flight cases and 0.007- and 0.0132-scale grids for wind-tunnel cases to match the wind-tunnel test model sizes. The single-block grids were used for all cases reported herein except for a single case to check the influence of the wake on the computed aerodynamic coefficients. The nominal resolution of the single-block grid was $127 \times 181 \times 65$ (streamwise $\times$ circumferential $\times$ body normal) points, although grids with higher or lower resolution were also employed for various cases.

The nominal grid resolution of $127 \times 181 \times 65$ was determined to produce acceptable results for laminar wind-tunnel heating computations through a grid

resolution study in which solutions were computed on grids with the nominal point density, one-half the nominal resolution in all directions ($64 \times 91 \times 33$) and one-quarter the nominal resolution in the circumferential and normal directions with one-sixth the streamwise resolution ($22 \times 46 \times 17$). Grid resolution results were generated with GASP using the hybrid van Leer-Roe flux splitting scheme with min-mod limiting discussed subsequently. The free-stream conditions were those of the Mach 6, $Re_\infty = 4.0 \times 10^6$/ft wind-tunnel case with a 30° angle of attack. Heating distributions along the centerline and at three different axial stations obtained on the different grids are shown in figures 4–7. The heating was observed to decrease by approximately 10 to 20 percent from the coarse grid to the intermediate grid, and by 5 to 8 percent from the intermediate grid to the fine grid. These results suggest that doubling the resolution of the fine grid would only produce a 2- to 3-percent drop in the computed heating, and therefore use of the current fine grid ($127 \times 181 \times 65$) is an acceptable compromise between accuracy and computational time and memory requirements.

The nominal $127 \times 181 \times 65$-point grid was used for all laminar wind-tunnel aeroheating and aerodynamic GASP computations. For turbulent wind-tunnel computations with GASP, the body-normal direction grid-point resolution was doubled to produce a $127 \times 181 \times 129$-point grid. LAURA wind-tunnel and flight computations were performed prior to this grid resolution study on a $254 \times 181 \times 65$-point grid. For the GASP flight cases, the grid resolution was decreased to $64 \times 91 \times 65$ points to offset the increased computational demands of the equilibrium chemistry modeling. Finally, as aerodynamic parameters can be expected to be less sensitive to grid resolution than aeroheating parameters, the parametric M-α study of X-33 aerodynamics was carried out on the intermediate $64 \times 91 \times 33$-point grid.

For each computation, grid adaption was performed to align the outer boundary of the grid with the bow shock and to cluster points in the wall boundary layer. Typically, the outer boundary was adjusted so that the shock was located at approximately 80 percent of the distance from the wall to the outer boundary of the grid. Approximately 50 percent of the normal grid points were clustered in or near the wall boundary layer, and the wall cell Reynolds number was set in

the range of 10 to 20. These grid manipulations were performed using the scheme described in reference 22, and additional grid quality refinement and smoothing was carried out with the Volume Grid Manipulator (VGM) code (ref. 26).

Inviscid Flux Splitting, Formulation, and Limiting

The numerical formulation of the inviscid flux terms in LAURA is fixed (Roe flux with Harten entropy fix and Yee's symmetric total variation limiting) and has been demonstrated to produce good comparisons with experimental data (refs. 27–29). The GASP code offers numerous choices for flux representations, limiters, and integration schemes, but little information is available on the suitability of the various options for viscous, hypersonic flow field computations. Therefore, an investigation of several different inviscid flux formulations and limiters was performed in order to determine which methods produced the best results for a complex, three-dimensional configuration such as the X-33.

The first step of this investigation was to run test cases on the X-33 geometry with various combinations of the Roe, van Leer, and Roe-Harten flux formulations. The test cases were: van Leer flux in all three computational directions (referred to as the VLVLVL case), Roe flux in the normal direction with van Leer in the other two directions (VLVLRo), Roe-Harten flux in the normal direction with van Leer in the other two directions (VLVLRH), Roe flux in all directions (RoRoRo), and Roe-Harten flux in the normal direction with the Roe scheme in the other two directions (RoRoRH). The test cases were all run on the nominal $127 \times 181 \times 65$-point grid using Jacobi integration and the min-mod total variation diminishing (TVD) limiter. The test condition was the Mach 6, $Re_\infty = 4.0 \times 10^6$/ft wind-tunnel case with a 40° angle of attack for which the laminar, perfect-gas options in GASP were employed.

A comparison of windward centerline heating distributions generated with each option is presented in figure 8. The choice of flux functions can be seen to have a large influence on surface heating computations. The use of Roe's flux in the normal direction is known to produce numerical instabilities around the stagnation region, which can be seen in the

discontinuous heating distribution near the nose for the RoRoRo case. Harten's correction in the RoRoRH method dampens out the numerical instability but introduces excessive dissipation that elevates the heating rates. (It should be noted that the Roe-Harten implementation in GASP is not the same as that in LAURA; in LAURA, the Harten entropy correction has been further modified to produce less dissipation, as documented in ref. 21.) The three cases run with van Leer's flux (VLVLVL, VLVLRH, and VLVLRo) all produced smooth solutions with varying amounts of numerical dissipation depending on the normal direction flux. Of the options employed, the case with the Roe flux in the normal direction and van Leer in the other directions (VLVLRo) produced the smoothest distribution with the least dissipation (i.e., produced the lowest heating rates) and is thus assumed to be the best solution method of the options available in GASP. The assumption will be verified subsequently when heating predictions generated using the VLVLRo method are compared with experimental data.

After establishing that the VLVLRo method produces the best results, the influence of the TVD limiters on the solution was investigated. Additional cases were run using the VLVLRo scheme with the Superbee (ref. 30) and Chakravarthy-Osher (ref. 31) limiters in place of the min-mod limiter in the body-normal direction. As shown in figure 9, the magnitude of the centerline heating distributions showed much less sensitivity to the limiter than was observed for the flux formulations. However, both the Superbee and Chakravarthy-Osher limiter solutions showed a lack of smoothness along the body. It was therefore concluded that the VLVLRo scheme with min-mod limiting would be used for subsequent GASP computations.

Subsequent to the completion of this research, it was shown that the min-mod limiter implementation in the version of GASP employed in this research (3.2.x) differs from that in previous versions (ref. 32). The change in the limiter was made in order to provide more computational stability, but it did so by adding more dissipation to the computation, which could then cause an increase in the computed heating levels. When the min-mod limiter is used with the van Leer inviscid flux, which is inherently more dissipative than the Roe flux, the combination of the two sources

of dissipation can produce very high heating levels. This dissipation was probably the reason for the high heating levels presented in figure 8 for the VLVLVL scheme; in contrast, other studies (e.g., ref. 33) have shown good agreement with experimental data when using the VLVLVL scheme with earlier versions of GASP.

Turbulence Modeling

Turbulent aeroheating computations were performed for the Mach 6 wind-tunnel test conditions using the GASP code. The existing Baldwin-Lomax model in the GASP code is a subsonic, incompressible formulation, and so therefore it was modified for the present hypersonic, compressible flow computations.

The Baldwin-Lomax model (ref. 18) is an algebraic formulation that consists of a two-layer representation of the eddy viscosity. The inner-layer viscosity is given by

$$\mu_{t,i} = \rho l_{\text{mix}}^2 |\omega| \tag{1}$$

The thin-shear layer approximation for vorticity is used:

$$|\omega| = \sqrt{\left(\frac{dw}{dn}\right)^2 + \left(\frac{du}{dn}\right)^2} \tag{2}$$

and the mixing length l_{mix} is given by

$$l_{\text{mix}} = K_v n D \tag{3}$$

where $K_v = 0.4$ is the von Karman constant. The damping factor D is given by

$$D = 1 - \exp\left(\frac{n^+}{A^+}\right) \tag{4}$$

A^+ has a constant value of 26, and the normal coordinate parameter, n^+, is given by

$$n^+ = \frac{n\sqrt{\rho_w \tau_w}}{\mu_w} \tag{5}$$

where

$$\tau_w = \mu_w |\omega_w| \tag{6}$$

The outer-layer viscosity is given by

$$\mu_{t,0} = 0.0168 \rho C_{CP} F_{\max} n_{\max} F_{\text{KLEB}} \qquad (7)$$

where $C_{CP} = 1.6$, $n_{\max}$ is the location of the maximum value $F_{\max}$ of the vorticity function F,

$$F = n|\omega|D \qquad (8)$$

and F_{KLEB} is Klebanoff's intermittency factor:

$$F_{\text{KLEB}} = \left[1 + 5.5\left(\frac{C_{\text{KLEB}}n}{n_{\max}}\right)^6 \right]^{-1} \qquad (9)$$

with the constant $C_{\text{KLEB}} = 0.3$.

As detailed in references 19 and 20, the Baldwin-Lomax model can be modified for compressible, hypersonic flows through the use of local, instead of the wall values in equation (5), to give

$$(n^+)_{\text{comp}} = \frac{n\sqrt{\rho \tau_w}}{\mu} \qquad (10)$$

and the constant A^+ in equation (4) is replaced with the expression

$$(A^+)_{\text{comp}} = 26\left(\left|\frac{\tau_w}{\tau}\right|\right)^{0.5} \qquad (11)$$

with the local shear stress given by

$$\tau = (\mu + \mu_t)|\omega| \qquad (12)$$

After implementing these modifications, they were checked by performing turbulent computations for one of the test cases used in reference 19: a 9° blunt cone at hypersonic speeds (ref. 34). The aeroheating predictions were in very close agreement with the experimental data, as shown in figure 10.

Experimental Methods

Background

The data from the wind-tunnel tests that complement this computational study are presented in detail in references 8, 9, 12, and 13. The goal of these tests was to define the hypersonic aerodynamic and aeroheating environment of the X-33 vehicle. The aeroheating tests were performed in the Langley 20-Inch Mach 6 Air Tunnel using the global thermographic phosphor technique and encompassed over 1100 runs

in which the effects of angle of attack, body-flap deflection, Reynolds number, and discrete and distributed surface roughness on the X-33 heating characteristics were determined. The aerodynamic test series consists of several hundred runs in the Langley 31-Inch Mach 10 and 20-Inch Mach 6 Air Tunnels in which the effects of Reynolds number, angle of attack, and control surface deflections on the aerodynamic forces and moments were investigated.

Test Facility Descriptions

The Langley 20-Inch Mach 6 Air Tunnel (fig. 11) and Langley 31-Inch Mach 10 Air Tunnel (fig. 12) are both conventional blowdown tunnels in which heated, dried, and filtered air is used as the test gas. Freestream Reynolds numbers of 0.5×10^6/ft to 2×10^6/ft at a stagnation temperature of 1800 °R can be produced in the 31-Inch Mach 10 Air Tunnel, while freestream Reynolds numbers of 0.5×10^6/ft to 7×10^6/ft with stagnation temperatures of 760 °R to 1000 °R can be produced in the 20-Inch Mach 6 Air Tunnel. Both facilities have fast injection systems (bottom-mounted in the Mach 6 tunnel, side-mounted in the Mach 10 tunnel) that can place test models on the tunnel centerline in under 1 s. Detailed information on both facilities can be found in reference 35.

Thermographic Phosphor Global Heating Technique

Global surface heating distributions were obtained through the digital optical measurement method of two-color, relative-intensity, phosphor thermography (refs. 36–39). In this method (fig. 13), ceramic wind-tunnel models are coated with a phosphor compound that fluoresces in two separate regions (green and red) of the visible light spectrum. During a wind-tunnel run, the phosphor-coated model is illuminated by ultraviolet (UV) light sources, and the resulting fluorescent intensity of the model is recorded and digitized through a color charge coupled device (CCD) camera. The fluorescent intensity is dependent on both the intensity of incident UV light and the local model surface temperature. The UV intensity dependence is removed by taking the ratio of the green to red intensity images, from which surface temperature distributions can be determined through prior calibrations. Images are acquired before the wind-tunnel run and after injection of the model to the tunnel centerline

during a run. Global heat transfer distributions are then computed from these temperature data using one-dimensional, constant heat transfer coefficient conduction theory.

The global phosphor thermography technique is now the standard method for aeroheating studies in Langley's hypersonic tunnels. The global data obtained using this method permit the resolution of complex three-dimensional flow phenomena such as transition fronts, vortex structures, and shock interactions that are difficult to examine using conventional discrete-sensor methods such as thin-film resistance gauges or coaxial surface thermocouples. Recent studies such as references 39 and 40 have demonstrated the accuracy of phosphor thermography through comparisons with both thin-film gauge heating data and computational fluid dynamics (CFD) predictions.

Thermographic phosphor data are commonly reported in terms of the heat transfer coefficient ratio, h/h_{FR}, where h is the heat transfer coefficient measured in the wind tunnel and h_{FR} is a reference heat transfer coefficient based on Fay-Riddell theory (ref. 41). The heat transfer coefficient is defined as

$$h = \dot{q}/(H_{AW} - H_w) \qquad (13)$$

In the heat transfer coefficient, the adiabatic wall enthalpy H_{AW} is set equal to the total enthalpy H_0 in the tunnel. The enthalpy coefficient definition produces a theoretically constant value over the course of a wind-tunnel run because the drop in $\dot{q}$ over time as the wind-tunnel model surface temperature increases is offset by the decrease of the enthalpy term $(H_{AW} - H_w)$ in the denominator. The Fay-Riddell value, h_{FR}, is computed using the reference nose radius of the X-33 vehicle at the appropriate model scale (1.21 m full scale) at a wall temperature of 300 K. Heat transfer results from the computations will also be presented in terms of the ratio h/h_{FR}.

As discussed in reference 39, the experimental uncertainty of the phosphor technique is dependent on the temperature rise on the surface of the test model. For the experimental results discussed herein, windward surface heating data were estimated to have an uncertainty of ±8 percent due to the measurement technique and an overall uncertainty of ±15 percent due to all factors, such as free-stream conditions and

flow uniformity, model placement, accuracy of model aerolines, quality of thermographic phosphor coating, image acquisition system calibration, etc. For leeward heating data, where the surface temperatures are considerably lower, the measurement uncertainty is estimated at ±15 percent with an overall uncertainty of ±25 percent.

Aerodynamic Force and Moment Technique

Aerodynamic forces (normal, axial, side) and moments (pitch, roll, yaw) were measured using six-component, water-cooled strain gauge balances. Data were obtained in pitch/pause mode, with pauses of 3 to 5 s at a given point. Data were averaged over 1-s intervals with an acquisition rate of 20 samples per second. Sting cavity and model base pressure measurements were made to ensure that pressure levels in these areas remained sufficiently low that no corrections to the data were required.

The experimental uncertainty of the aerodynamic data is estimated at ±0.5 percent of the full-scale load capacity of the balance. The balance precision obtained through calibration is generally much smaller than this number, but with other possible sources for additional uncertainties—such as balance heating effects on the balance, flow conditions, and model positioning—±0.5 percent of the full-scale load estimate should provide a reasonable estimate for the total data uncertainty. Over the course of the aerodynamic tests, five different balances were used to obtain data. Details of these balances and quoted uncertainties can be found in reference 13.

Wind-Tunnel Model Descriptions

Cast ceramic models (fig. 14) are used for aeroheating testing with the thermographic phosphor system. To fabricate these models, a rapid prototyping stereolithographic apparatus is first used to build a resin model of the configuration. A wax mold of the resin model is then formed, and then a patented silica-ceramic investment slip-casting technique (ref. 42) is used to make a ceramic shell model of the vehicle. For strength and support, the ceramic shell model is back-filled with a hydraulically setting magnesia ceramic into which a sting is fixed. Finally, the model is coated with a mixture of phosphors suspended in a silica-based colloidal binder. This phosphor coating consists

of a 5:1 mixture of lanthanum oxysulfide (La_2O_2S) doped with trivalent europium and zinc cadmium sulfide (ZnCdS) doped with silver and nickel.

The model scale for the aeroheating tests was 0.0132, which produced a 0.254-m (10.0-in.) model length measured from the model nose to the end of the engine module. Models of the F-Loft, Rev-F configuration were fabricated with body-flap deflections of 0°, 10°, and 20°. Several copies of each flap deflection were made in order to provide backup models and model-to-model checks on the fabrication process. Also, as discussed in reference 8, the effects of raised or bowed thermal protection system (TPS) tiles on the state of the boundary layer were investigated through the use of discrete and distributed roughness elements. Discrete roughness elements were produced by application of one or more layers of 0.0025-in. thick Kapton tape squares at various locations (e.g., a single centerline trip or an array of trips across the body) on the windward surface of a model. A distributed roughness pattern that simulates the bowing of the windward surface TPS tiles due to temperature gradients within the metallic tiles was created through fabrication of models (fig. 15) with tiles raised to heights of 0.002 to 0.008 in. between $X/L = 0.10$ and 0.45. More in-depth information on the models may be found in references 8, 9, and 12.

Aerodynamic data were obtained with a 0.007-scale metallic force-and-moment model of the F-Loft, Rev-G configuration designed and fabricated at LaRC. The model was built with removable canted fins, body flaps, vertical tails, and engine blocks. Fins, rudders, and body flaps with various deflections were fabricated and fin, flap, and engine off-blocks were also made for use in configuration buildup studies. The model was designed to accept a base-mounted sting (fig. 16) or a leeside-mounted blade strut support (fig. 17).

Computational Results and Comparisons With Wind-Tunnel Aeroheating and Aerodynamic Data

Surface Heating, Pressure, and Streamlines for Wind-Tunnel Cases

Symmetry-plane Mach number distributions, surface pressure and heating distributions, and surface streamlines at Mach 6 are shown for angles of attack of 20°, 30°, and 40° in figures 18–21, 22–25, and 26–29, respectively. The results presented are from laminar GASP computations for the 20-Inch Mach 6 Air Tunnel conditions. Schlieren images from the wind-tunnel tests are shown along with Mach number distributions for comparison. Note that in the surface heating and pressure distribution figures, separate scales are shown for the pressure or heating levels on the windward and leeward sides of the vehicle, and that the streamlines are color coded to show surface pressures.

Post-shock Mach numbers in the windward symmetry plane varied from the 3 to 4 range at $\alpha = 20°$ to 1 to 2 at $\alpha = 40°$, while leeward symmetry-plane Mach numbers are in the range of 2 to 4 for all angles of attack. Aside from the nose, chine, and wing leading edge regions, windward surface pressure distributions were nearly constant. Leeside surface pressures were at least an order of magnitude lower than on the windward side. Relatively high heating occurred at the nose of the vehicle, along the chines, and on the leading edges of the canted fins. Evidence of a bow-shock/fin-shock interaction can be seen in the heating distribution on the leesides of the canted fins. Windward surface streamline patterns showed a strong inflow from the chines toward the centerline at $\alpha = 20°$. The inflow was less pronounced at $\alpha = 30°$, and at $\alpha = 40°$ the flow was parallel to the centerline. It can be seen in the surface streamlines that the flow split along the chines, with part of the flow going around to the leeside of the body and part remaining on the windward side. Leeside streamline patterns showed a symmetric pair of separated flow vortices emanating from near the nose of the vehicle at all angles of attack, and secondary vortices could also be seen further down the length of the vehicle at $\alpha = 20°$ and 30°.

Comparisons With Wind-Tunnel Aeroheating Data

Comparisons between GASP heating predictions and wind-tunnel measurements in the Langley 20-Inch Mach 6 Air Tunnel are presented in this section. Comparisons of laminar and turbulent predictions are made to data from smooth body models, models with bowed panels, and models with discrete trips placed on the fuselage for angles of attack of 20°, 30°, and 40° with body-flap deflections of $\delta_{BF} = 0°$, 10°, and 20°. Global

aeroheating comparisons are made to the thermographic phosphor images. Detailed comparisons are made with data extracted from the images along the windward centerline, along the chines, and across the fuselage at axial stations of X/L = 0.05, 0.10, 0.20, 0.30, 0.40, 0.50, 0.60, 0.70, 0.80, and 0.90, where L is the distance from the nose to the end of the engine module. The "cut" locations for these detailed comparisons are shown in figure 30.

It should be noted that a subset of the aeroheating comparisons to be presented in subsequent sections has previously been presented in references 9, 10, and 12. However, it was later discovered that due to a calibration error in the thermographic phosphor system, much of the experimental data presented in those references were incorrect, and as a result conclusions drawn from those data were also incorrect. Further details are presented in reference 43. In this report, all comparisons are based on data that have been re-reduced using the correct calibration information.

Laminar Aeroheating Comparisons for Smooth Models

Laminar comparisons for angles of attack of 20°, 30°, and 40° on smooth models with undeflected body flaps (except for the $\alpha = 20°$ experimental cases where only $\delta_{BF} = 10°$ data were available) are presented in figures 31–33, 34–36, and 37–39, respectively. Each group of figures includes both graphical comparisons of the windward heating distributions and line-plot comparisons of the heating distributions at the various data-cut locations. All computations were performed for a free-stream Reynolds number of 4×10^6/ft, while experimental data are shown for $Re_\infty = 1 \times 10^6$/ft, 2×10^6/ft, and 4×10^6/ft.

For the range of test Reynolds numbers in these comparisons, the experimental heating data appeared to have no dependency on Reynolds number when expressed in the normalized form of h/h_{FR} (with the exception of the 10° body-flap data for $\alpha = 20°$). Therefore, it was concluded that the boundary layer remained laminar and comparisons with the laminar computations were valid. The only exception was near the centerline at the end of the fuselage at $Re_\infty = 4 \times 10^6$/ft where transition appeared to begin for all angles of attack.

The laminar computations agreed closely with the experimental data. In general, the two data sets differed by less than ±10 percent, and only along the chines did the differences approach the experimental uncertainty of ±15 percent. The greater differences along the chines may have been due to a need for increased grid resolution for the computations in this high flow-gradient region. The differences may also have been due to conduction losses in the wind-tunnel models because of the high surface-temperature gradient around the chines, or to optical effects in the thermographic phosphor images caused by the high curvature of the chines.

Laminar Aeroheating Comparisons for Bowed Panel Models

Comparisons between the laminar predictions and experimental data on the bowed panel models for angles of attack of 30° and 40° with undeflected body flaps are shown in figures 40–42 and 43–45, respectively. Experimental data are shown for $Re_\infty = 1 \times 10^6$/ft and 2×10^6/ft, while the computations were performed at $Re_\infty = 4 \times 10^6$/ft. As with the smooth model comparisons above, both graphical and line-plot comparisons are shown for each angle of attack.

For the Reynolds number range shown, h/h_{FR} exhibited no Reynolds number dependency and therefore the data were assumed to be laminar. Although the panels spanned almost the first one-half of the fuselage length, the experimental and computational heating distributions again agreed to within the experimental uncertainty of the data except in the immediate region of the panels, where perturbations above the computed heating levels were observed. However, these perturbations did not continue downstream, which suggested that the boundary layer remained laminar at these Reynolds numbers whereas, as will be shown in the next section, the panels did act as a mechanism to trip the boundary layer at higher Reynolds numbers.

Laminar Aeroheating Comparisons for Smooth Models With Deflected Body Flaps

Comparisons between wind-tunnel data and laminar predictions for deflected flaps at $\alpha = 30°$ ($\delta_{BF} = 20°$) and $\alpha = 40°$ ($\delta_{BF} = 10°$ and 20°) on

smooth models are shown in figures 46–51. Experimental data are presented for free-stream Reynolds numbers of 0.5×10^6/ft (except at $\alpha = 30°$), 1×10^6/ft, and 2×10^6/ft, while the computations were performed at $Re_\infty = 4 \times 10^6$/ft. Global image comparisons are shown for each case; however, as both computations and measurements showed that body-flap deflection affected only a small region upstream of the body flaps, line-plot comparisons are shown only for the data-cut running along the chine and onto the body flap.

For the $\alpha = 30°$, $\delta_{BF} = 20°$ case, the experimental data were not constant with Reynolds number and were considerably higher than the predictions, which suggested that the boundary layer is transitional or turbulent on the body flaps.

For the $\alpha = 40°$, $\delta_{BF} = 10°$ case, the experimental data were Reynolds number independent, which indicated laminar flow. Close agreement between the measurements and predictions, except at the body-flap hinge line ($X/L \approx 0.87$), also suggested the body-flap boundary layer remains laminar. Higher grid-point resolution would probably have been required for closer agreement at the hinge line.

For the $\alpha = 40°$, $\delta_{BF} = 20°$ body-flap deflection case, the experimental heating data began to increase with Reynolds number above $Re_\infty = 1 \times 10^6$/ft, which indicated that the deflection had caused the flow to become transitional or turbulent. Further evidence of transition was provided by the fact that measured heating distributions for the $Re_\infty < 2 \times 10^6$/ft cases compared with the laminar predictions to within slightly more than experimental uncertainty, while the $Re_\infty = 2 \times 10^6$/ft data were up to 50 percent higher than the laminar predictions.

A noticeable feature of the deflected body-flap experimental data was the diagonal band of elevated heating near the end of the body flap. This heating increase was due to the interaction that occurred between the bow shock of the vehicle and the shock from a deflected body flap. As shown in figure 52, the interaction produced an expansion wave that washed over the end of the flap. The expansion fan thinned the boundary layer on this portion of the body flap and caused an increase in the heating, as shown in figure 53. The heating patterns shown in this figure are

from a laminar computation and agreed qualitatively with the experimental data, but as shown in the previous comparisons, the effects on the heating were more severe in the transitional/turbulent wind-tunnel data. This interaction also affected the vehicle's aerodynamic performance, as will be discussed subsequently.

Turbulent Aeroheating Comparisons

All turbulent computations were performed using GASP with the Baldwin-Lomax turbulence model modified for compressible flow. In these computations, the flow was modeled as completely turbulent over the whole length of the vehicle. However, for the range of experimental free-stream test conditions ($Re_\infty = 1 \times 10^6$/ft to 4×10^6/ft), the model length was insufficient to produce natural, fully developed turbulent flow except in some cases on deflected body flaps. Additionally, the aft-end of the fuselage between the body flaps has an upsweep that forms an expansion ramp, producing a favorable (decreasing) pressure gradient that limits the growth of turbulence. Therefore, the boundary layer was artificially tripped using both discrete- and distributed-roughness elements in an attempt to produce fully developed turbulent flow.

For the discrete-roughness cases, the trips produced wedge-shaped regions of what appeared to be fully developed turbulent flow behind the trips, while for the distributed-roughness cases, fully developed turbulent flow appeared to be produced at or behind the bowed panels across the width of the fuselage. In most cases, the transition location was not symmetric across the body due to small differences in trip height, placement, and/or orientation, or because the trip arrangement was (intentionally) asymmetric.

In all cases where roughness elements were employed, heating rates downstream from the trips showed a rapid increase attributed to transition, after which they remained nearly constant over the rest of the length of the vehicle, behavior which is attributed to fully developed turbulent flow. Because the measured turbulent heating levels did not show a significant dependence with running length (after the transition region), comparisons between computations that were treated as fully turbulent over the whole vehicle and measurements in which turbulence

developed downstream from the nose on the fuselage should still be valid.

Turbulent Aeroheating Comparisons for Smooth Models With Trips

Comparisons between turbulent aeroheating predictions and experimental data on smooth models with trips are presented for angles of attack of 20°, 30°, and 40° with undeflected body flaps in figures 54 and 55, 56 and 57, and 58 and 59, respectively. Additionally, comparisons at $\alpha = 40°$ for the 20º deflected body-flap cases are presented in figures 60 and 61. Because turbulent flow was produced over only a portion of the fuselage, comparisons with prediction are only shown for the centerline, chines, and aft portion of the vehicle.

The downstream influence of the discrete-roughness elements generally was observed to be limited. As can be seen in figures 54, 56, or 58, the heating rise caused by a discrete element was confined to a narrow wedge behind the element that spread very little over the length of the fuselage. The region of influence of these trips should be noted when examining the plotted comparison between the tripped data and the computations.

For the $\alpha = 20°$ and 40° cases, the turbulent experimental data and turbulent predictions matched to within the experimental uncertainty of ±15 percent. For the $\alpha = 30°$ case, the experimental data were up to approximately 25 percent higher than the predictions. The heating predictions for the deflected flap case were within the uncertainty of the experimental data except, as was also observed for the laminar comparison, at the flap hinge line.

Turbulent Aeroheating Comparisons for Models With Bowed Panels

Comparisons between turbulent aeroheating predictions and experimental data on bowed panel models for angles of attack of 30° and 40° with undeflected body flaps are presented in figures 62 and 63 and 64 and 65, respectively. In contrast to the discrete trips on the smooth models, the distributed-roughness elements produced a wider, more uniform region of non-laminar flow that spanned most or all of the fuselage, as can be seen in figure 62 or 64. For the $\alpha = 30°$ case, the predictions were within approximately ±25 percent

of the data whereas for the $\alpha = 40°$, the predictions compared to the measurements to within the experimental uncertainty of ±15 percent except on portions of the chines.

Wall Temperature Distributions for Flight Cases

GASP and LAURA results for cases on the Michael 9A-8 trajectory are presented in this section. GASP computations were performed for all four cases, while LAURA computations were performed for cases 1 and 3. Computed radiative-equilibrium wall temperature distributions for each of the four flight cases are shown in figures 66–69. Centerline windward and leeward surface temperature distributions for all cases are plotted in figures 70–73, and temperature distributions at constant X locations of 5.0, 10.0, and 15.0 m are shown for cases 1 and 3 in figures 74–79. Most of the windward surface was found to remain in the 400 to 800 K (260 to 980 °F) temperature range for all cases, except for the chines, nose, and wing leading edges. Chine and wing leading temperatures varied between 700 and 900 K (800 and 1160 °F), while nose temperatures approached 1200 K (1700 °F).

As discussed earlier, the GASP computations were run with equilibrium chemistry (as opposed to nonequilibrium chemistry with LAURA) on a coarser $64 \times 91 \times 65$-point grid (compared with the $254 \times 181 \times 65$-point LAURA grid) in order to save time and computational resources. Nevertheless, the GASP results were in close agreement with the LAURA results, as shown by the comparisons for cases 1 and 3. Temperatures in the nose region compared well between the two methods, which confirmed the assumption that nonequilibrium chemistry was not a factor at these relatively low flight Mach numbers. Slightly larger differences around the chines and in the shock-interaction regions on the fins were probably due to the coarseness of the GASP grid.

Comparisons With Wind-Tunnel Aerodynamic Data

Aerodynamic predictions from GASP and LAURA for the Mach 6 and Mach 10 wind-tunnel conditions are presented in this section. Normal force (C_N), axial force (C_A), and pitching moment (C_m) coefficients are plotted versus angle of attack for each

case. Axial force and pitching moment coefficients are shown for 0°, 10°, and 20° body-flap deflections; body-flap deflection had little effect on the normal force, so only the 0° information is shown. The experimental data consist of several hundred measurements of each coefficient of which only curve fits are shown for clarity. Each curve fit is bordered by a shaded band that shows the uncertainty of the measurements based on the ±0.5 percent of the balance full-scale load estimate.

GASP and LAURA predictions for the 20-Inch Mach 6 Air Tunnel conditions are compared with the experimental data in figures 80–82. For the 20° body-flap deflection, an inflection in the pitching moment curve at around $\alpha = 35°$ was present. This inflection resulted from the bow-shock/flap-shock interaction discussed earlier. The interaction produced an expansion fan that impinged on the body flap and caused a drop in the surface pressure, thereby reducing the pitching moment produced by the flap. Normal force predictions were within the experimental uncertainty, while the axial and pitching moment predictions were slightly outside the experimental uncertainty range. GASP axial force predictions were closer to the data than those from LAURA whereas for pitching moment predictions, LAURA results were closer. For both codes, the differences increased with both angle of attack and body-flap deflection.

One reason considered for the differences between predictions and measurement for the Mach 6 cases was the exclusion of the wake from the computations. Therefore, a solution for the $\alpha = 36°$, $\delta_{BF} = 20$ case was computed with GASP using the 16-block, full-wake grid. Aerodynamic coefficients for this case have also been included on the Mach 6 plots. The differences between the GASP full-wake grid solution and the LAURA single-block, no-wake grid solution at the same point were very small, and it was concluded that exclusion of the wake from the computations had little effect on the aerodynamic predictions. Another possible source of error in the computations was the grid-point density. However, as will be shown in the next section, the aerodynamic coefficients were relatively insensitive to grid resolution. Thus, the source of the differences between experiment and computation at Mach 6 remains unresolved. However, the X-33 vehicle was designed to trim with little or no body-flap deflection in hypersonic, high angle-of-attack flight but has a 30° flap deflection capability, so

these differences were well within the control deflection authority of the vehicle.

GASP and LAURA predictions for the 31-Inch Mach 10 Air Tunnel conditions are provided for comparison with the experimental data in figures 83–85. Note that the inflection in the pitching moment curve was again present. For all variables, the predictions from both codes were within the experimental uncertainty.

Mach Number Versus Angle-of-Attack Parametric Aerodynamics

In order to investigate the effects of Mach number and angle of attack on the aerodynamics of the X-33 vehicle, a series of perfect-gas computations were performed using GASP across a range of Mach numbers from 4 to 10 and angles of attack of 10° to 50°. A constant Reynolds number of 6.59×10^6/m (2.01×10^6/ft) was maintained for all computations. The free-stream temperatures were determined by interpolation with Mach number between the free-stream temperatures of the 31-Inch Mach 10 Air and 20-Inch Mach 10 Air Tunnels.

Results from these computations are presented in figures 86–91. The predictions for the force coefficients (C_A, C_N, C_L, and C_D) and the lift-to-drag ratio (L/D) all showed similar behavior; that is, the magnitude of the coefficient versus angle-of-attack curves for each variable decreased with increasing Mach number. A trend toward Mach number independence was indicated by the fact that differences between the curves decreased with increasing Mach number. However, the pitching moment coefficient behavior differed from that of the other coefficients in that a stronger Mach number dependency was observed (fig. 88). For angles of attack above 20°, a consistent trend could be observed where the pitching moment curve was stable (negative slope) and the magnitude of C_m increased with increasing Mach number. The trim point ($C_m = 0$) appeared to be nearly Mach-independent at around 43°. Also, the pitching moment curves all appeared to be tending toward instability somewhere below $\alpha < 20°$, depending on Mach number.

These M-α parametric space computations were performed on a coarser grid ($65 \times 91 \times 33$) than the

other GASP computations with the intent of identifying trends rather than producing quantitative results. However, as the data show in table 5 (aerodynamic coefficients on the coarse grid and GASP computations on the finer grid ($127 \times 181 \times 65$) for the 31-Inch Mach 10 Air Tunnel cases), the accuracy of the coarser grid results was almost as good as those on the finer grid, at least for aerodynamics. The parametric computations were within less than ± 1 percent of the finer grid computations except for the pitching moment at $\alpha = 30°$ and $40°$, where the value of this coefficient approached zero.

Summary

Aerodynamic and aeroheating predictions were generated for the X-33 vehicle at both flight and wind-tunnel test conditions using two finite-volume, Navier-Stokes solvers. Wind-tunnel aerodynamic computations were performed at Mach 6 and Mach 10 for angles of attack of $10°$ to $50°$ with body-flap deflections of $0°$ to $20°$. Additional aerodynamic computations were performed over a parametric range of free-stream conditions with Mach numbers of 4 to 10 and angles of attack of $10°$ to $50°$. Laminar and turbulent wind-tunnel aeroheating computations were performed at Mach 6 for angles of attack of $20°$ to $40°$ with body-flap deflections of $0°$ to $20°$. Aeroheating computations were performed at four points along the flight trajectory with Mach numbers of 6.6 to 8.9 and angles of attack of $10°$ to $40°$ using both equilibrium and nonequilibrium thermochemical models. Surface heating and pressure distributions, surface streamlines, flow field information, and aerodynamic coefficients from these computations are presented, and comparisons are made with wind-tunnel data.

Laminar aeroheating predictions for the wind-tunnel cases matched the low Reynolds number ($Re_\infty \leq 4 \times 10^6$/ft) experimental data to within the estimated uncertainty of ± 15 percent at all points on the body except on portions of the chines and on the deflected body flaps where the flow appeared to be transitional/turbulent for some test conditions. Computations showed that the expansion fan produced by the bow-shock/flap-shock interaction augmented the body-flap heating in the area where the fan impinges on the flap.

The incompressible, Baldwin-Lomax algebraic turbulence model was modified for compressible, hypersonic flows and used to generate turbulent aeroheating predictions. For the wind-tunnel test conditions, natural, fully developed turbulent boundary-layer flow was not produced; therefore, the boundary layer was tripped using both discrete- and distributed-roughness elements. Comparisons between predictions and measurements on models with both distributed- and discrete-roughness elements were within ± 25 percent at $\alpha = 30°$ and within ± 15 percent at $\alpha = 20°$ and $40°$.

Flight aeroheating computations performed with two different codes were found to be in close agreement. For the selected trajectory points, peak temperatures of around 800 to 1200 K were predicted at and around the nose. Chine and wing leading edge temperatures were in the range of 700 to 900 K whereas the fuselage reached temperatures in the 400 to 800 K range.

Predicted aerodynamic coefficients were found to match Mach 10 wind-tunnel data to within the experimental uncertainty while the Mach 6 predictions for axial force and high angle-of-attack pitching moment fell slightly outside the uncertainty range. Flow field predictions revealed the existence of an interaction between the bow shock of the vehicle and the shocks produced by deflected body flaps. This interaction produces expansion fans that wash over the body flaps and decrease their contribution to the vehicle's pitching moment at high angles of attack. M-α parametric predictions showed that the aerodynamic coefficient tends toward Mach number independence at high Mach (≈ 10) numbers, and that the vehicle is stable for $\alpha > 20$ and trims near $43°$.

References

1. Bekey, I.; Powell, R.; and Austin, R.: NASA Studies Access to Space. *Aerospace America*, May 1994, pp. 38–43.

2. Cook, S. A.: X-33 Reusable Launch Vehicle Structural Technologies. AIAA-96-4563, Nov. 1996.

3. Freeman, D. C., Jr.; Talay, T. A.; and Austin, R. E.; Reusable Launch Vehicle Technology Program. AIAA IAF 96-V.4.01, Oct. 1996.

4. Powell, R. W.; Lockwood, M. K.; and Cook, S. A.: The Road From the NASA Access-to-Space Study to a Reusable Launch Vehicle. AIAA IAF-98-V.4.02, Sept. 1998.

5. Baumgartner, R. I.; and Elvin, J. D.: Lifting Body—An Innovative RLV Concept. AIAA-95-3531, Sept. 1995.

6. Thompson, R. A.; Hamilton, H. H., II; Berry, S. A.; and Horvath, T. J.: Hypersonic Boundary Layer Transition for X-33 Phase II Vehicle. AIAA-98-0867, Jan. 1998.

7. Hamilton, H. H., II; Weilmuenster, K. J.; Berry, S. A.; and Horvath, T. J.: Computational/Experimental Aeroheating Predictions for X-33 Phase II Vehicle. AIAA-98-0869, Jan. 1998.

8. Berry, S. A.; Horvath, T. J.; Hollis, B. R.; Thompson, R. A.; and Hamilton, H. H., II: X-33 Hypersonic Boundary Layer Transition. *J. of Spacecr. and Rocket*s, vol. 38, no. 5, Sept.–Oct. 2001, pp. 646–657.

9. Berry, S. A.; Horvath, T. J.; Kowalkowski, M. K.; and Liechty, D. S.: *X-33 (Rev-F) Aeroheating Results of Test 6770 in NASA Langley 20-Inch Mach 6 Air Tunnel*. NASA/TM-1999-209122, 1999.

10. Hollis, B. R.; Horvath, T. J.; Berry, S. A.: Hamilton, H. H., II; Thompson, R. A.; and Alter, S. J.: X-33 Aeroheating Predictions and Comparisons With Experimental Data. *J. of Spacecr. and Rockets*, vol. 38, no. 5, Sept.–Oct. 2001, pp. 658–669.

11. Hollis, B. R.; Thompson, R. A.; Murphy, K. J.; Nowak, R. J.; Riley, C. J.; Wood, W. A.; Alter, S. A.; and Prabhu, R. K.: X-33 Aerodynamic Computations and Comparisons With Wind Tunnel Data. *J. of Spacecr. and Rockets*, vol. 38, no. 5, Sept.–Oct. 2001, pp. 684–691.

12. Horvath, T. J.; Berry, S. A.; Hollis, B. R.; Liechty, D. S.; Hamilton, H. H., II; and Merski, N. R.: X-33 Experimental Aeroheating at Mach 6 Using Phosphor Thermography. *J. of Spacecr. and Rockets*, vol. 38, no. 5, Sept.–Oct. 2001, pp. 634–645.

13. Murphy, K. J.; Nowak, R. J.; Hollis, B. R.; and Thompson, R. A.: X-33 Hypersonic Aerodynamic Characteristics. *J. of Spacecr. and Rockets*, vol. 38, no. 5, Sept.–Oct. 2001, pp. 670–683.

14. Thompson, R. A.: Review of X-33 Hypersonic Aerodynamic and Aerothermodynamic Development. *22nd International Congress of the Aeronautical Sciences*, ICA-0323, Aug. 27–Sept. 1, 2000.

15. AeroSoft: *GASP Version 3, The General Aerodynamic Simulation Program, Computational Flow Analysis Software for the Scientist and Engineer, User's Manual*. AeroSoft Inc., 1996.

16. Roe, P. L.: Approximate Riemann Solvers, Parameter Vectors and Difference Schemes. *J. of Computational Physics*, vol. 43, no. 2, 1981, pp. 357–372.

17. Van Leer, B.: Flux Vector Splitting for the Euler Equations. *Proceedings of the 8th International Conference on Numerical Methods in Fluid Dynamics*. Springer Verlag, Berlin, 1981.

18. Baldwin, B. S.; and Lomax, H.: Thin Layer Approximation and Algebraic Model for Separated Turbulent Flow. AIAA-78-257, Jan. 1978.

19. Gupta, R. N.; Lee, K. P.; Zoby, E. V.; Moss, J. N.; and Thompson, R. A.: Hypersonic Viscous Shock-Layer Solutions Over Long Slender Bodies—Part 1: High Reynolds Number Flows. *J. of Spacecr. and Rockets*, vol. 27, no. 2, March–April 1990, pp. 175–184.

20. Cheatwood, F. M.; and Thompson, R. A.: *The Addition of Algebraic Turbulence Modeling to Program LAURA*. NASA TM-107758, 1993.

21. Gnoffo, P. A.: *An Upwind-Biased, Point-Implicit Algorithm for Viscous, Compressible Perfect-Gas Flows*. NASA TP-2953, 1990.

22. Cheatwood, F. M.; and Gnoffo, P. A.: *User's Manual for the Langley Aerothermodynamic Upwind Relaxation Algorithm (LAURA)*. NASA TM-4674, 1996.

23. Harten, A.: High Resolution Schemes for Hyperbolic Conservation Laws. *J. of Comput. Phys.*, vol. 49, no. 3, 1983, pp. 357–393.

24. Yee, H. C.: *On Symmetric and Upwind TVD Schemes*. NASA TM-88325, 1990.

25. Alter, S. J.: Grid Generation Techniques Utilizing the Volume Grid Manipulator. AIAA-98-3012, June 1998.

26. Alter, S. J.: *The Volume Grid Manipulator (VGM): A Grid Reusability Tool*. NASA CR-4772, 1997.

27. Gnoffo, P. A.: A Code Calibration Program in Support of the Aeroassist Flight Experiment. AIAA-89-1673, June 1989.

28. Micol, J. R.: Aerothermodynamic Measurement and Prediction for Modified Orbiter at Mach 6 and 10. *J. of Spacecr. and Rockets*, vol. 32, no. 5, Sept.–Oct. 1995, pp. 737–748.

29. Berry, S. A.; Horvath, T. J.; DiFulvio, M.; Glass, C.; and Merski, N. R.: X-34 Experimental Aeroheating at Mach 6 and 10. *J. of Spacecr. and Rockets*, vol. 36, no. 2, March–April 1999, pp. 171–178.

30. Roe, P. L.: Some Contributions to the Modelling of Discontinuous Flows. *Proceedings of the 1983 AMS SIAM Summer Seminar on Large Scale Computing in Fluid*

Mechanics, Lectures in Applied Mathematics, vol. 22. SIAN, 1985, pp.163–193.

31. Chakravarthy, S. R.; and Osher, S.: High Resolution Applications of the Osher Upwind Scheme for the Euler Equations. AIAA-83-1943, 1983.

32. Prabhu, D. K.; Wright, M. J.; Marvin, J. G.; Brown, J. L.; and Venkatapathy, E.: X-33 Aerothermal Design Environment Predictions: Verification and Validation. AIAA-2000-2686, June 2000.

33. Loomis, M. P.; Venkatapathy, E.; Papadopoulos, P.; Davies, C. B.; Horvath, T. J.; Berry, S. A.; and Campbell, C.: Aeroheating and Aerodynamic CFD Validation and Prediction for the X-38 Program. AIAA-97-2478, June 1997.

34. Widhopf, G. F.: Turbulent Heat-Transfer Measurements on a Blunt Cone at Angle of Attack. *AIAA Journal*, vol. 9, no. 9, August 1971, pp. 1574–1580.

35. Micol, J. R.: Hypersonic Aerodynamic/Aerothermodynamic Testing Capabilities at Langley Research Center: Aerothermodynamic Facilities Complex. AIAA-95-2107, June 1995.

36. Buck, G. M.: *Automated Thermal Mapping Techniques Using Chromatic Image Analysis*. NASA TM-101554, 1989.

37. Buck, G. M.: Surface Temperature/Heat Transfer Measurement Using a Quantitative Phosphor Thermography System. AIAA-91-0064, Jan. 1991.

38. Merski, N. R.: *A Relative-Intensity, Two-Color Phosphor Thermography System*. NASA TM-104123, 1991.

39. Merski, N. R.: Global Aeroheating Wind-Tunnel Measurements Using Improved Two-Color Phosphor Thermography Methods. *J. of Spacecr. and Rockets*, vol. 36, no. 2, March–April 1999, pp. 160–170.

40. Horvath, T. J.; Berry, S. A.; Merski, N. R.; and Fitzgerald, S. M.: X-38 Experimental Aerothermodynamics. AIAA-2000-2685, June 2000.

41. Fay, J. A.; and Riddell, F. R.: Theory of Stagnation Point Heat Transfer in Dissociated Air. *J. of Aero. Sci.*, vol. 25, no. 2., Feb. 1958, pp. 73–85.

42. Buck, G. M.; and Vasquez, P.: *An Investment Ceramic Slip-Casting Technique for Net-Form, Precision, Detailed Casting of Ceramic Models*. U.S. Patent 5,266,252, Nov. 1993.

43. Hollis, B. R.; Berry, S. A.; and Horvath, T. J.: X-33 Turbulent Aeroheating Predictions and Measurements. AIAA-2002-4700, Aug. 2002.

Table 1. Reference Dimensions for X-33 F-Loft, Rev-F Configuration

Dimension	Full scale	1.32 percent	0.7 percent
S_{ref}	149.4 m^2	2.60 cm^2	0.732 cm^2
L_{ref}	19.3 m	25.4 cm	13.5 cm
B_{ref}	11.2 m	14.8 cm	7.84 cm
$C.G._{ref}$	12.7 m	16.8 cm	8.89 cm
R_n	1.21 m	1.60 cm	0.847 cm

Table 2. Free-Stream Conditions for Michael 9A-8 Trajectory Cases

Case	M_∞	T_∞, K	ρ_∞, kg/m^3	U_∞, m/s	Re_∞, 1/m	α, deg
1	8.82	265.9	7.07×10^{-4}	2887.3	1.07×10^5	10
2	8.87	258.5	5.13×10^{-4}	2863.5	7.88×10^4	20
3	8.89	252.1	3.87×10^{-4}	2833.5	5.97×10^4	30
4	6.64	263.1	2.09×10^{-3}	2147.4	2.38×10^5	40

Table 3. Free-Stream Conditions for Wind-Tunnel Cases

Tunnel	M_∞	T_∞, K	ρ_∞, kg/m^3	U_∞, m/s	Re_∞, 1/m	α, deg
20-Inch Mach 6 Air ($Re_\infty = 4 \times 10^6$/ft)	5.99	62.1	6.28×10^{-2}	945.1	1.33×10^7	12, 20, 24, 30, 36, 40, 48
31-Inch Mach 10 Air ($Re_\infty = 2 \times 10^6$/ft)	9.98	48.9	1.71×10^{-2}	1414.0	6.84×10^6	12, 20, 24, 30, 36, 40, 48

Table 4. Free-Stream Conditions for Computational Parametric M-α Cases

Mach	T_∞, K	ρ_∞, kg/m^3	U_∞, m/s	Re$_\infty$, 1/m	α, deg
4.0	68.0	4.88×10^{-2}	660.1	6.59×10^6	10, 20, 30, 40
5.0	65.0	3.81×10^{-2}	807.6	6.59×10^6	10, 20, 30, 40, 50
6.0	62.0	3.10×10^{-2}	946.4	6.59×10^6	10, 20, 30, 40, 50
8.0	56.0	2.20×10^{-2}	1198.4	6.59×10^6	10, 20, 30, 40, 50
10.0	50.0	1.66×10^{-2}	1413.8	6.59×10^6	10, 20, 30, 40, 50

Table 5. Differences in Coarse and Fine Grid Aerodynamics for Mach 10 Cases

Coefficient	$127 \times 181 \times 65$ grid	$65 \times 91 \times 33$ grid	Difference, percent
C_A at $\alpha = 20°$	0.1202	0.1206	+0.33
C_N at $\alpha = 20°$	0.3391	0.3388	−0.09
C_m at $\alpha = 20°$	0.0113	0.0114	+0.88
C_A at $\alpha = 30°$	0.1192	0.1195	+0.25
C_N at $\alpha = 30°$	0.6833	0.6813	−0.30
C_m at $\alpha = 30°$	0.0071	0.0073	+2.82
C_A at $\alpha = 40°$	0.1143	0.1144	+0.09
C_N at $\alpha = 40°$	1.0541	1.0544	+0.03
C_m at $\alpha = 40°$	0.0022	0.0019	−13.6
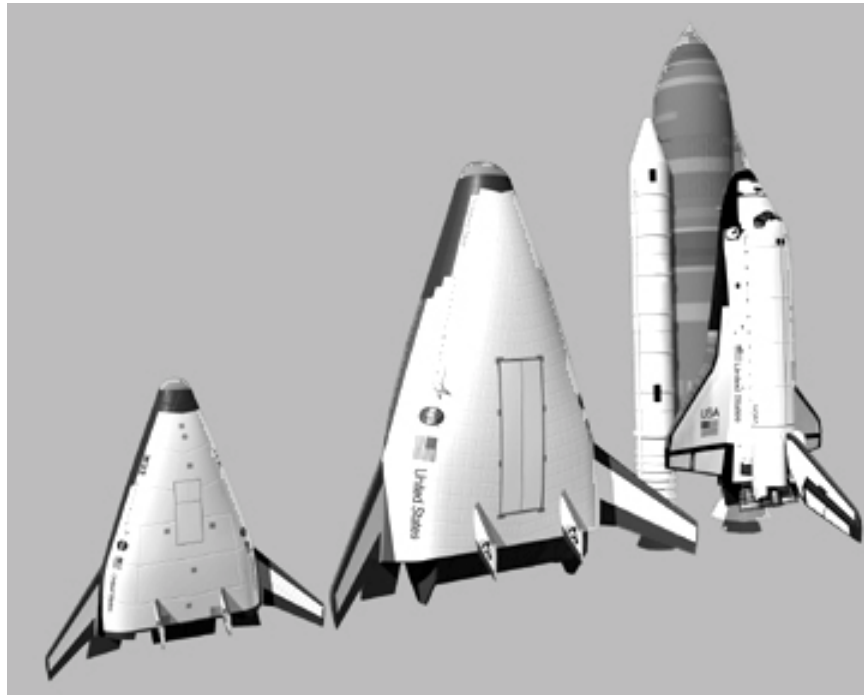
Figure 1. X-33 vehicle, RLV concept, and space shuttle.
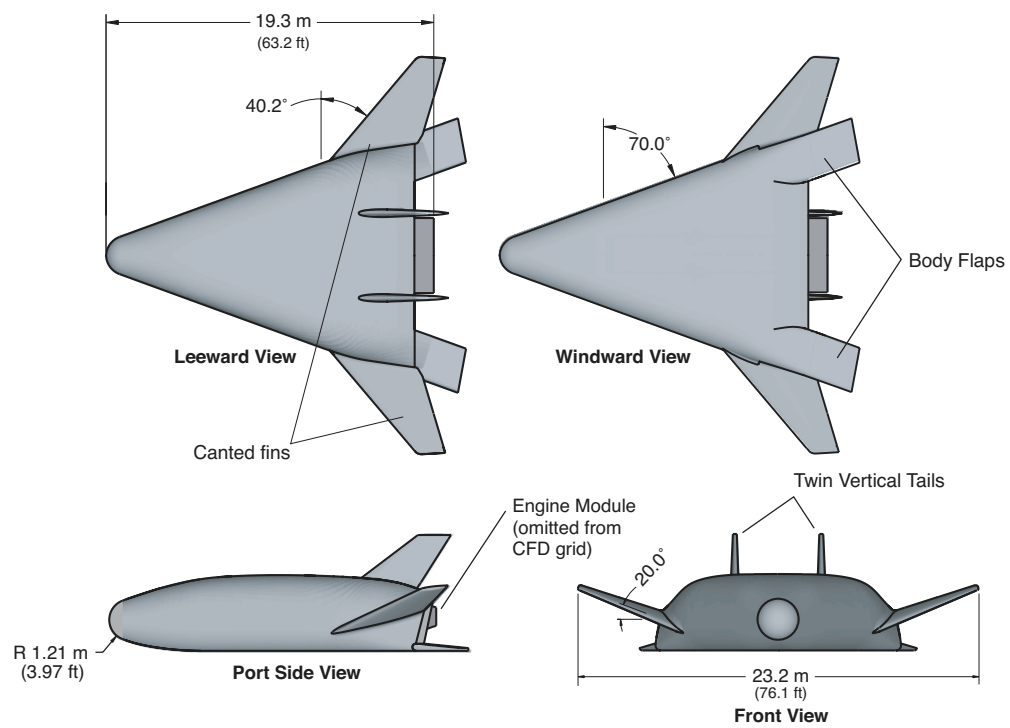
Figure 2. Dimensions of X-33 F-Loft, Rev-F configuration.
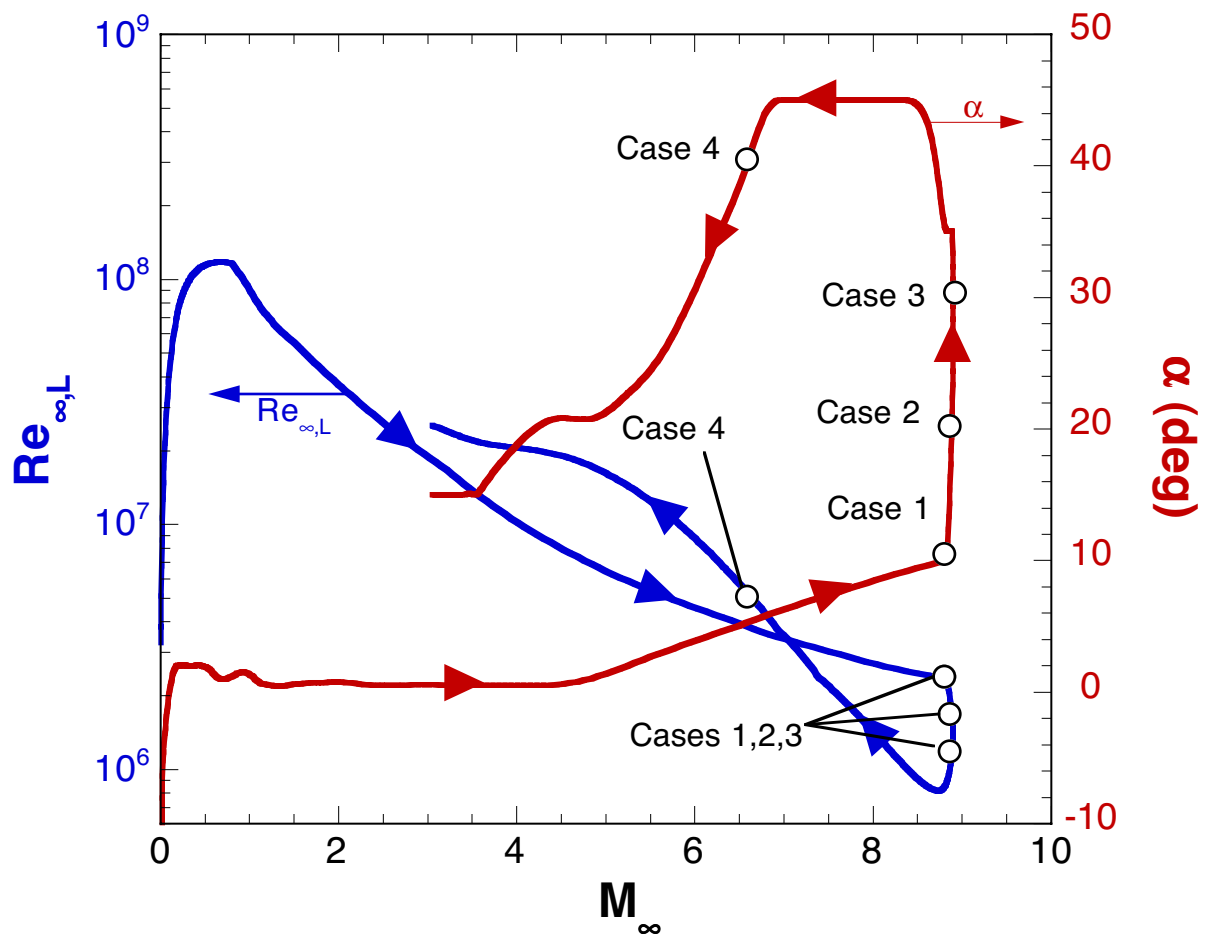
Figure 3. Michael 9A-8 trajectory and points for flight computations.
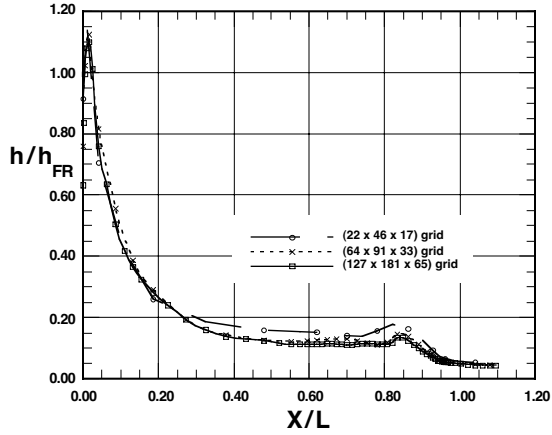
Figure 4. Grid resolution effects on centerline heating, Mach 6 wind-tunnel conditions, $\alpha = 30°$.
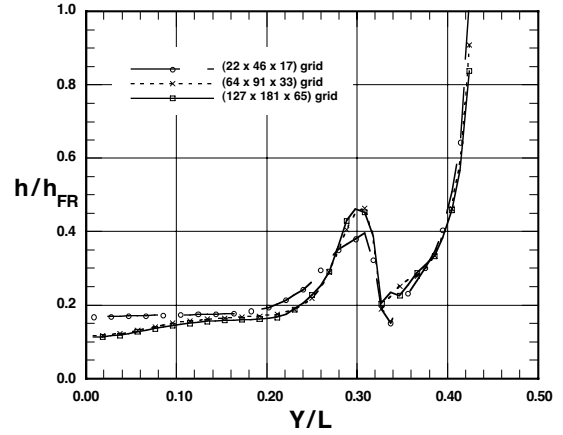
Figure 7. Grid resolution effects on axial ($X/L = 0.8$) heating, Mach 6 wind-tunnel conditions, $\alpha = 30°$.
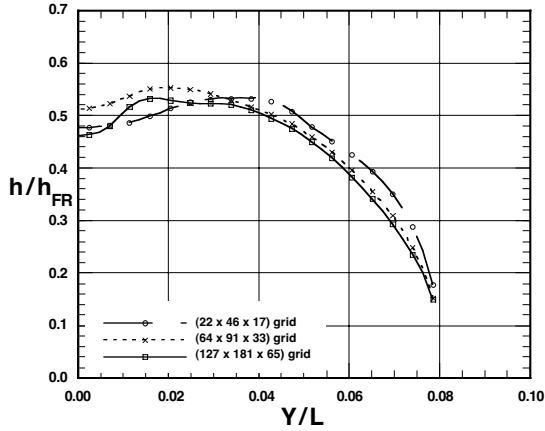
Figure 5. Grid resolution effects on axial ($X/L = 0.1$) heating, Mach 6 wind-tunnel conditions, $\alpha = 30°$.
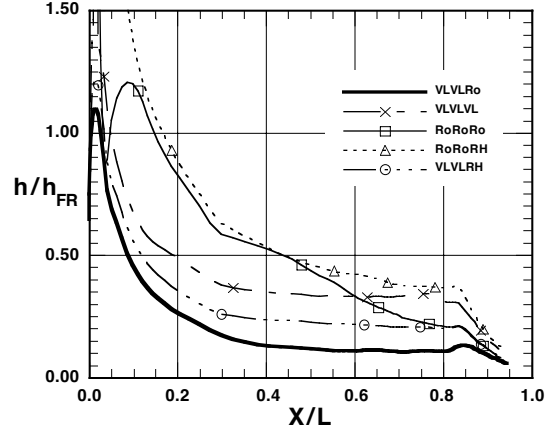
Figure 8. Flux formulation effects on centerline heating, Mach 6 wind-tunnel conditions, $\alpha = 40°$.
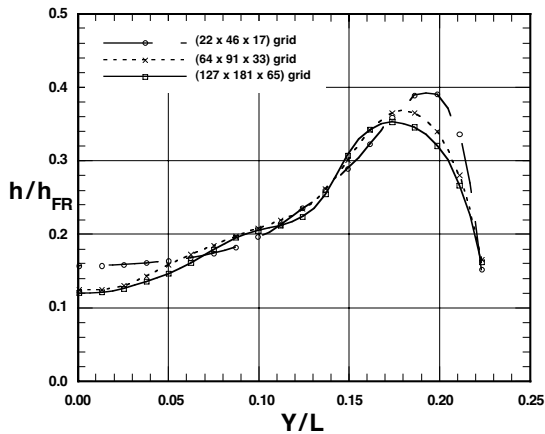
Figure 6. Grid resolution effects on axial ($X/L = 0.5$) heating, Mach 6 wind-tunnel conditions, $\alpha = 30°$.
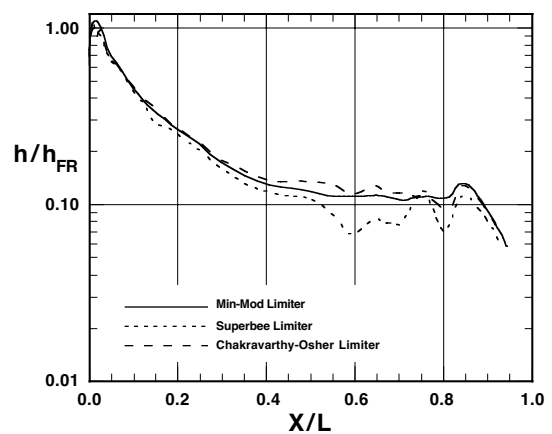
Figure 9. Flux limiter effects on centerline heating, Mach 6 wind-tunnel conditions, $\alpha = 40°$.
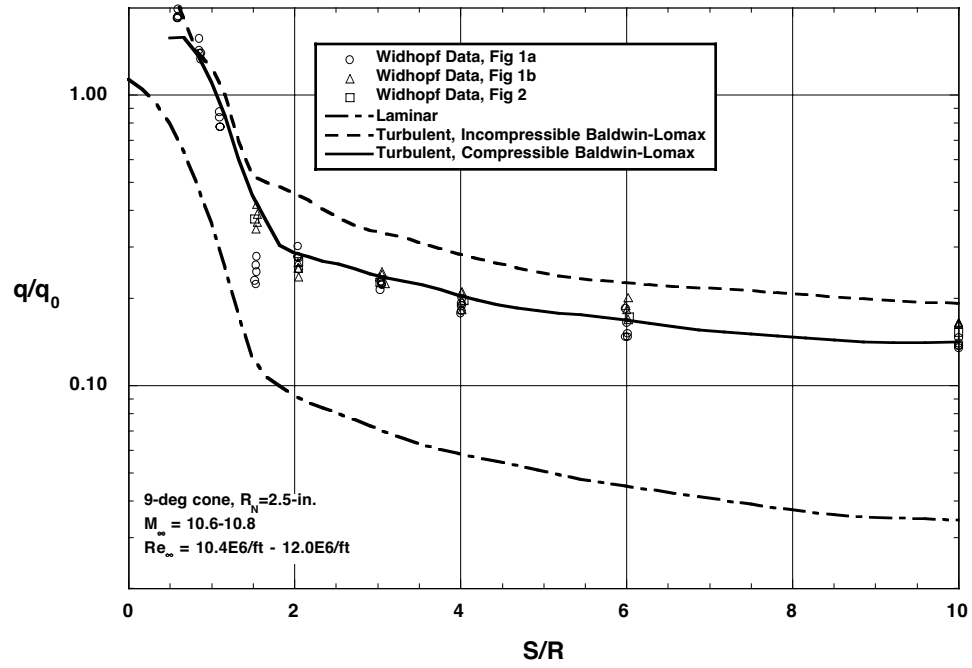
Figure 10. Compressible Baldwin-Lomax aeroheating predictions with data for 9° sphere cone (from ref. 34).

Figure 11. Langley 20-Inch Mach 6 Air Tunnel.
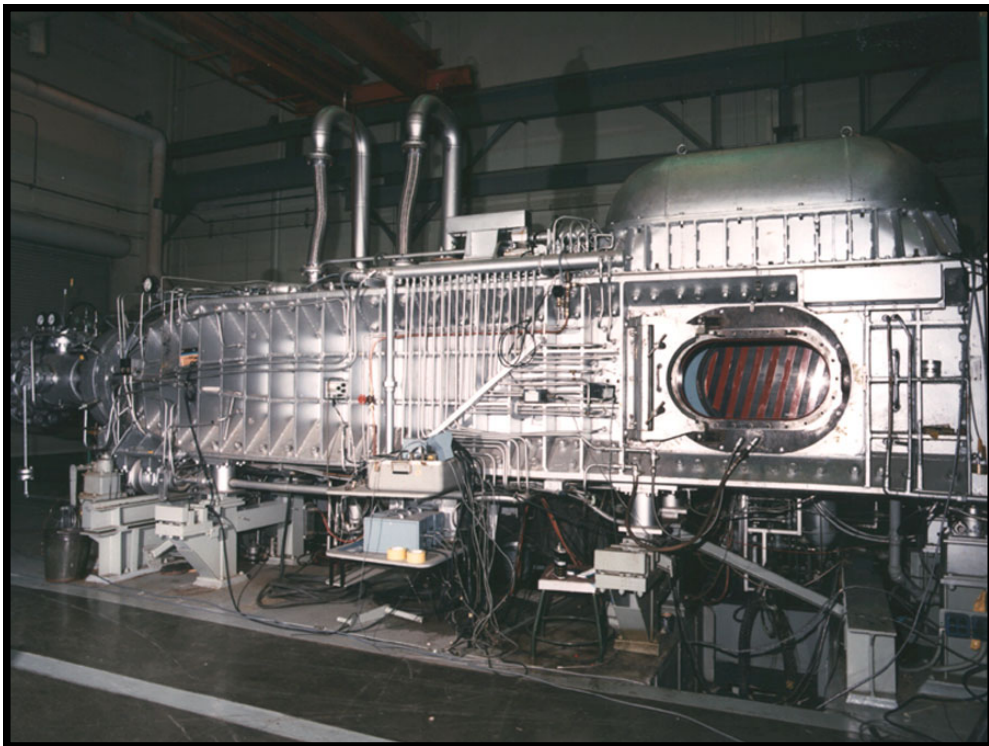
Figure 12. Langley 31-Inch Mach 10 Air Tunnel.
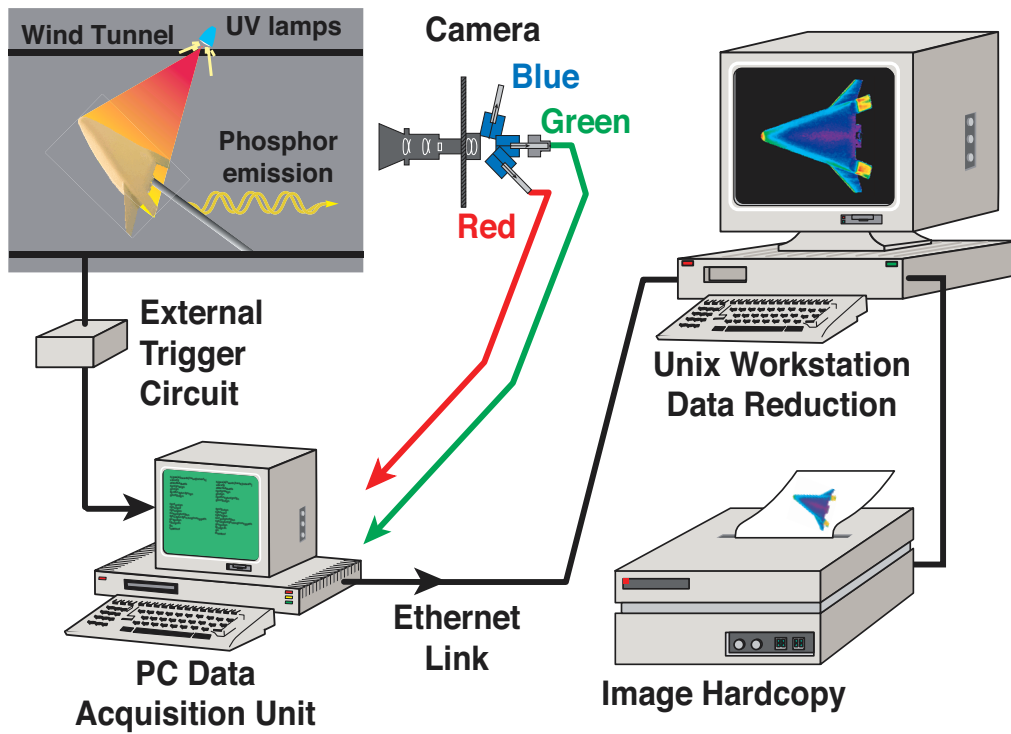
Figure 13. Schematic of Langley two-color thermographic phosphor system.
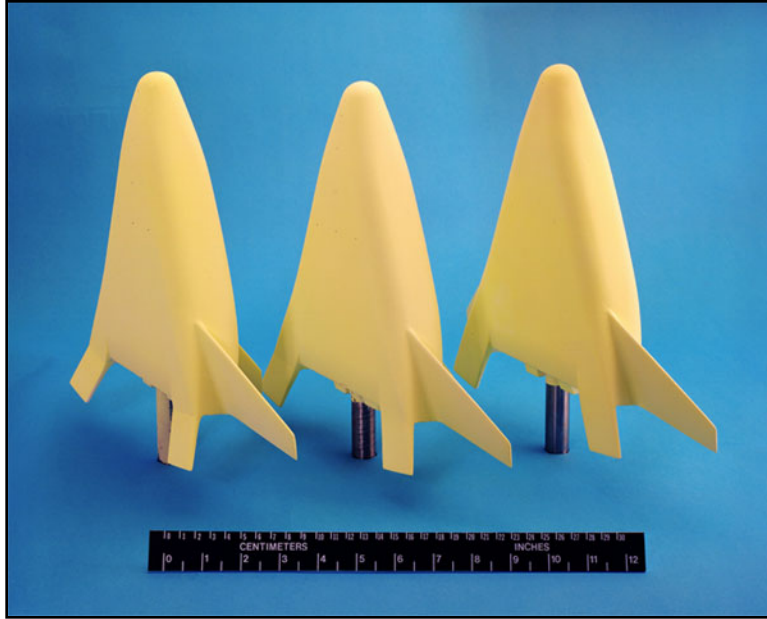
Figure 14. Phosphor-coated ceramic X-33 models.
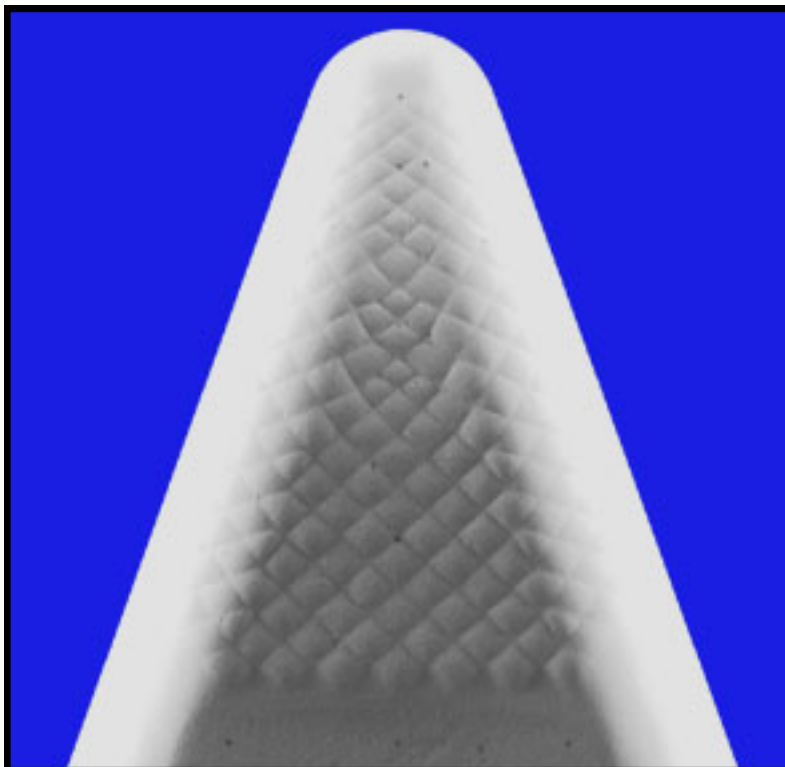
Figure 15. Closeup of X-33 ceramic model with bowed panels.
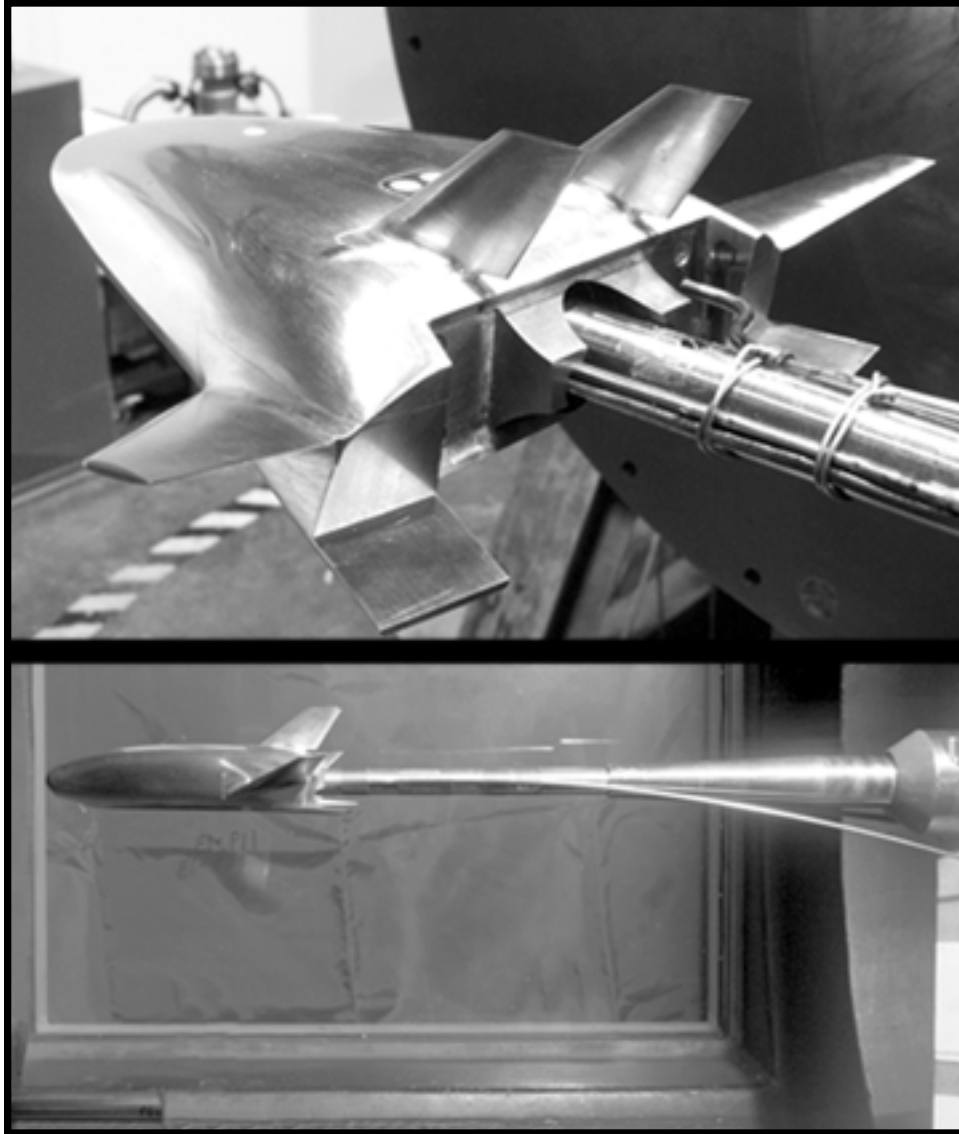
Figure 16. Metallic force and moment X-33 model with sting mount; closeup (top) and installed in tunnel (bottom).
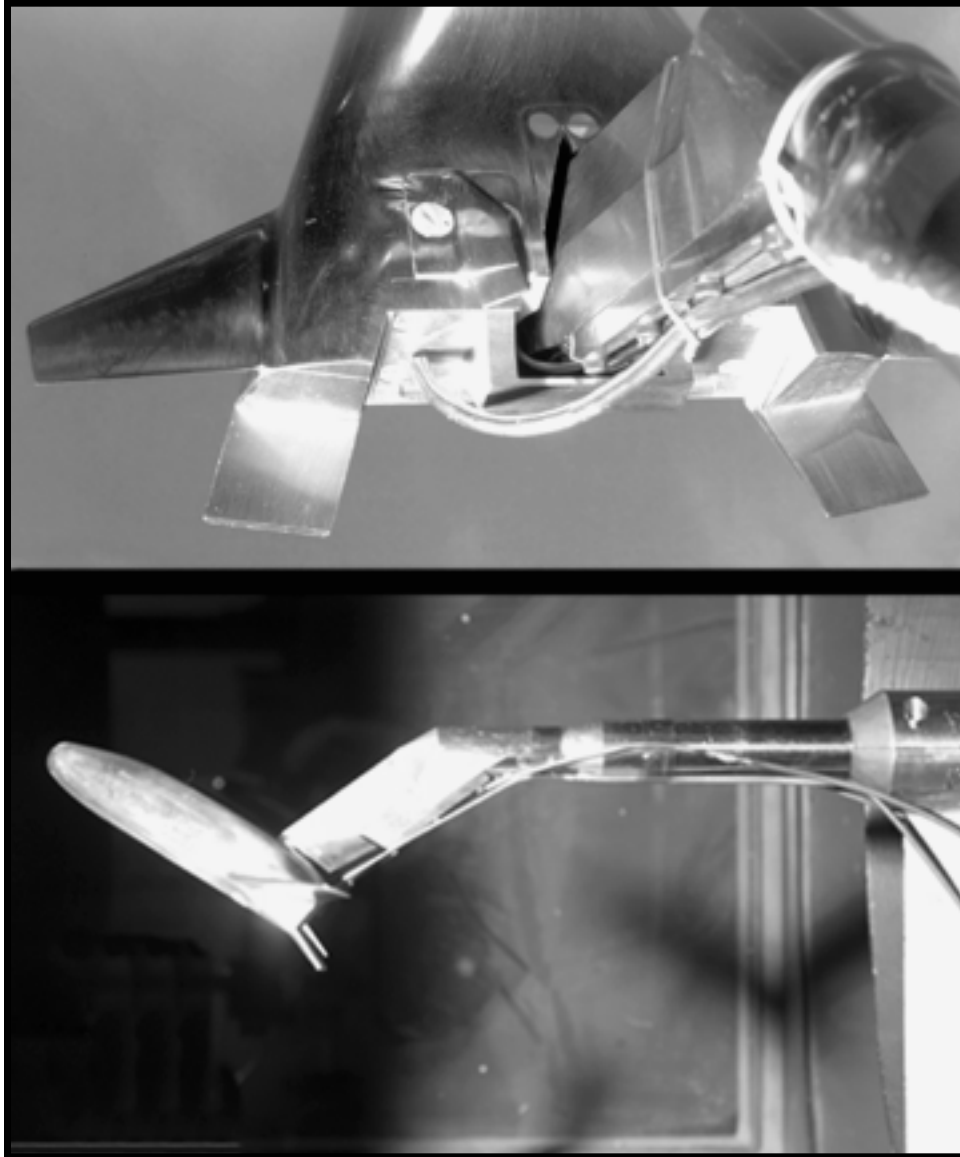
Figure 17. Metallic force and moment X-33 model with blade mount; closeup (top) and installed in tunnel (bottom).
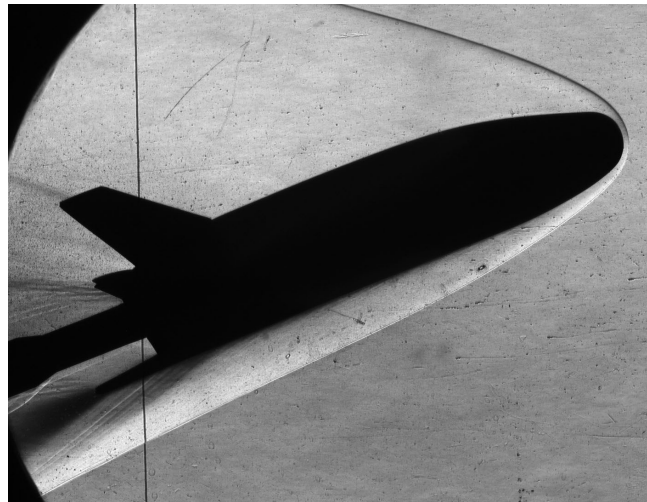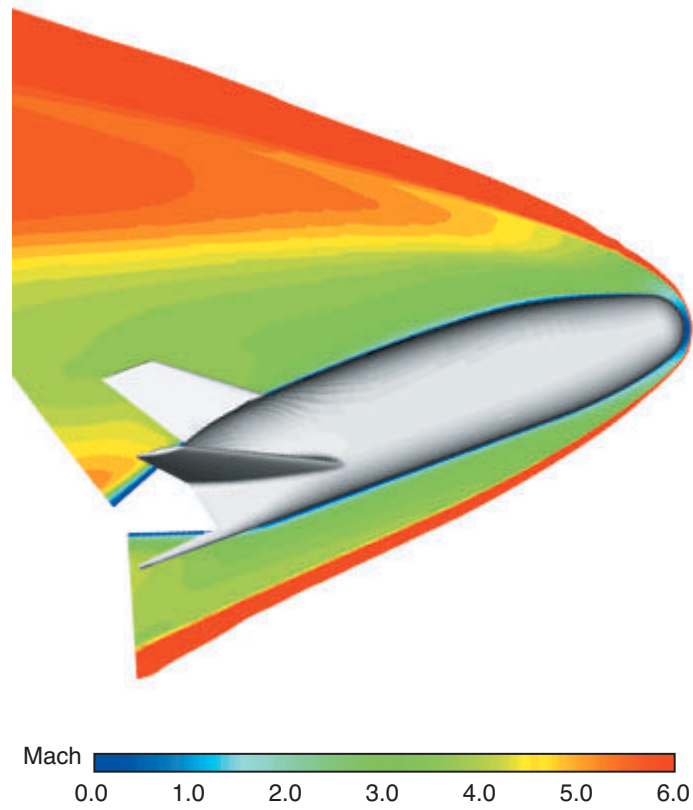
Figure 18. Mach number contours computed with GASP at Mach 6 wind-tunnel conditions and wind-tunnel schlieren image, $\alpha = 20°$.
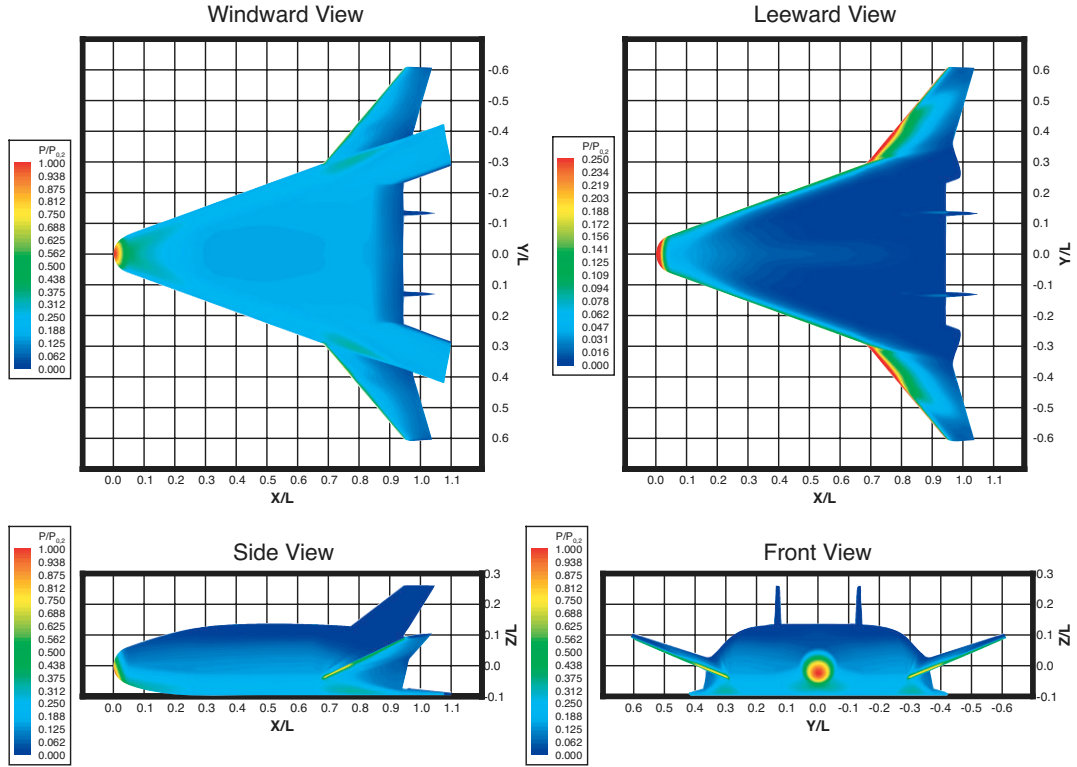
Figure 19. Surface pressures computed with GASP, Mach 6 wind-tunnel conditions, $\alpha = 20°$.
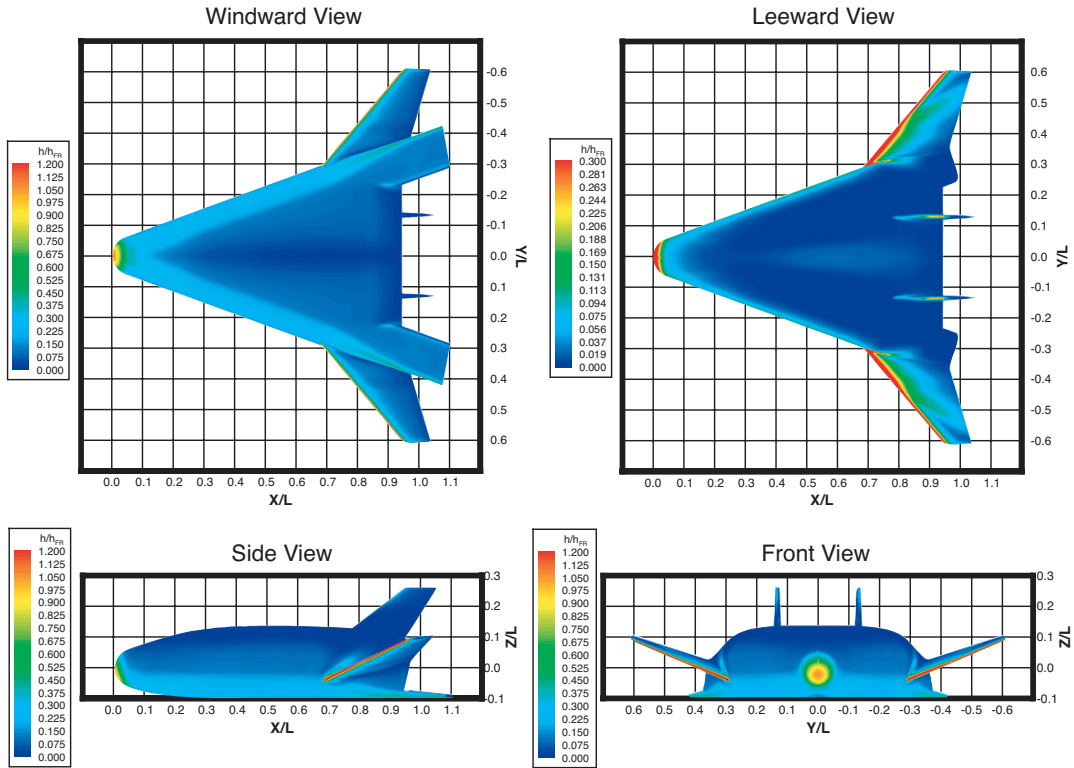
Figure 20. Surface heating computed with GASP, Mach 6 wind-tunnel conditions, $\alpha = 20°$.

Windward View

Leeward View

Side View

Front View

Oil Flow, Windward View
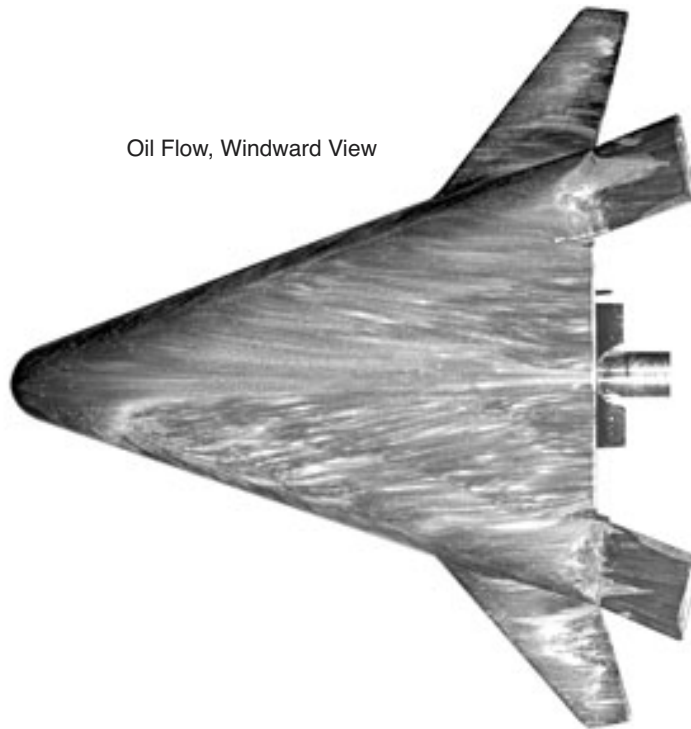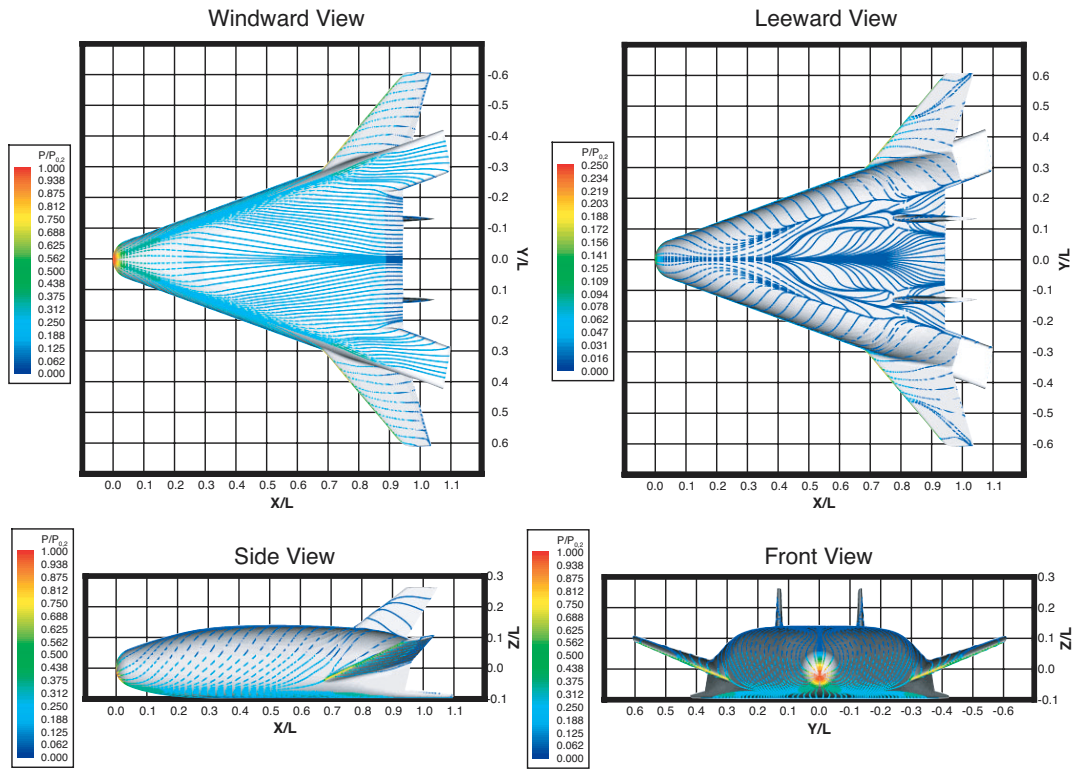
Figure 21. Surface streamlines computed with GASP at Mach 6 wind-tunnel conditions and wind-tunnel oil flow image, $\alpha = 20°$.
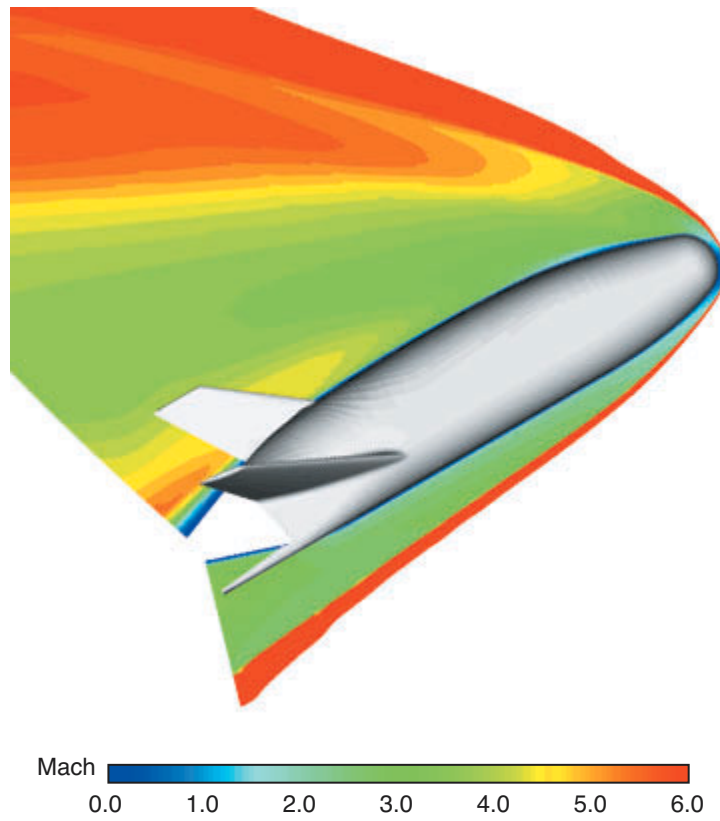
Figure 22. Mach number contours computed with GASP at Mach 6 wind-tunnel conditions and wind-tunnel schlieren image, $\alpha = 30°$.
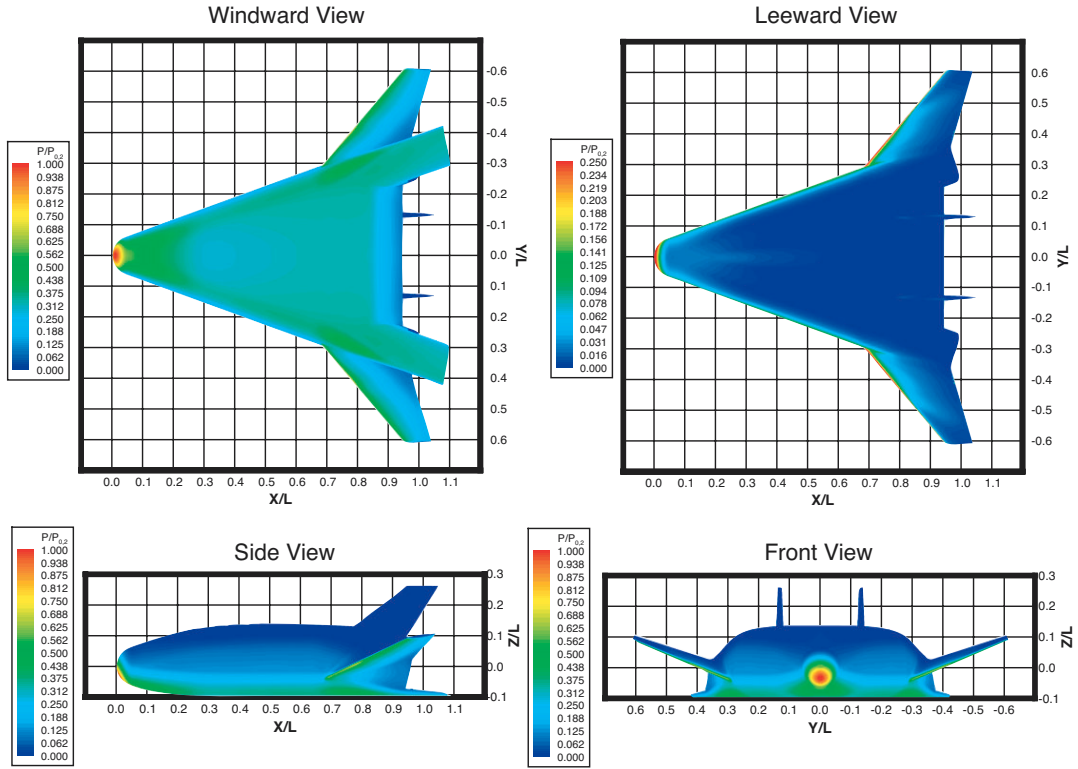
Figure 23. Surface pressures computed with GASP, Mach 6 wind-tunnel conditions, α = 30°.
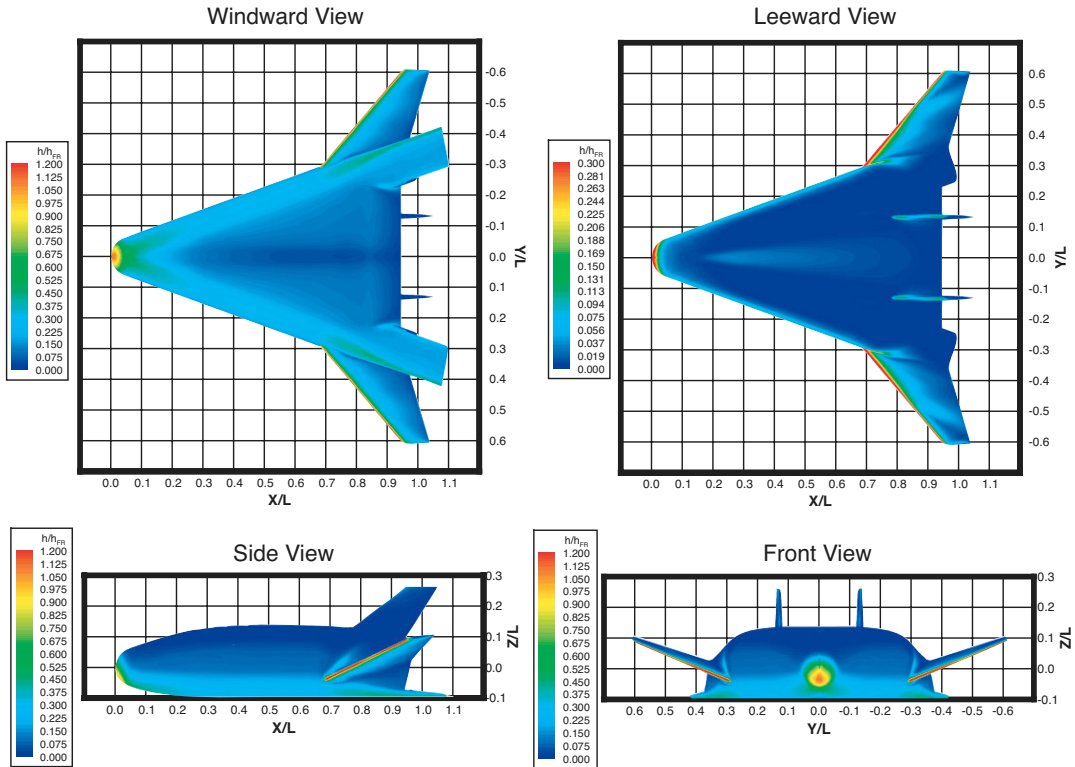
Figure 24. Surface heating computed with GASP, Mach 6 wind-tunnel conditions, α = 30°.
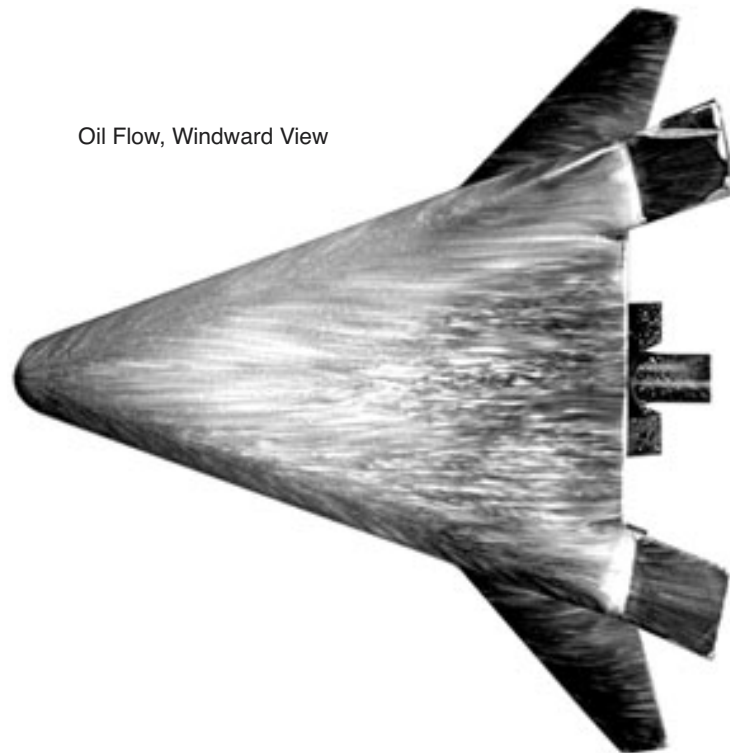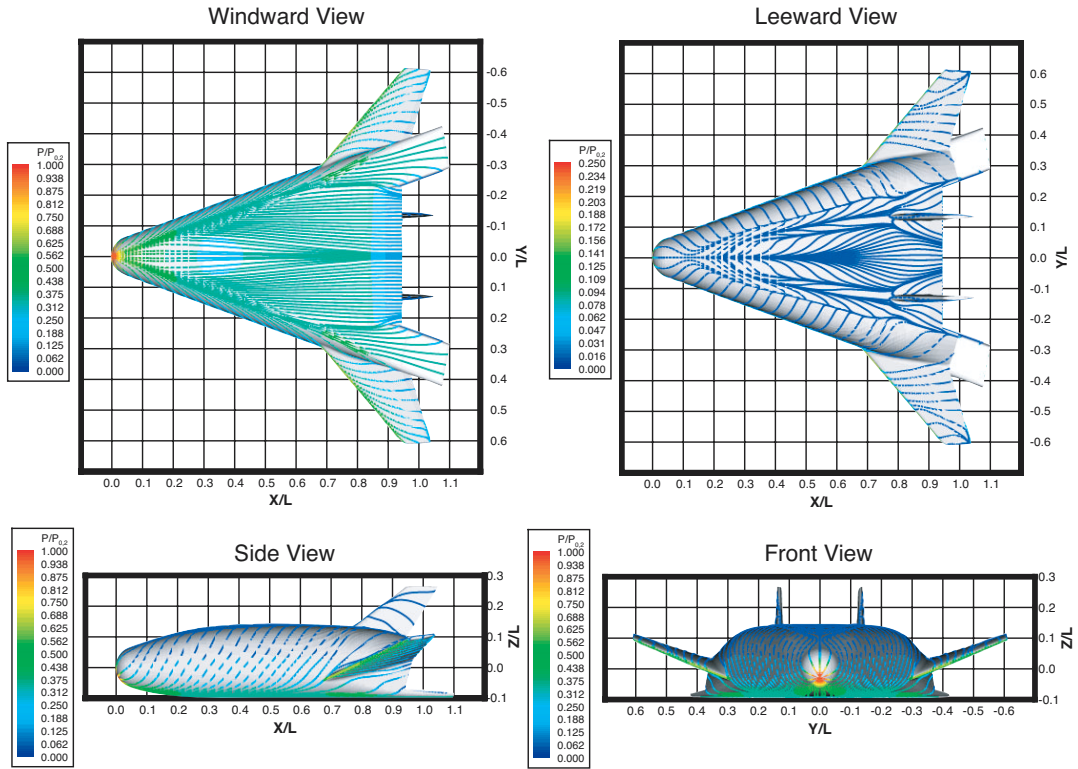
Figure 25. Surface streamlines computed with GASP at Mach 6 wind-tunnel conditions and wind-tunnel oil flow image, $\alpha = 30°$.
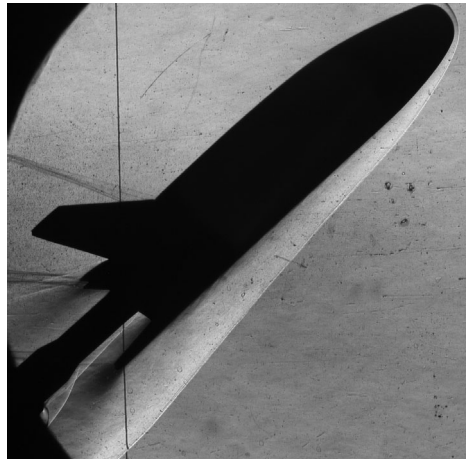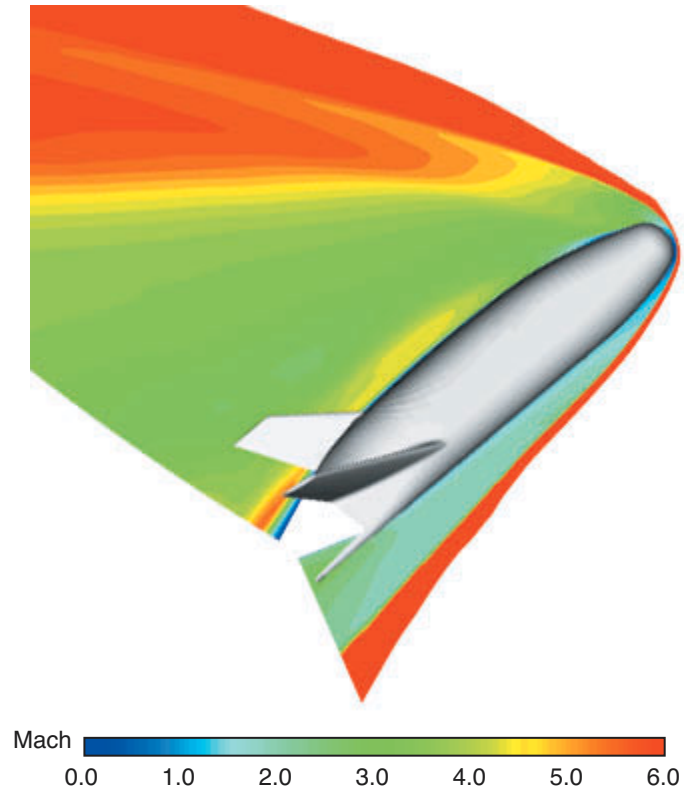
Figure 26. Mach number contours computed with GASP at Mach 6 wind-tunnel conditions and wind-tunnel schlieren image, $\alpha = 40°$.
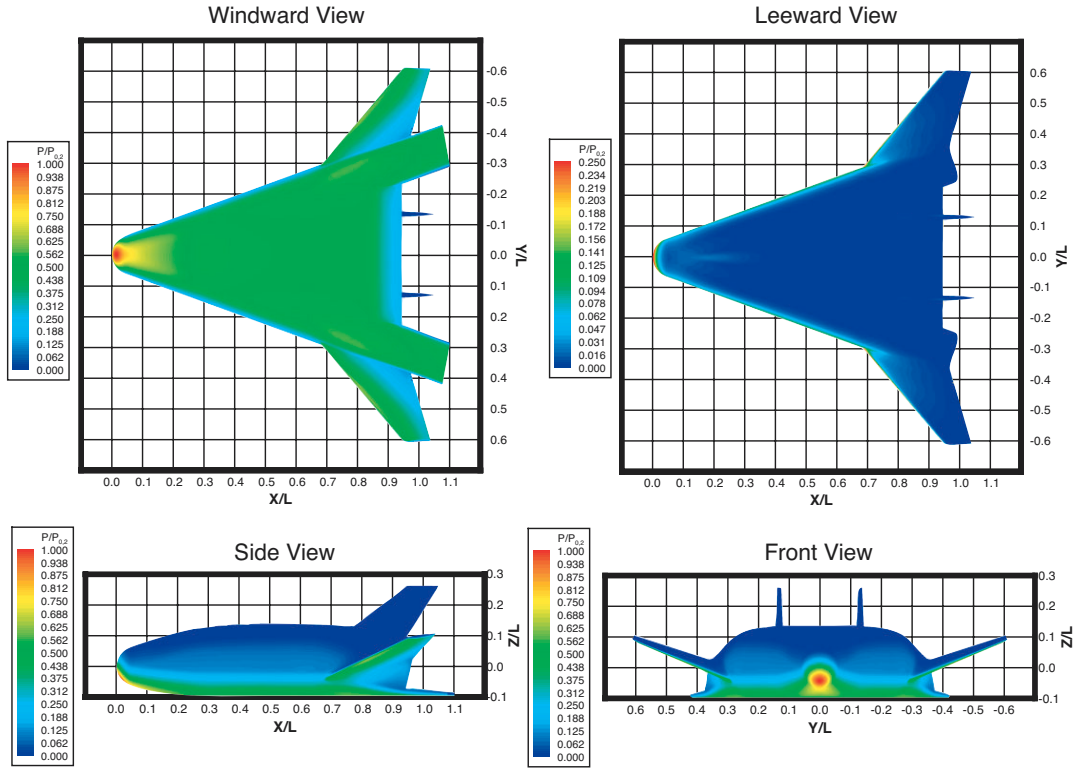
Figure 27. Surface pressures computed with GASP, Mach 6 wind-tunnel conditions, $\alpha = 40°$.
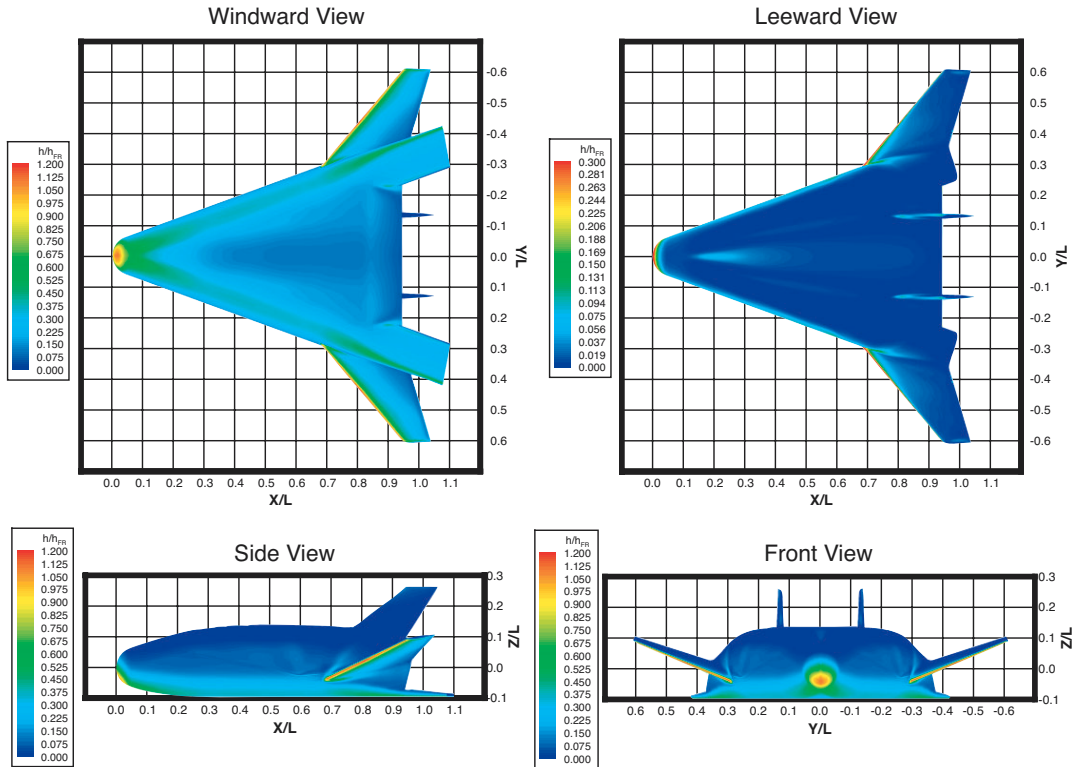
Figure 28. Surface heating computed with GASP, Mach 6 wind-tunnel conditions, $\alpha = 40°$.
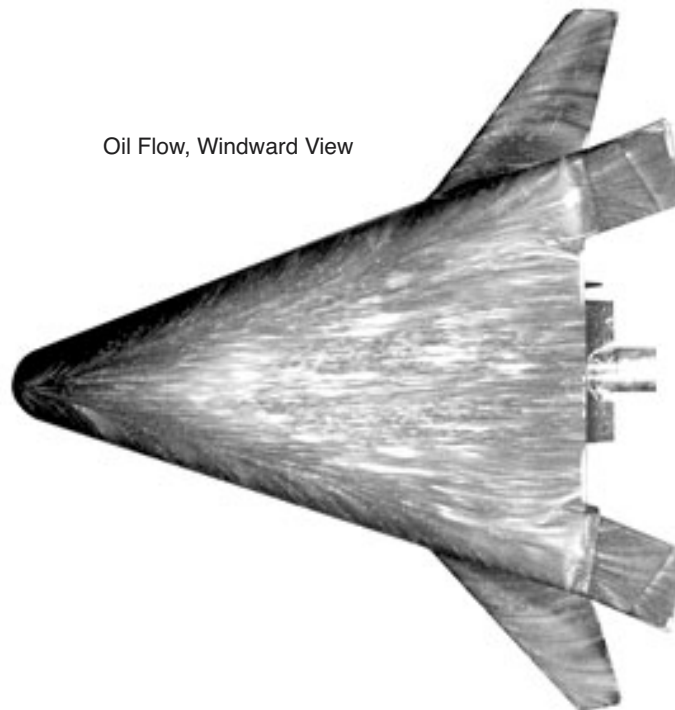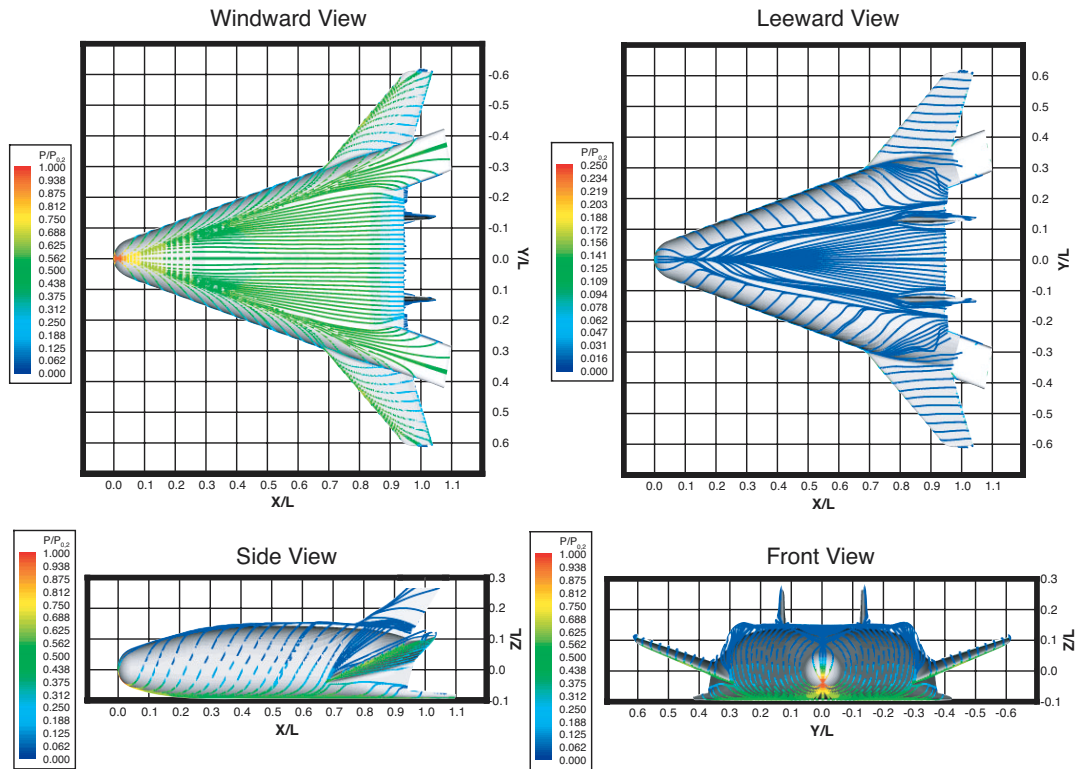
Figure 29. Surface streamlines computed with GASP at Mach 6 wind-tunnel conditions and wind-tunnel oil flow image, $\alpha = 40°$.
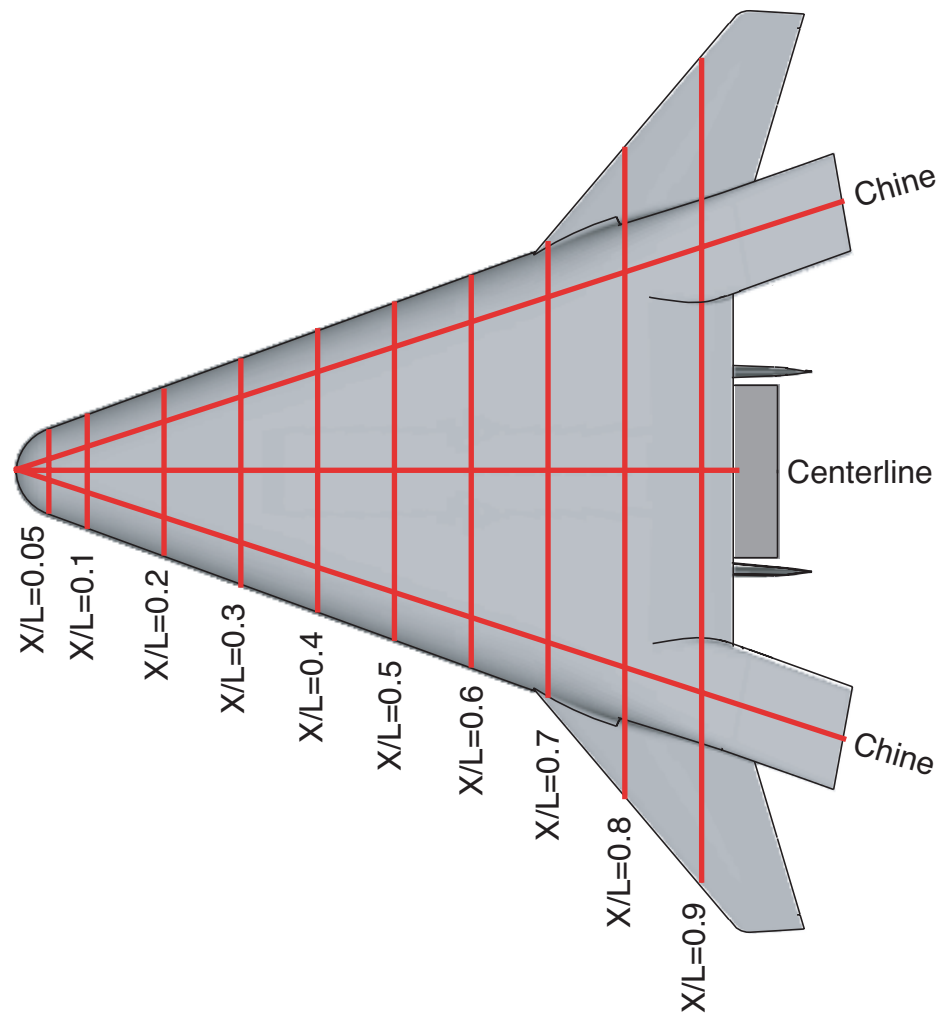
Figure 30. Cut locations for comparisons between experimental and computational heating data.
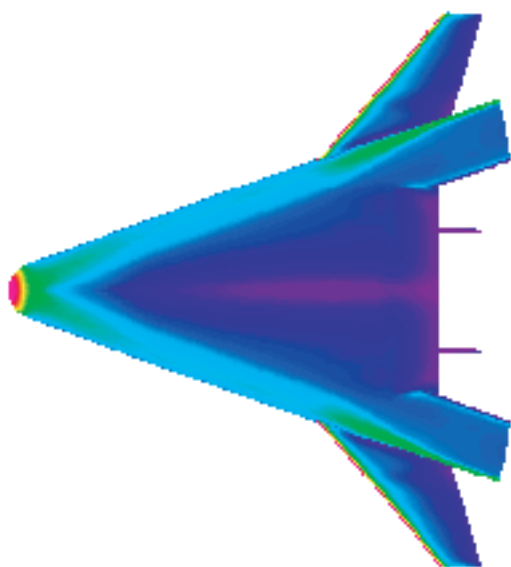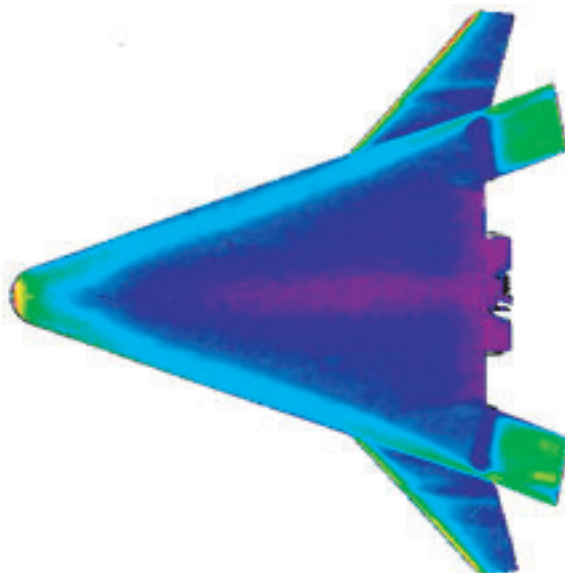
GASP Laminar Solution, Re_inf = 4E6/ft   Test 6763, Run 056, Re_inf = 2E6/ft

Note: All Experimental data
are for δ_{BF} = +10-deg
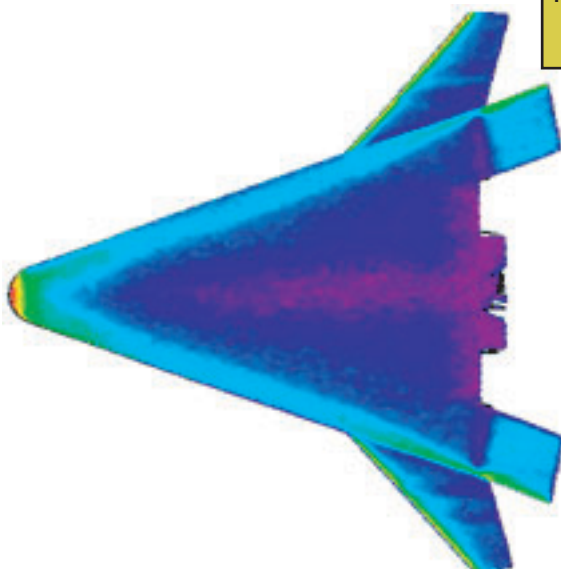
Test 6763, Run 055, Re_inf = 1E6/ft   Test 6763, Run 057, Re_inf = 4E6/ft
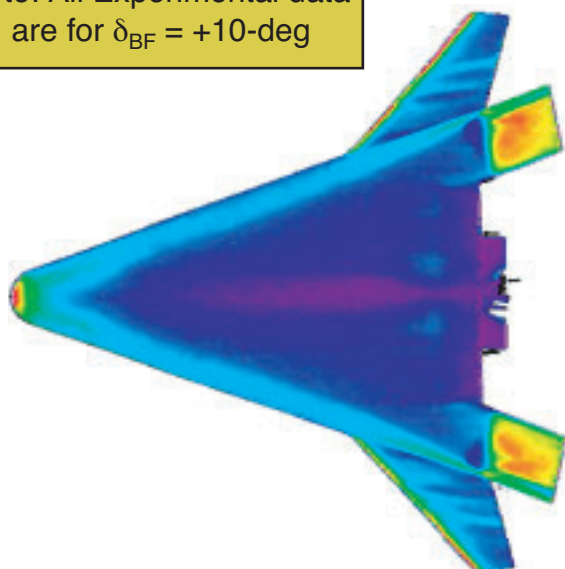
h/h_{FR}

0.0   0.1   0.2   0.3   0.4   0.5   0.6   0.7   0.8   0.9   1.0
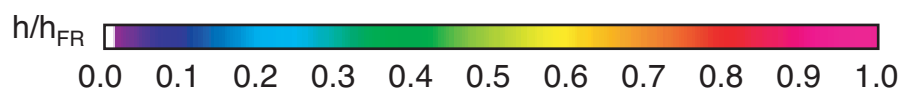
Figure 31. Graphical depiction of GASP laminar solution and heating data on smooth models, windward surface, Mach 6, $\alpha = 20°$, $\delta_{BF} = 0°$.
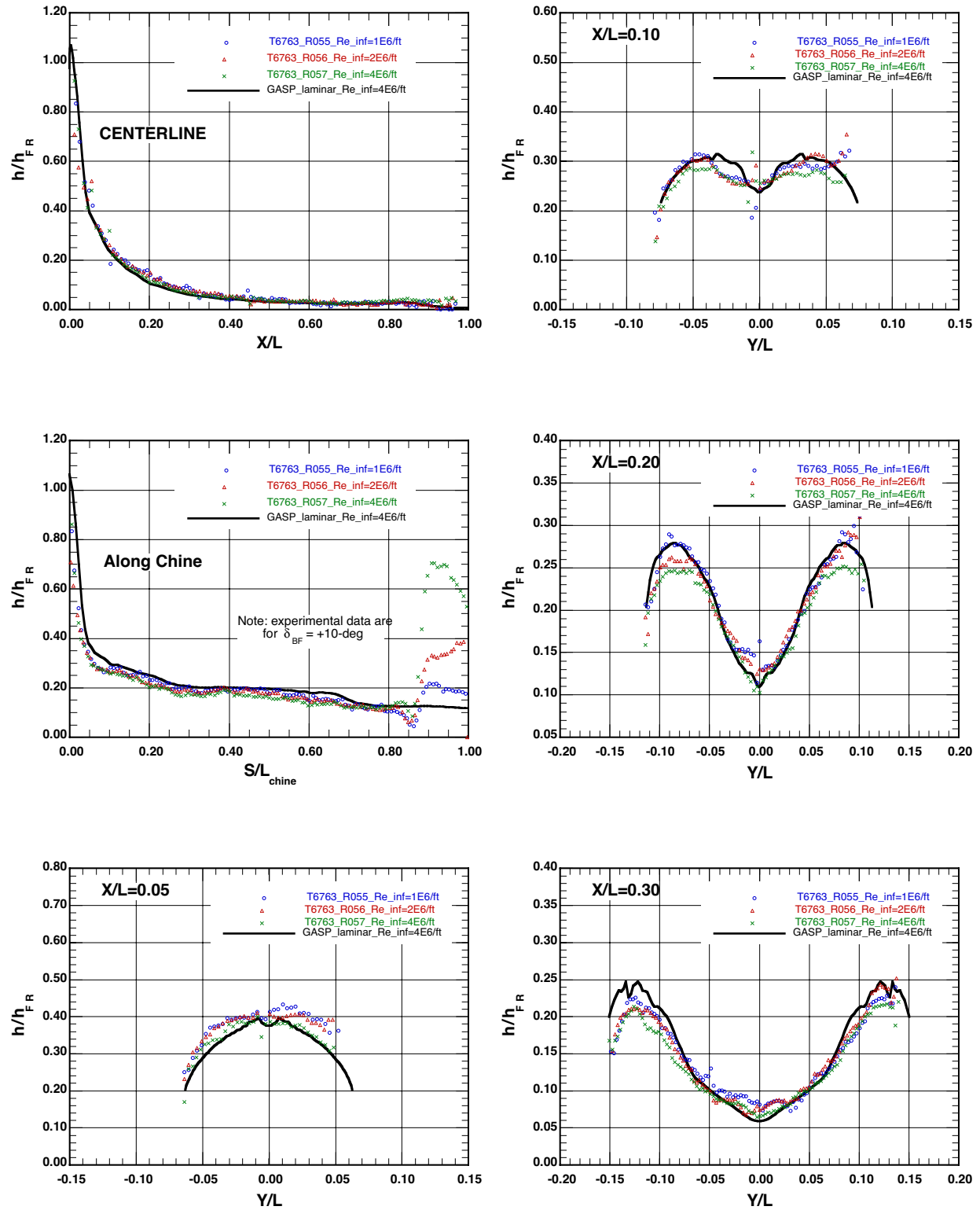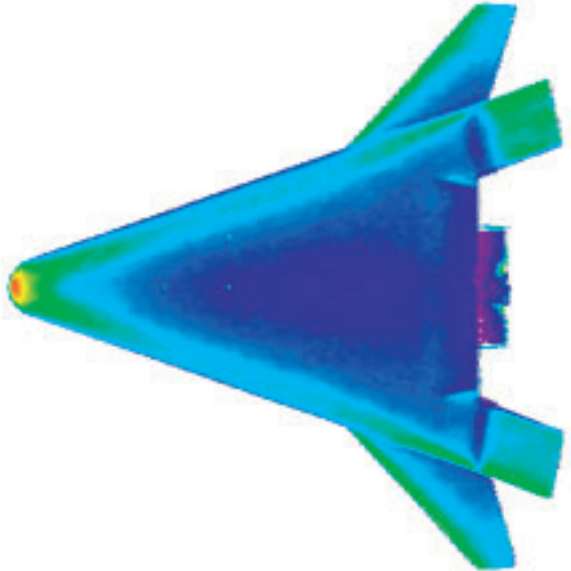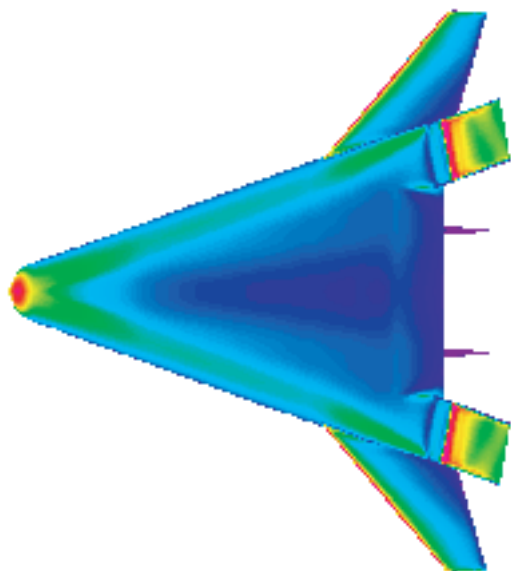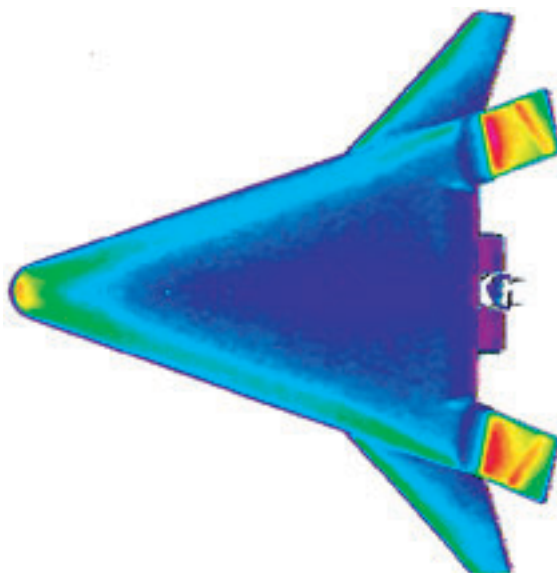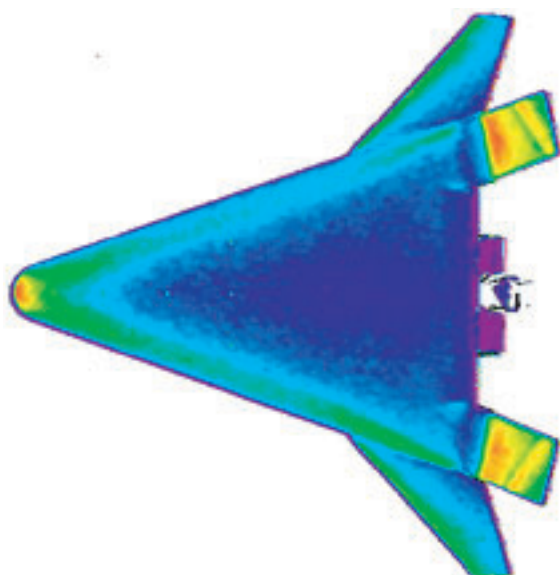
Figure 32. GASP laminar computation versus heating data on smooth models at Mach 6, $\alpha = 20°$, $\delta_{BF} = 0°$; centerline, chine, and axial cuts to $X/L = 0.30$.
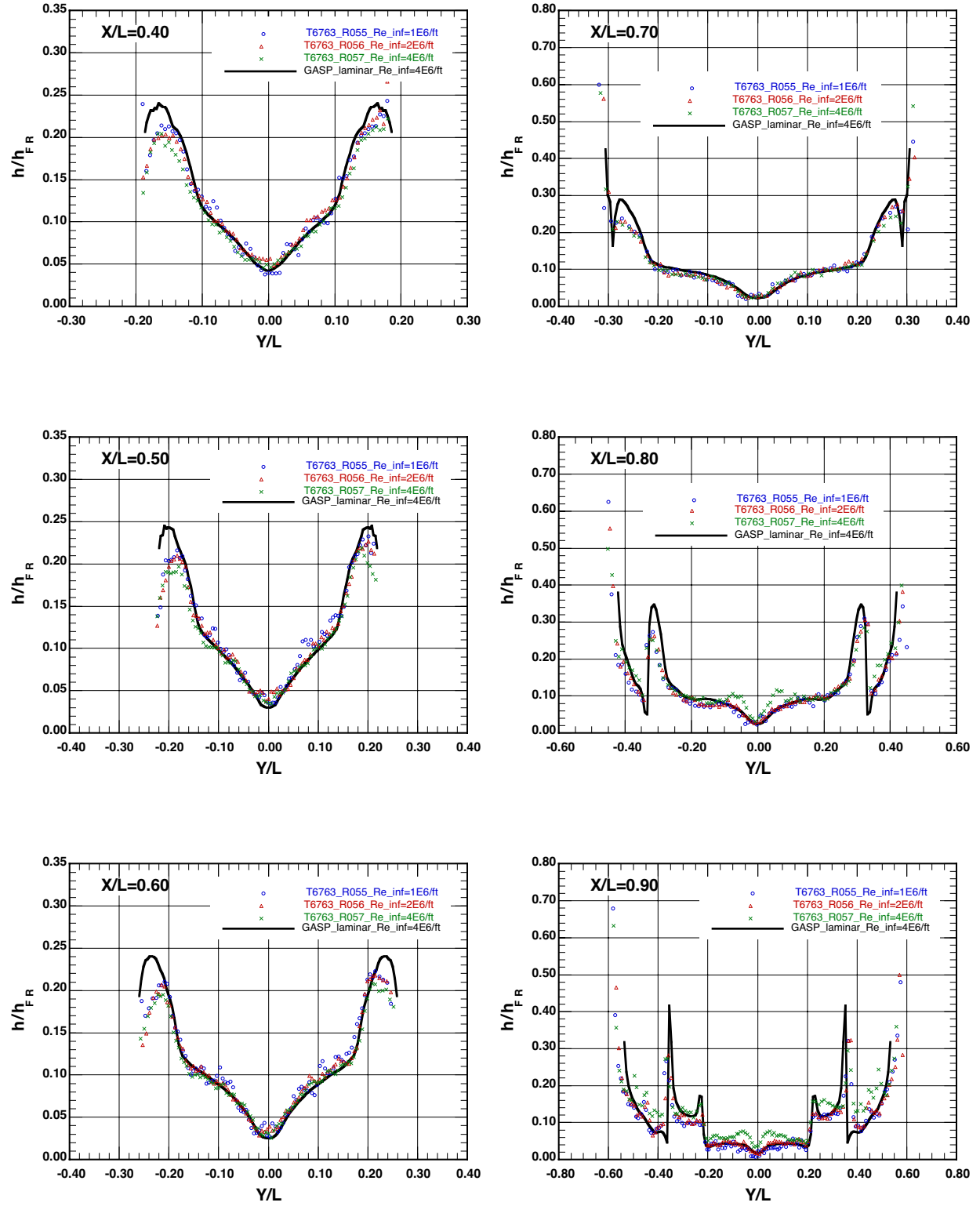
Figure 33. GASP laminar computation versus heating data on smooth models at Mach 6, $\alpha = 20°$, $\delta_{BF} = 0°$; axial cuts from $X/L = 0.40$ to $X/L = 0.90$.
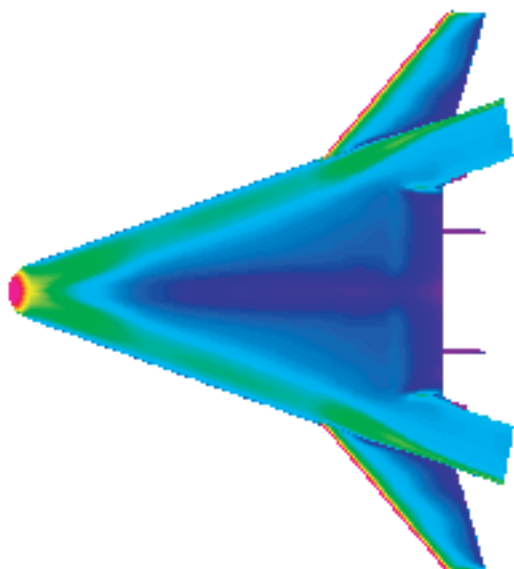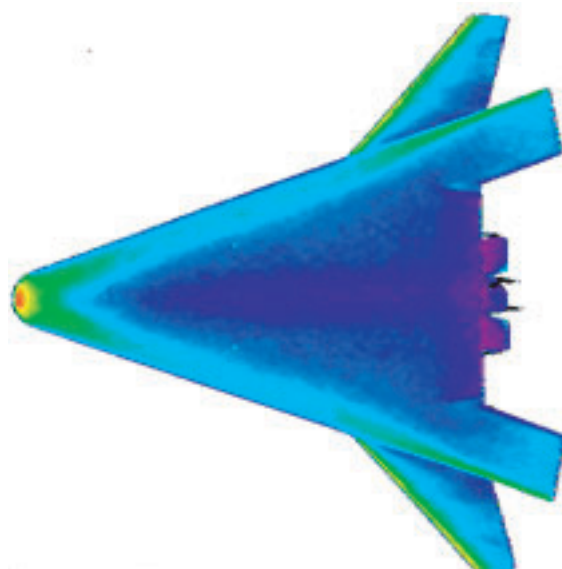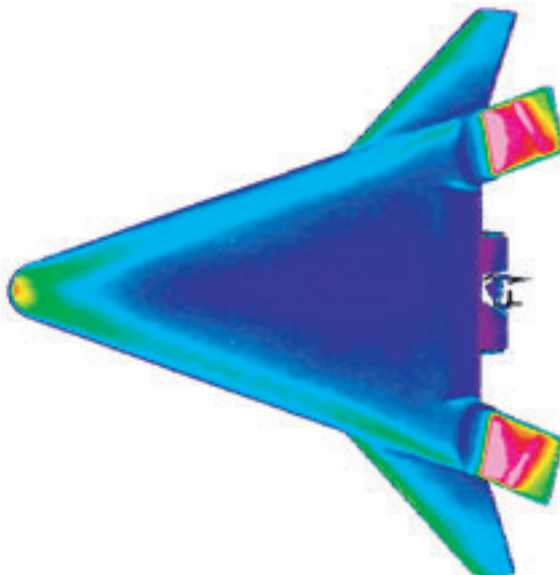
GASP Laminar Solution, Re_inf = 4E6/ft   Test 6763, Run 053, Re_inf = 2E6/ft
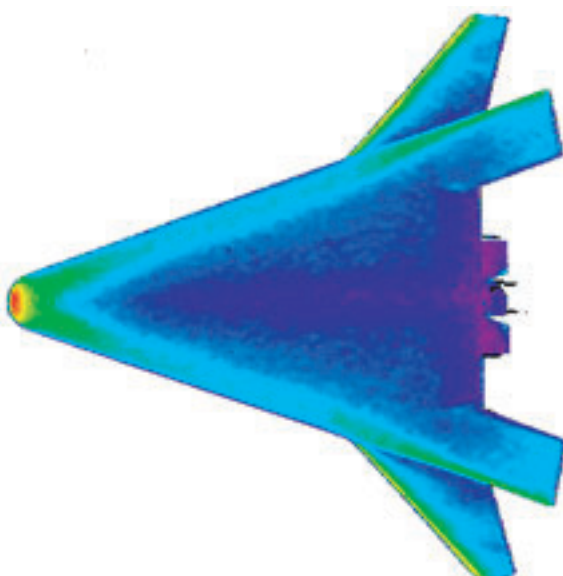
Test 6763, Run 054, Re_inf = 1E6/ft   Test 6763, Run 052, Re_inf = 4E6/ft
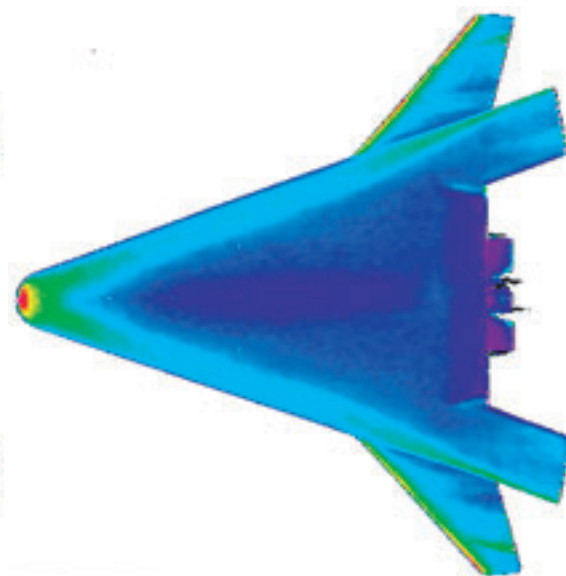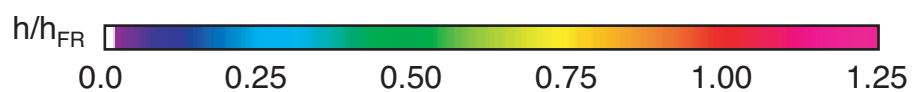
h/h_{FR}

0.0   0.1   0.2   0.3   0.4   0.5   0.6   0.7   0.8   0.9   1.0
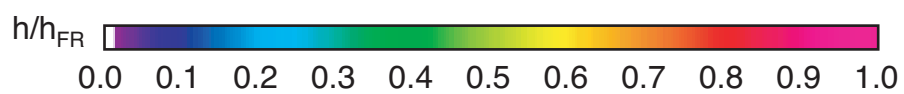
Figure 34. Graphical depiction of GASP laminar solution and heating data on smooth models, windward surface, Mach 6, $\alpha = 30°$, $\delta_{BF} = 0°$.
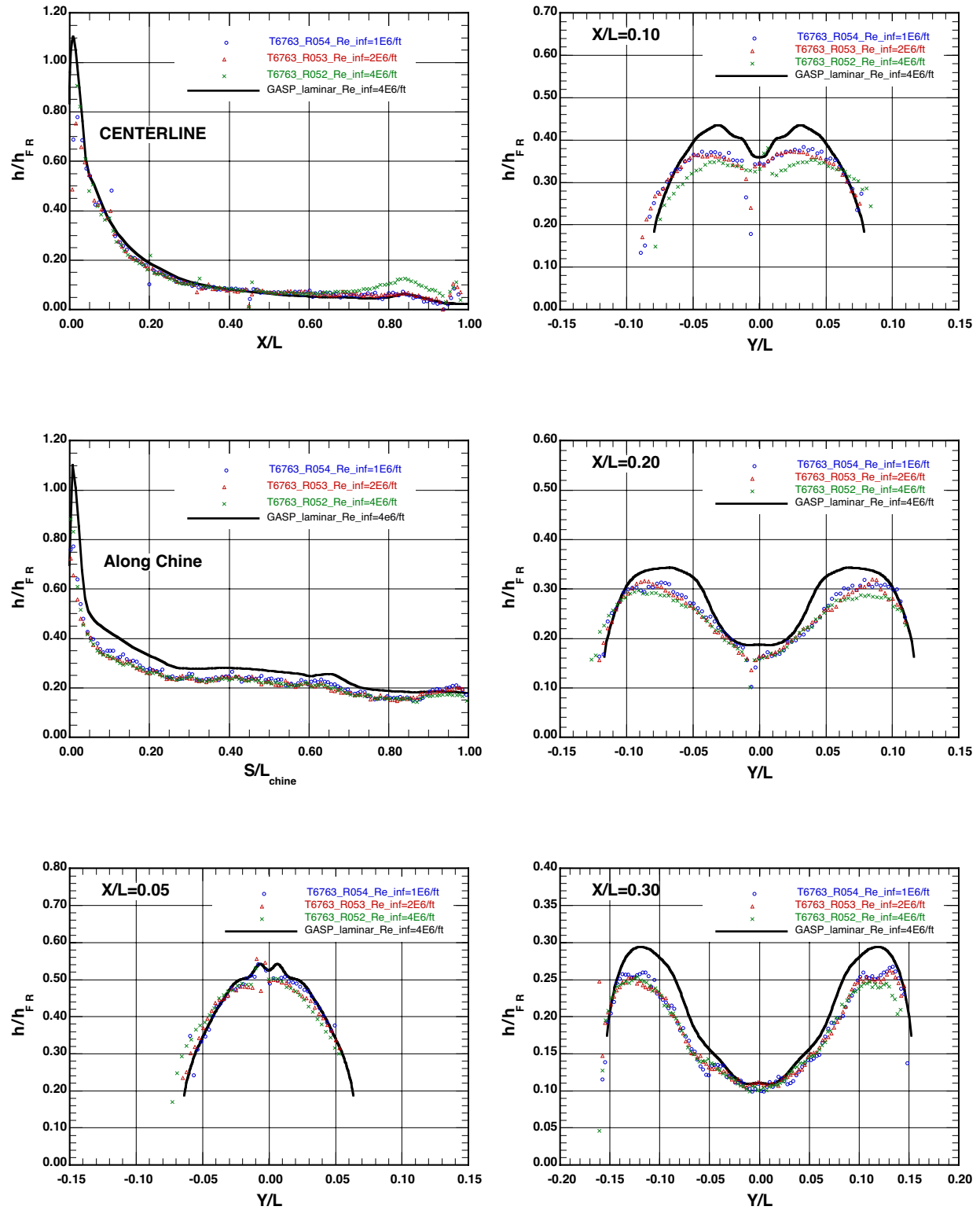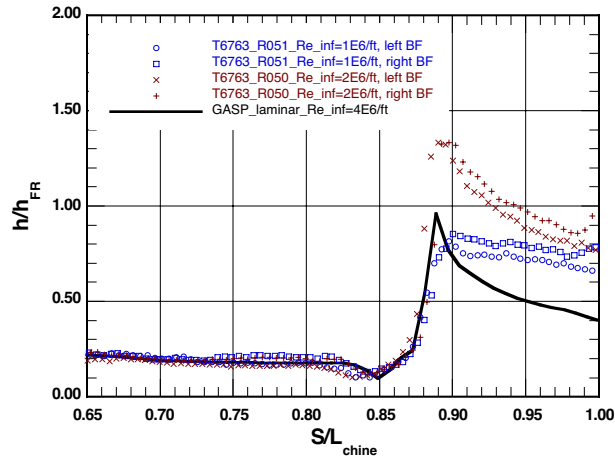
Figure 35. GASP laminar computation versus heating data on smooth models at Mach 6, $\alpha = 30°$, $\delta_{BF} = 0°$; center-line, chine, and axial cuts to $X/L = 0.30$.
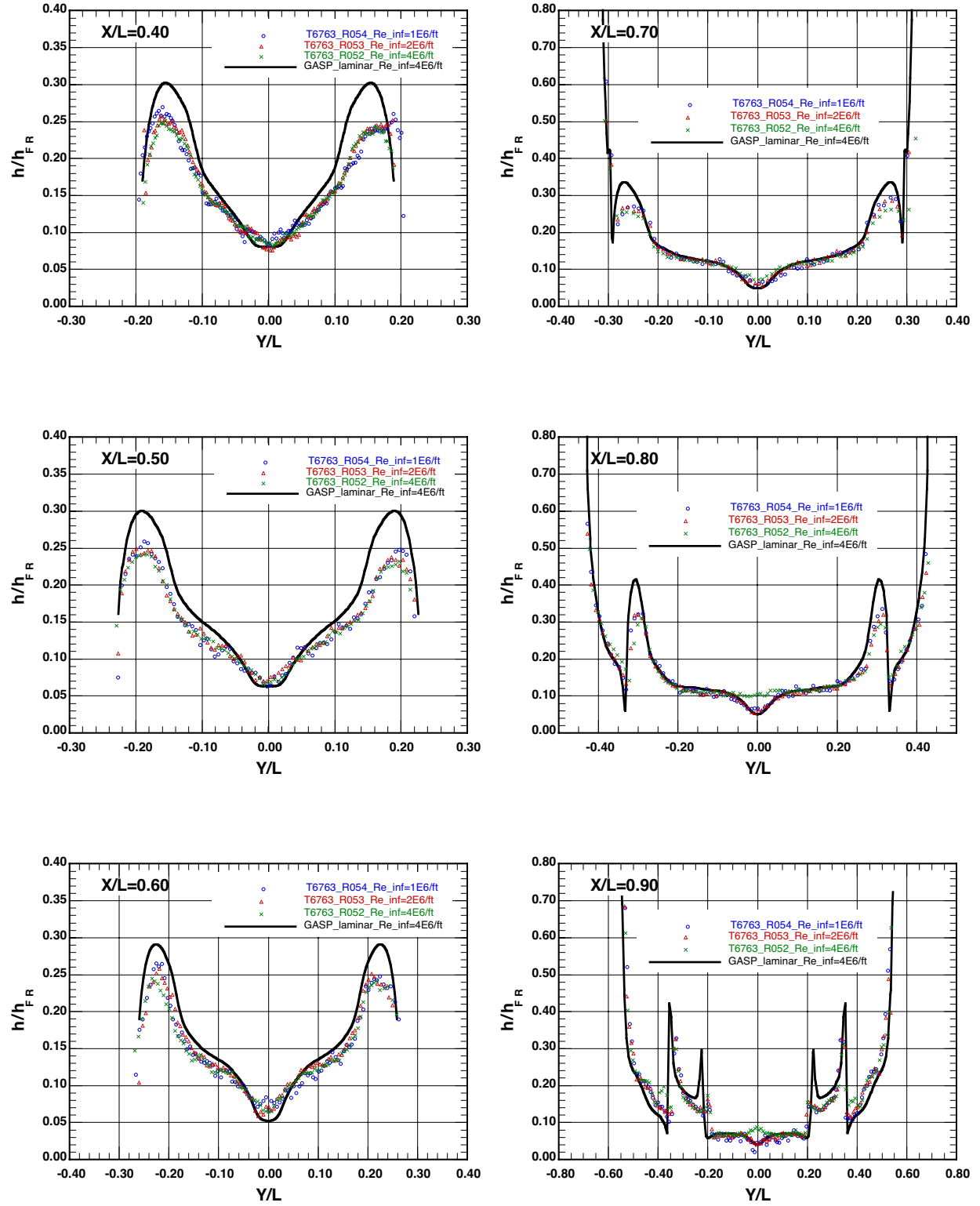
Figure 36. GASP laminar computation versus wind heating data on smooth models at Mach 6, $\alpha = 30°$, $\delta_{BF} = 0°$; axial cuts from $X/L = 0.40$ to $X/L = 0.90$.

GASP Laminar Solution, Re_inf = 4E6/ft

Test 6763, Run 036, Re_inf = 2E6/ft

Test 6763, Run 037, Re_inf = 1E6/ft

Test 6763, Run 035, Re_inf = 4E6/ft

h/h_{FR}

0.0 0.1 0.2 0.3 0.4 0.5 0.6 0.7 0.8 0.9 1.0
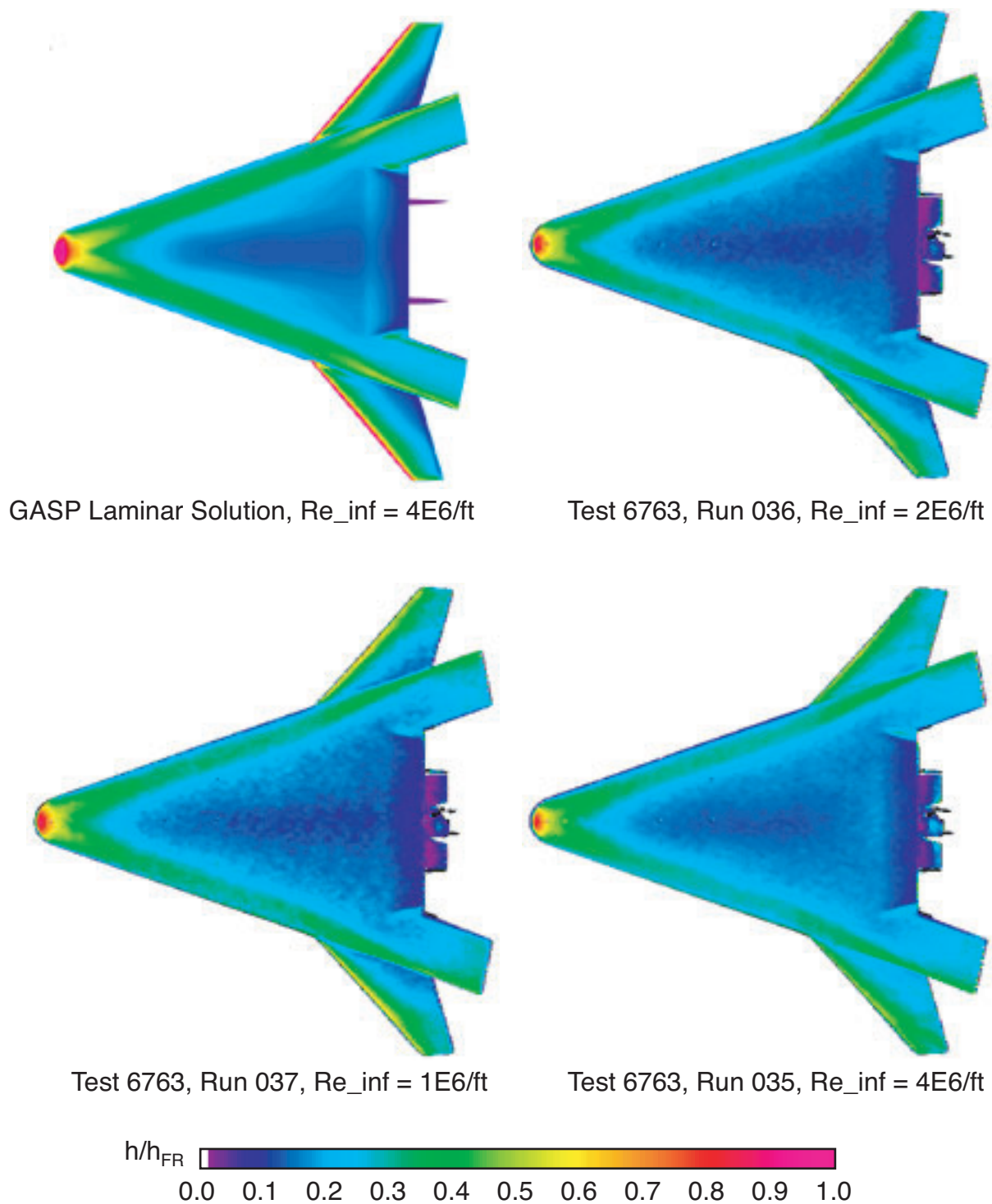
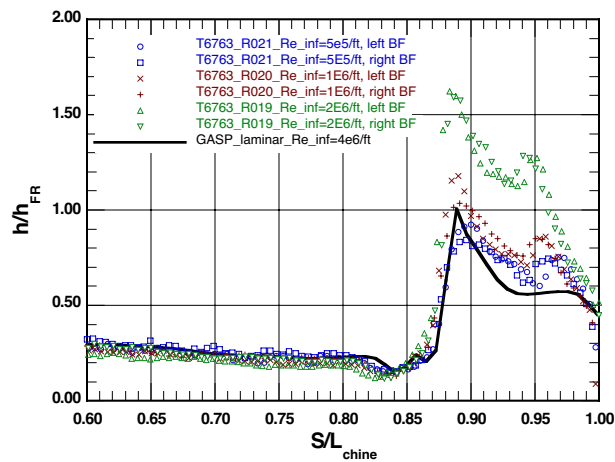Figure 37. Graphical depiction of GASP laminar solution and heating data on smooth models, windward surface, Mach 6, $\alpha = 40°$, $\delta_{BF} = 0°$.
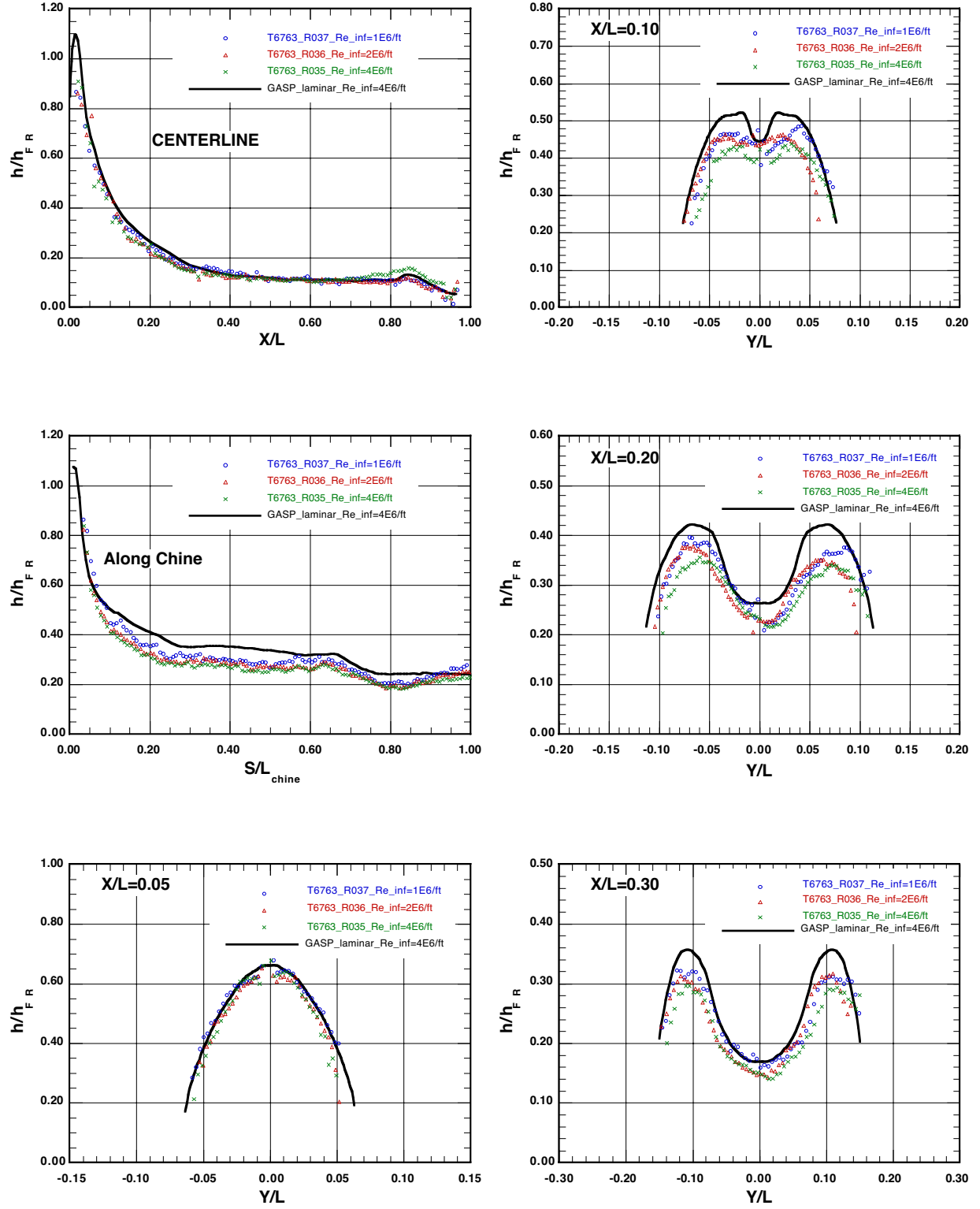
Figure 38. GASP laminar computation versus heating data on smooth models at Mach 6, $\alpha = 40°$, $\delta_{BF} = 0°$; center-line, chine, and axial cuts to $X/L = 0.30$.
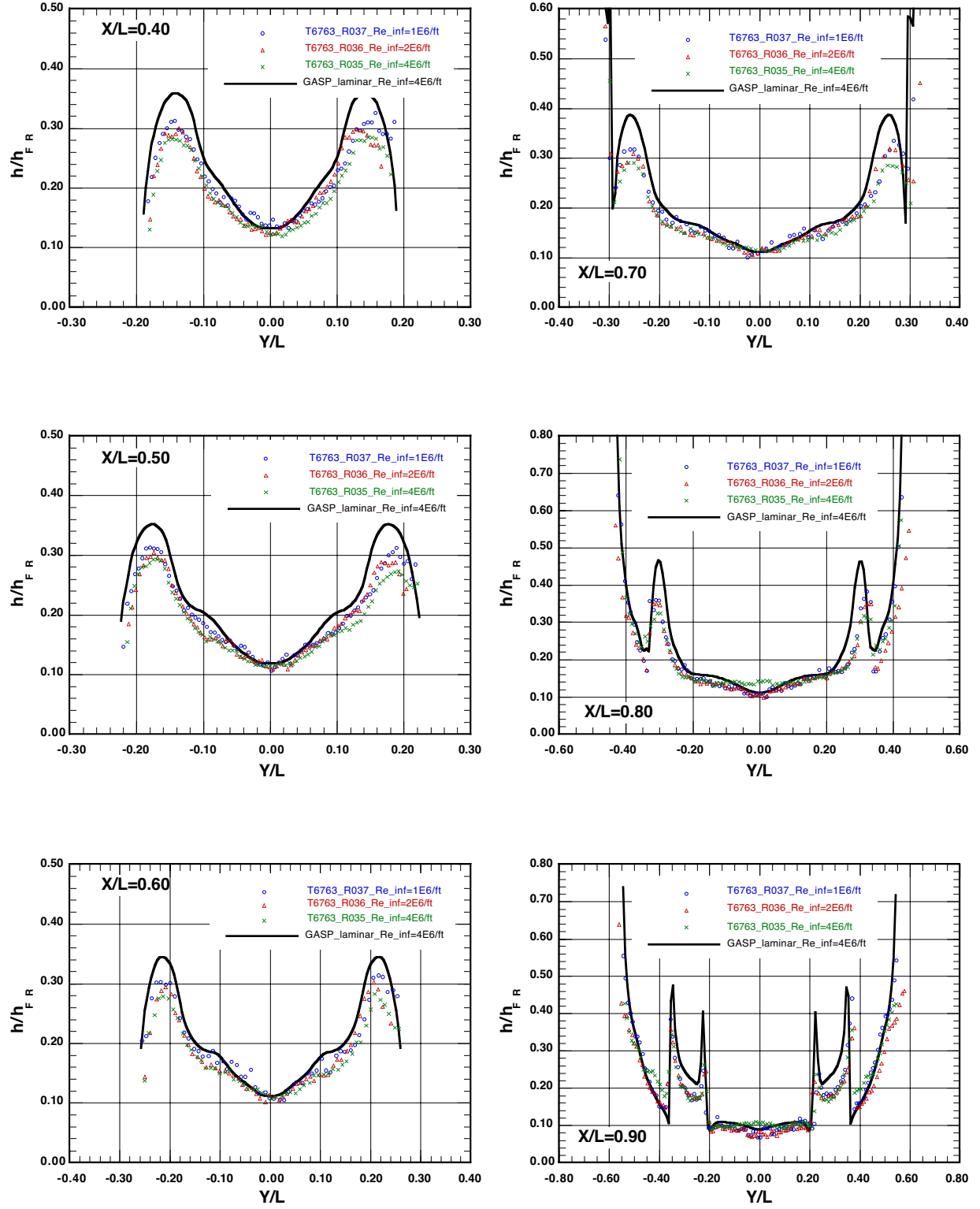
Figure 39. GASP laminar computation versus heating data on smooth models at Mach 6, $\alpha = 40°$, $\delta_{BF} = 0°$; axial cuts from $X/L = 0.40$ to $X/L = 0.90$.
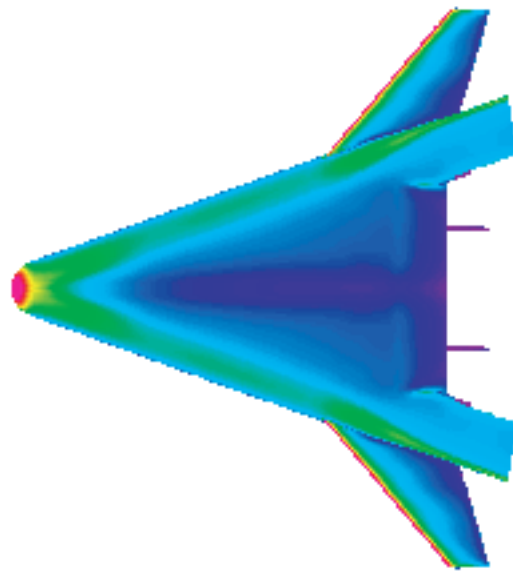
GASP Laminar Solution, Re_inf = 4E6/ft
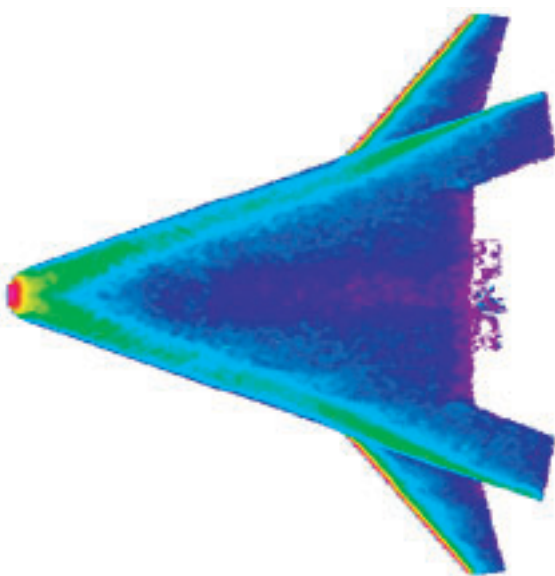
Test 6786, Run 034, Re_inf = 1E6/ft
0.006" Bowed Panel Array
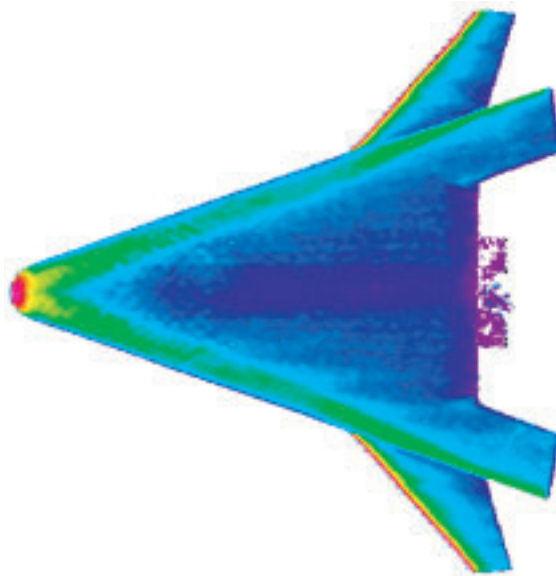
Test 6786, Run 035, Re_inf = 2E6/ft
0.006" Bowed Panel Array

h/h_{FR} 0.0   0.1   0.2   0.3   0.4   0.5   0.6   0.7   0.8   0.9   1.0
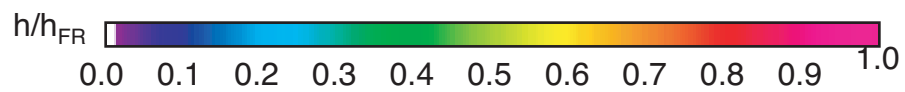
Figure 40. Graphical depiction of GASP laminar solution and heating data on bowed panel models, windward surface, Mach 6, $\alpha = 30°$, $\delta_{BF} = 0°$
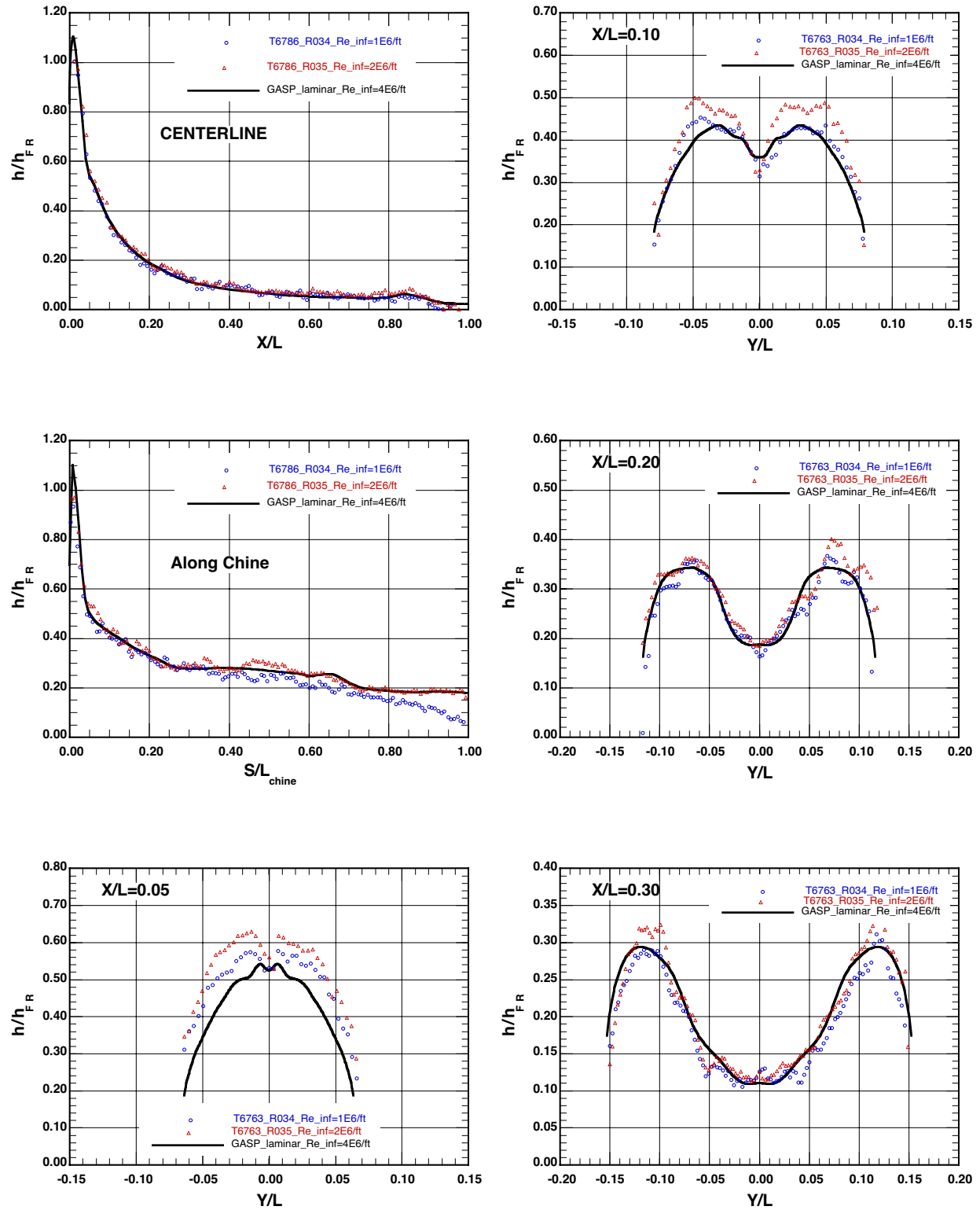
Figure 41. GASP laminar computation versus heating data on bowed panel models at Mach 6, $\alpha = 30°$, $\delta_{BF} = 0°$; centerline, chine, and axial cuts to $X/L = 0.30$.
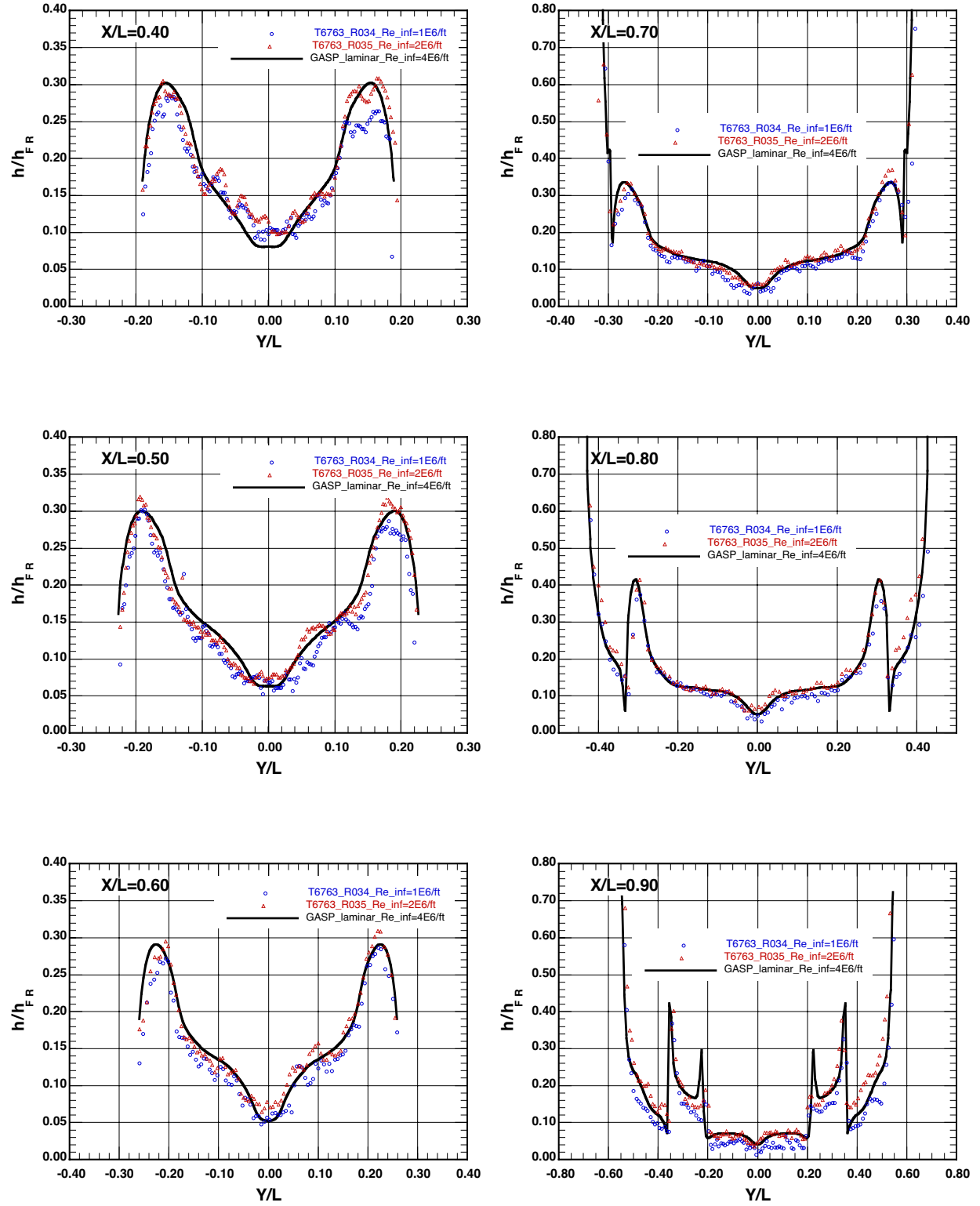
Figure 42. GASP laminar computation versus heating data on bowed panel models at Mach 6, α = 30°, δ_BF = 0°; axial cuts from *X/L* = 0.40 to *X/L* = 0.90.

49

GASP Laminar Solution, Re_inf = 4E6/ft

Test 6786, Run 010, Re_inf = 1E6/ft
0.006" Bowed Panel Array
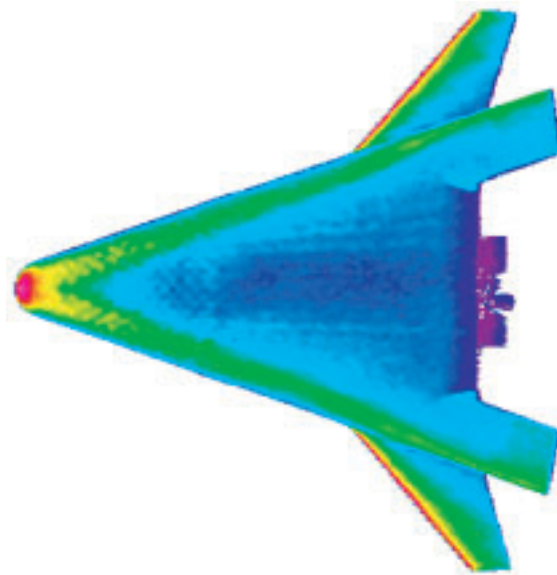
Test 6786, Run 011, Re_inf = 2E6/ft
0.006" Bowed Panel Array

h/h_{FR}

0.0   0.1   0.2   0.3   0.4   0.5   0.6   0.7   0.8   0.9   1.0
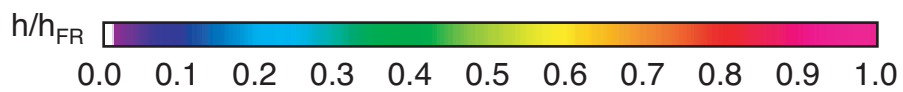
Figure 43. Graphical depiction of GASP laminar solution and heating data on bowed panels models, windward surface, Mach 6, $\alpha = 40°$, $\delta_{BF} = 0°$.
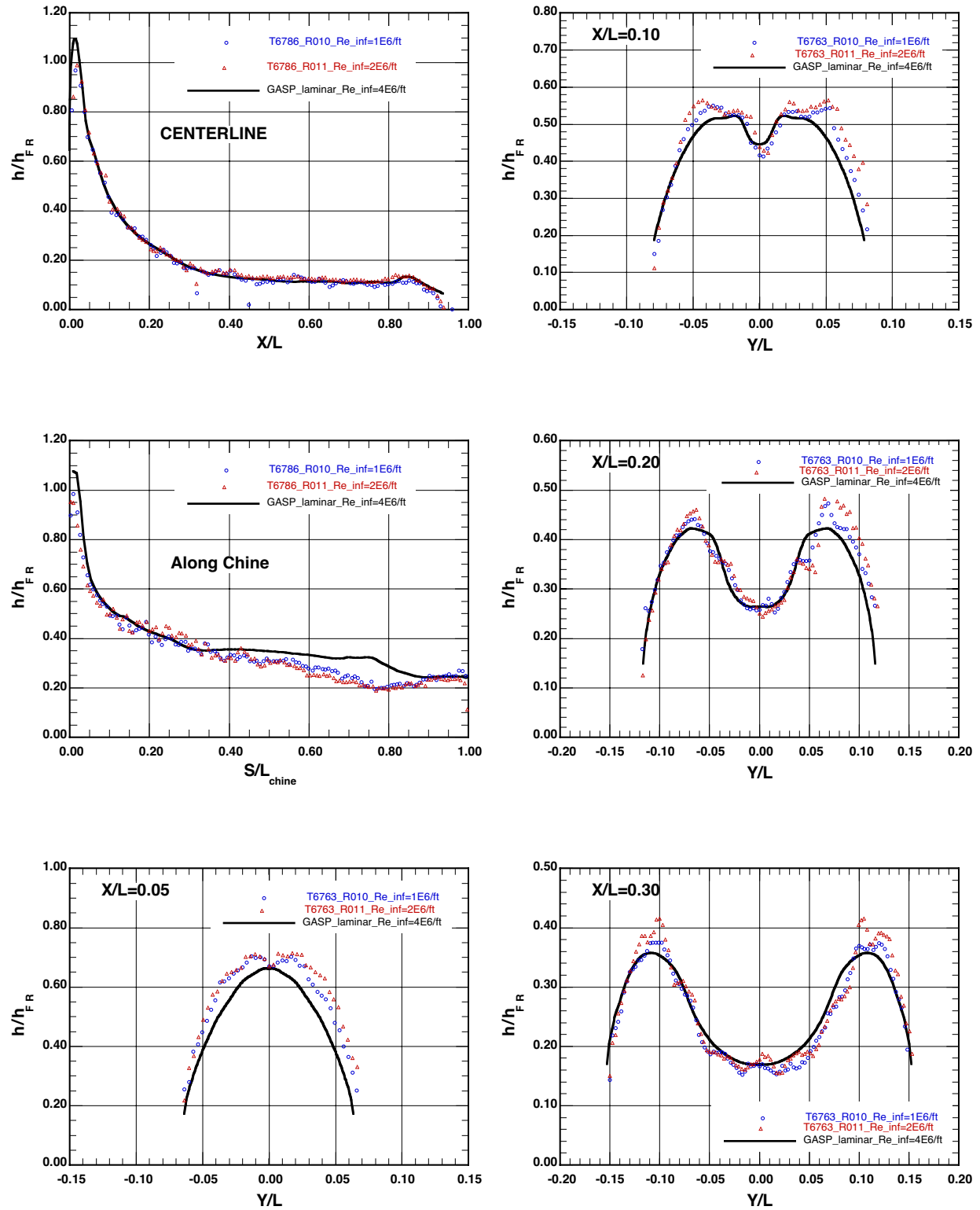
Figure 44. GASP laminar computation versus heating data on bowed panel models at Mach 6, $\alpha = 40°$, $\delta_{BF} = 0°$; centerline, chine, and axial cuts to $X/L = 0.30$.
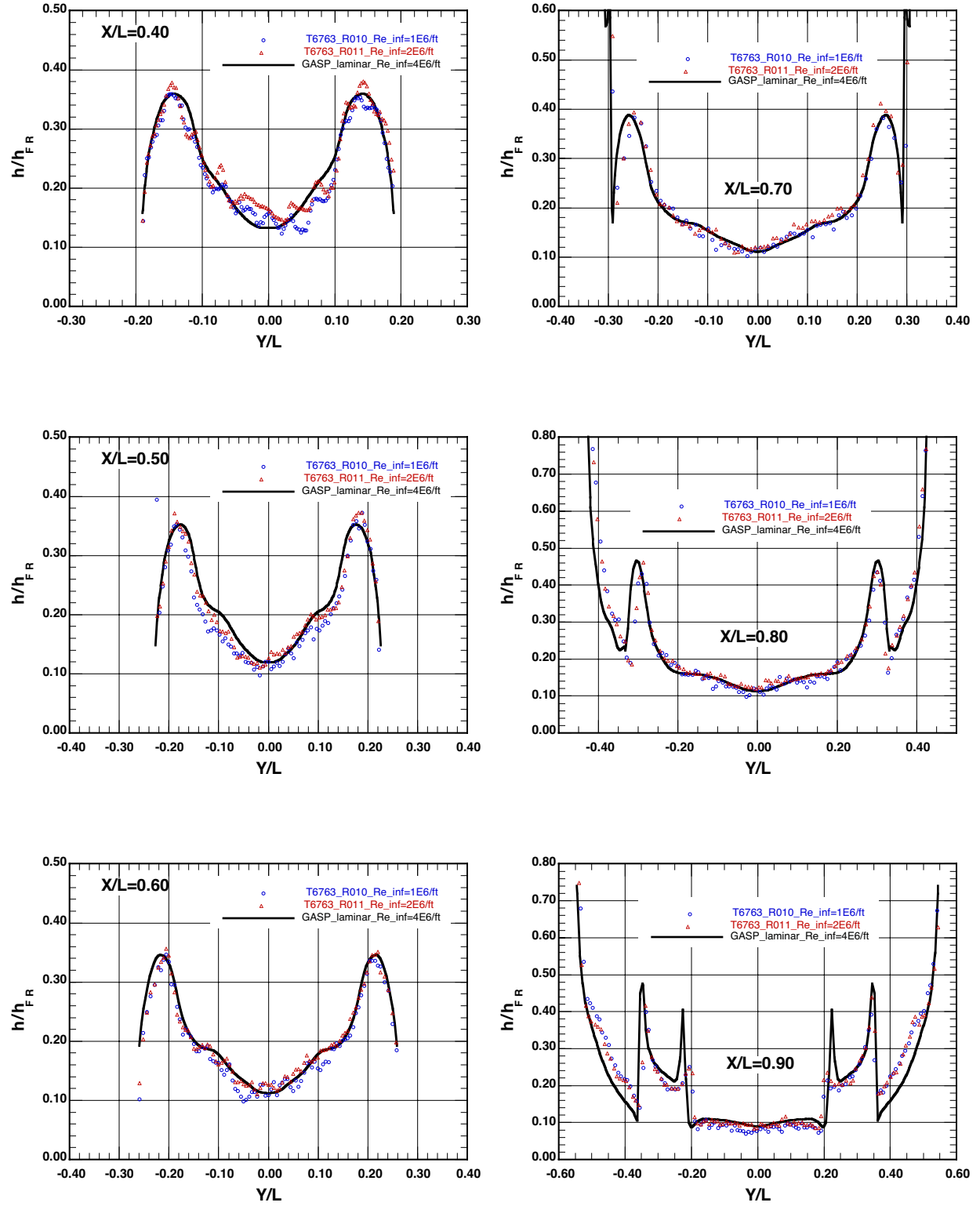
Figure 45. GASP laminar computation versus heating data on bowed panel models at Mach 6, $\alpha = 40°$, $\delta_{BF} = 0°$; axial cuts from $X/L = 0.40$ to $X/L = 0.90$.
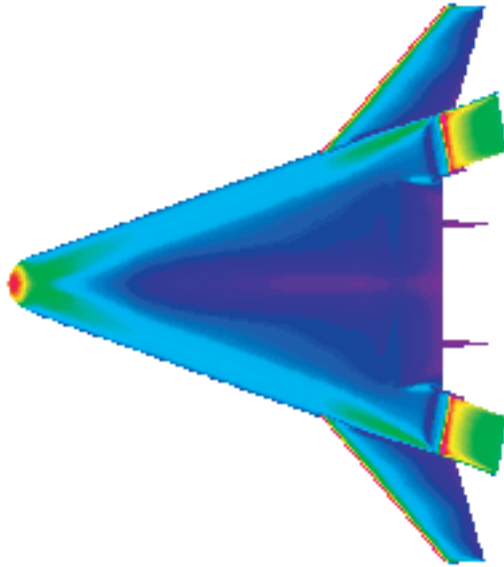
GASP Laminar Solution, Re_inf = 4E6/ft
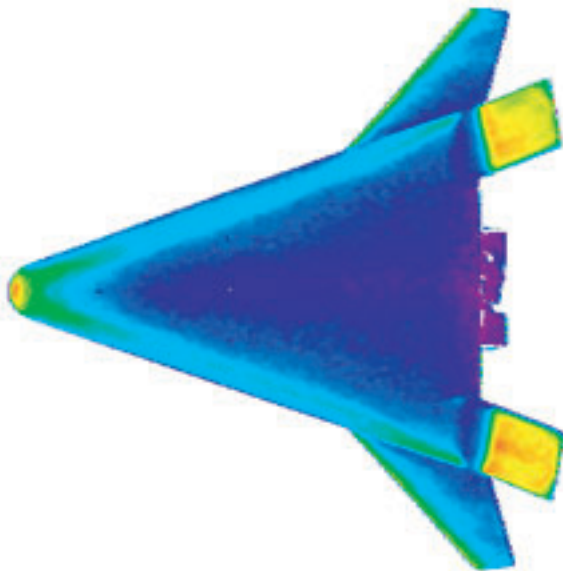
Test 6763, Run 051, Re_inf = 1E6/ft   Test 6763, Run 050, Re_inf = 2E6/ft

h/h_{FR}

0.0   0.25   0.50   0.75   1.00   1.25
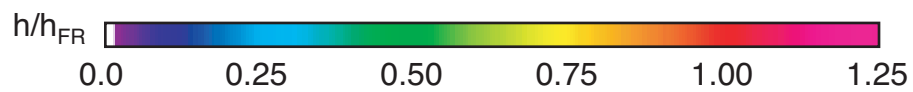
Figure 46. Graphical depiction of GASP laminar solution and heating data on smooth models, windward surface with deflected flaps, Mach 6, $\alpha = 30°$, $\delta_{BF} = 20°$.
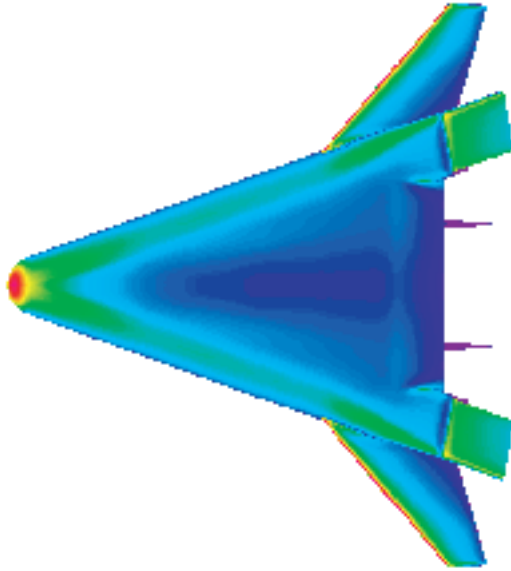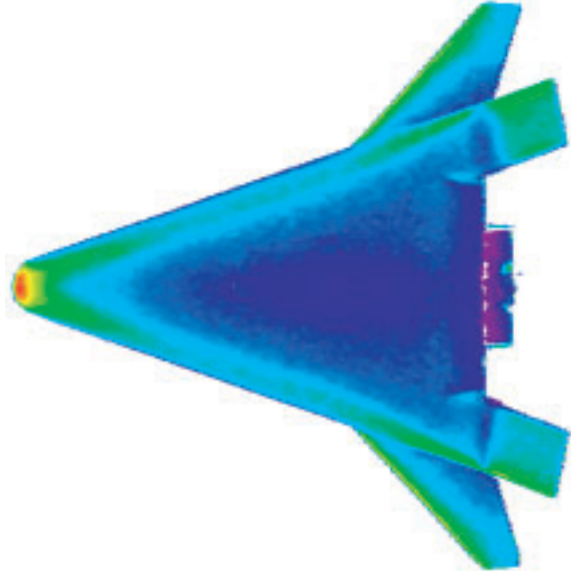
GASP Laminar Solution, Re_inf = 4E6/ft   Test 6763, Run 015, Re_inf = 1E6/ft
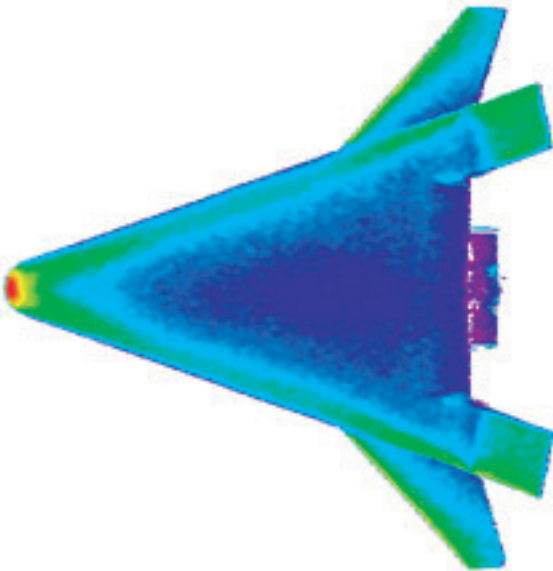
Test 6763, Run 016, Re_inf = 0.5E6/ft   Test 6763, Run 014, Re_inf = 2E6/ft

h/h_{FR}

0.0   0.25   0.50   0.75   1.00   1.25
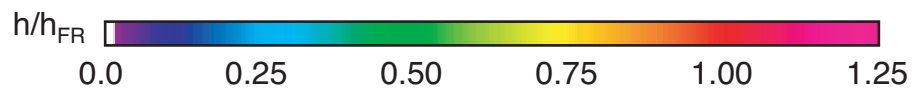
Figure 47. Graphical depiction of GASP laminar solution and heating data on smooth models, windward surface with deflected flaps, Mach 6, $\alpha = 40°$, $\delta_{BF} = 10°$.

GASP Laminar Solution, Re_inf = 4E6/ft   Test 6763, Run 020, Re_inf = 1E6/ft

Test 6763, Run 021, Re_inf = 0.5E6/ft   Test 6763, Run 019, Re_inf = 2E6/ft

h/h_{FR} 0.0   0.25   0.50   0.75   1.00   1.25

Figure 48. Graphical depiction of GASP laminar solution and heating data on smooth models, windward surface with deflected flaps, Mach 6, $\alpha = 40°$, $\delta_{BF} = 20°$.

Figure 49. GASP laminar computation versus heating data on smooth models at Mach 6, $\alpha = 30°$, $\delta_{BF} = 20°$; along chine and onto body flap.
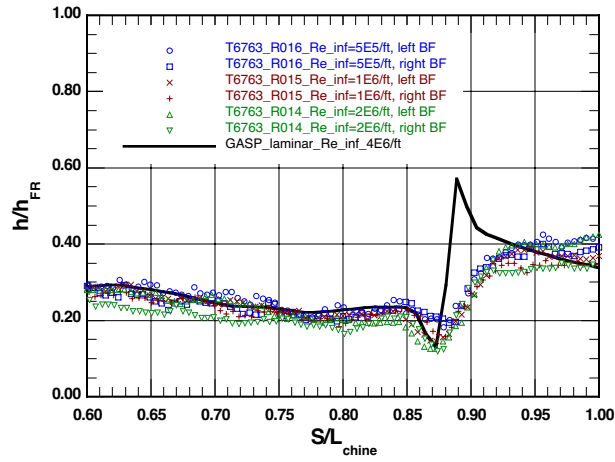
Figure 50. GASP laminar computation versus heating data on smooth models at Mach 6, $\alpha = 40°$, $\delta_{BF} = 10°$; along chine and onto body flap.

Figure 51. GASP laminar computation versus heating data on smooth models at Mach 6, $\alpha = 40°$, $\delta_{BF} = 20°$; along chine and onto body flap.
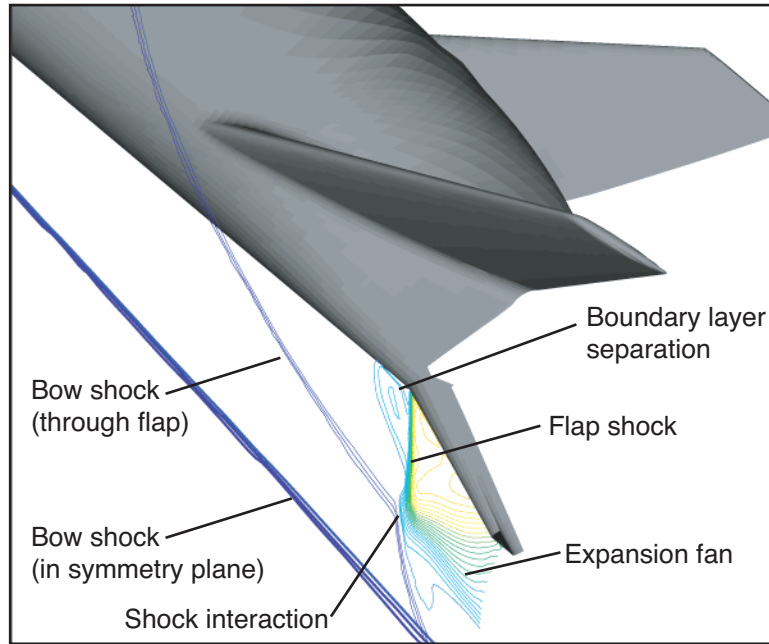
Figure 52. Pressure contours showing shock-shock interaction at Mach 6, $\alpha = 40°$, $\delta_{BF} = 20°$.
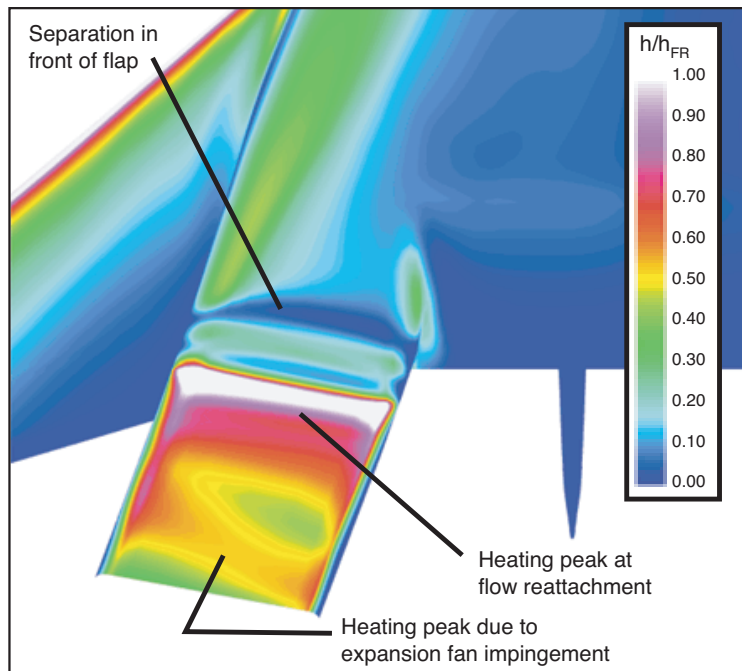
Figure 53. Computed laminar heating distribution showing shock-shock interaction at Mach 6, $\alpha = 40°$, $\delta_{BF} = 20°$.
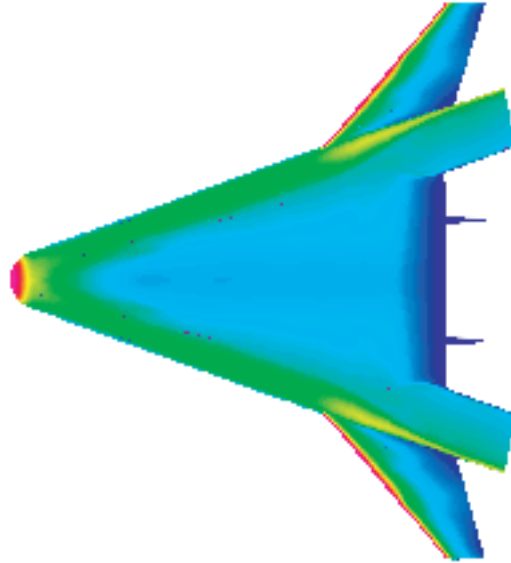
GASP Turbulent Solution, Re_inf = 4E6/ft

Trip locations on models
shown by a "◆" symbol
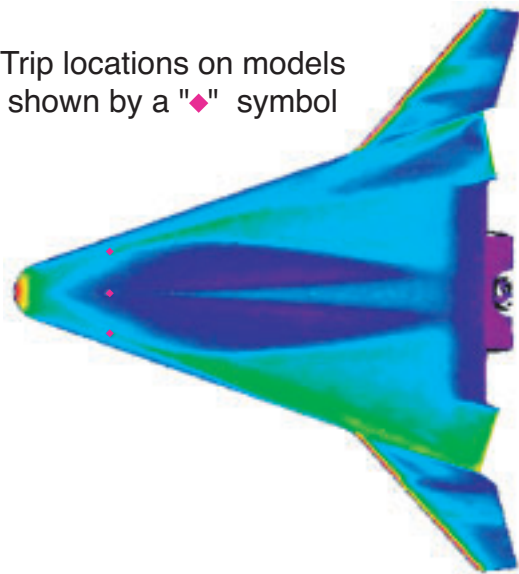
Test 6770, Run 150, Re_inf = 4E6/ft,
3-Trip Array

h/h$_{FR}$

| 0.0 | 0.25 | 0.50 | 0.75 | 1.00 | 1.25 |
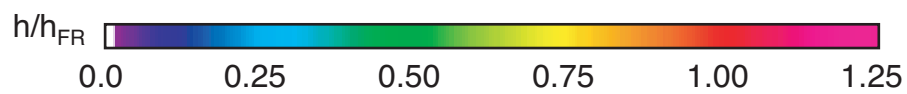
Figure 54. Graphical depiction of GASP turbulent solution and experimental heating data on smooth models with trips, windward surface, Mach 6, $\alpha = 20°$, $\delta_{BF} = 0°$.
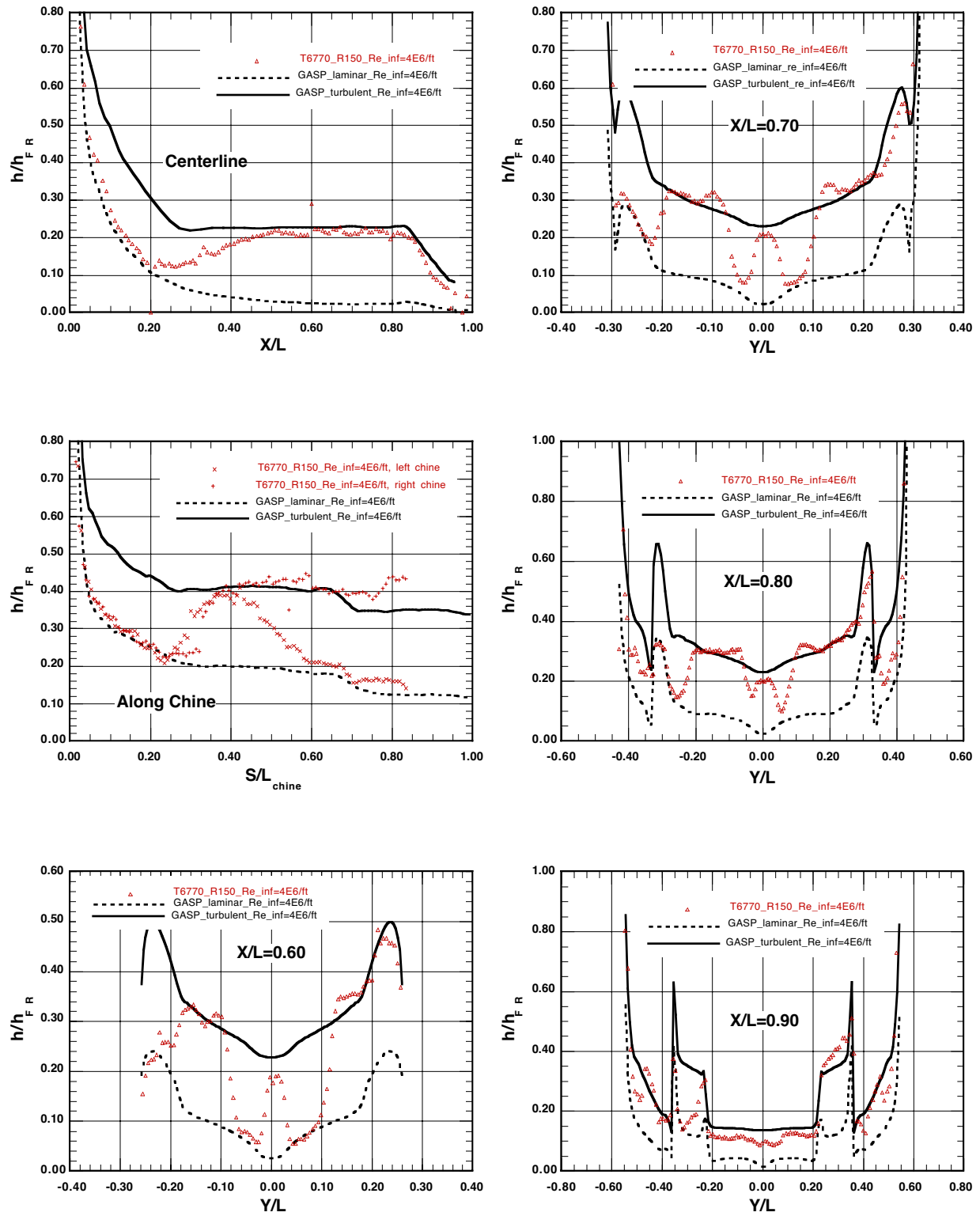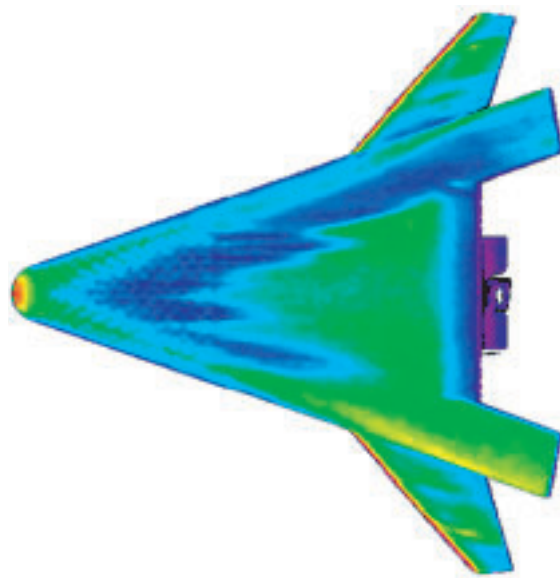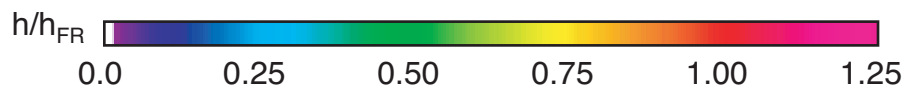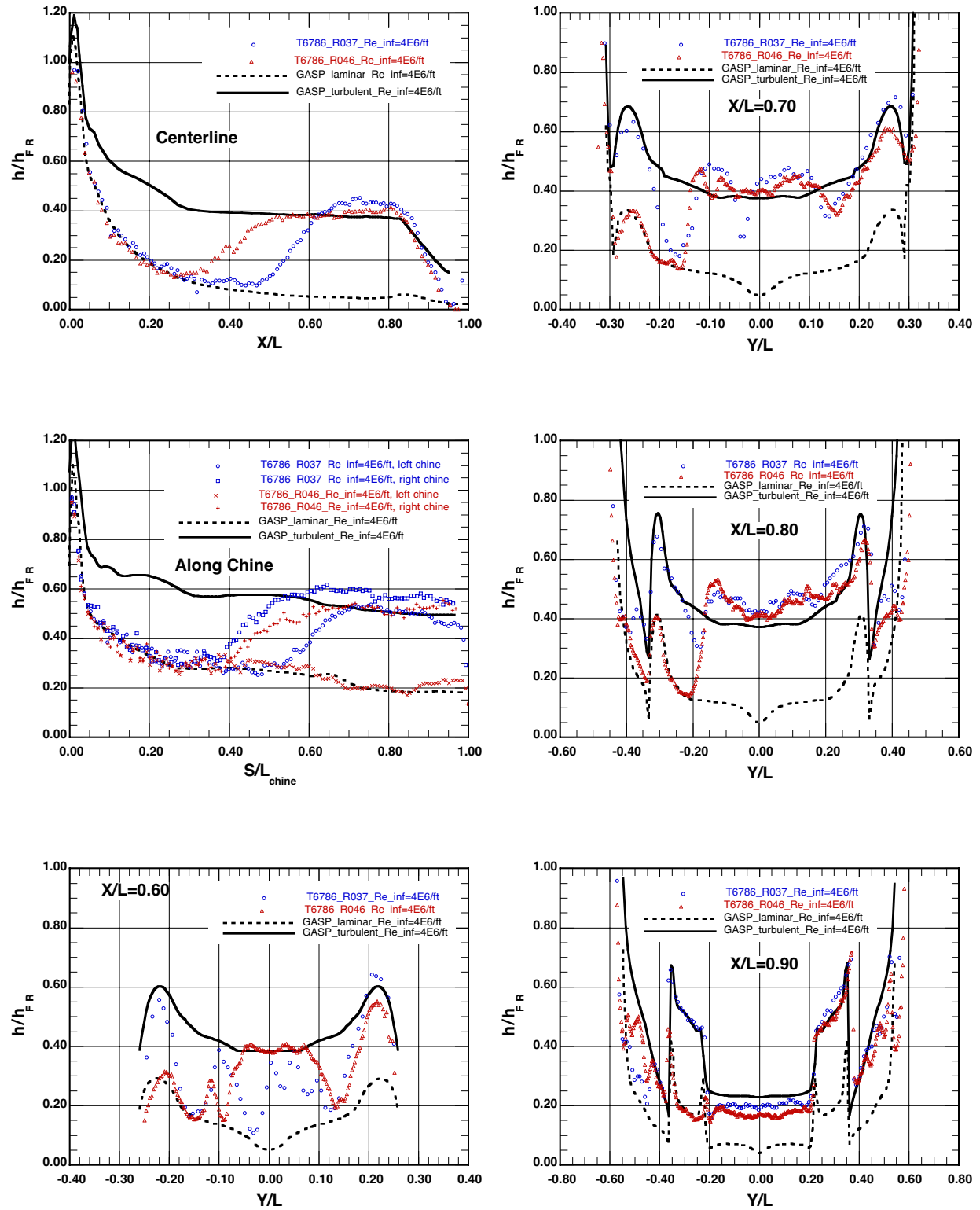
Figure 55. GASP turbulent computation versus heating data (on smooth models with trips) at Mach 6, $\alpha = 20°$, $\delta_{BF} = 0°$; centerline, chine, and axial cuts from $X/L = 0.60$ to $X/L = 0.90$.
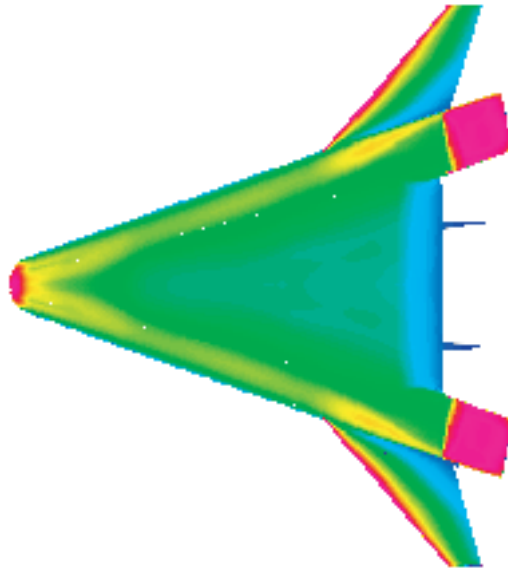
GASP Turbulent Solution, Re_inf = 4E6/ft (body flaps at δ_{BF} = +20-deg)
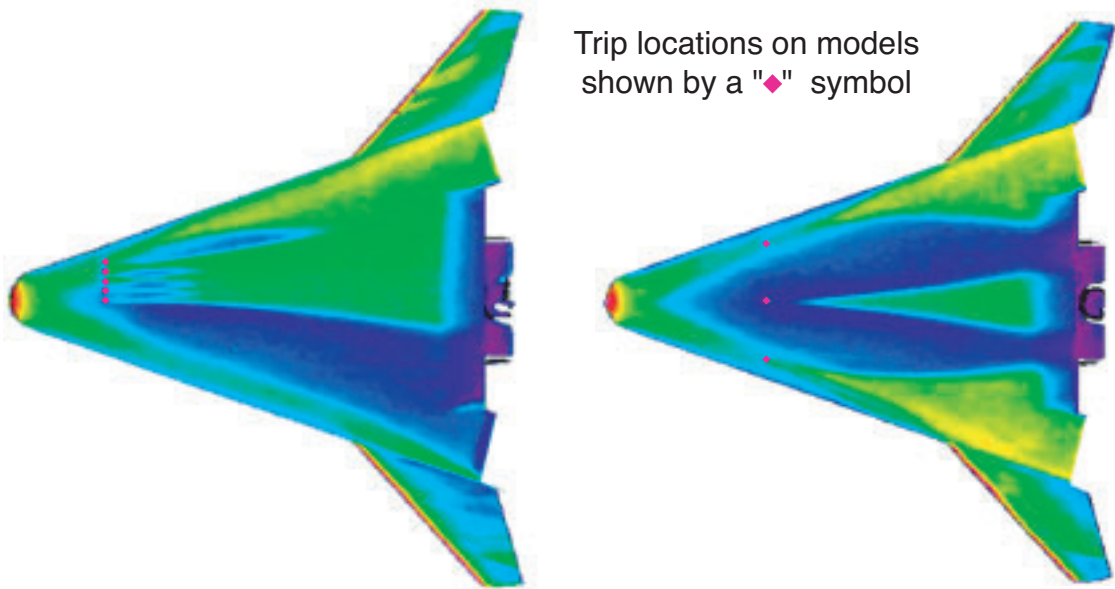
Trip locations on models
shown by a "◆" symbol

Test 6763, Run 175, Re_inf = 4E6/ft,
5-Trip Array on Port Side

Test 6770, Run 062, Re_inf = 4E6/ft,
3-Trip Array

h/h_{FR}

0.0   0.25   0.50   0.75   1.00   1.25
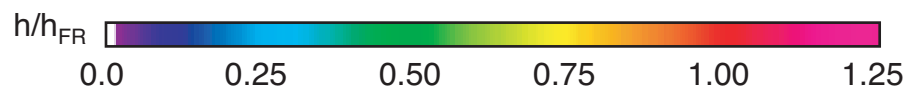
Figure 56. Graphical depiction of GASP turbulent solution and experimental heating data on smooth models with trips, windward surface, Mach 6, $\alpha = 30°$, $\delta_{BF} = 0°$.
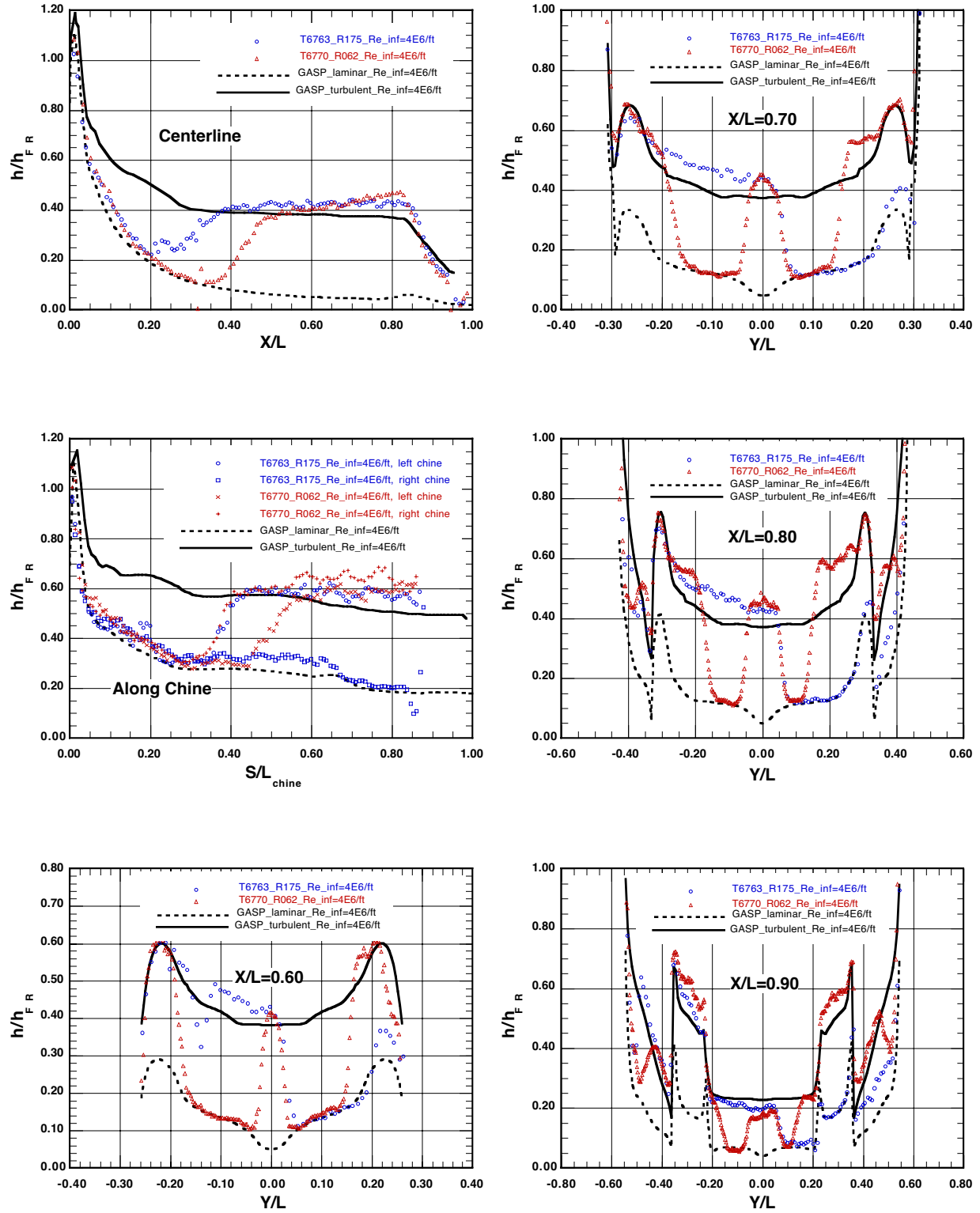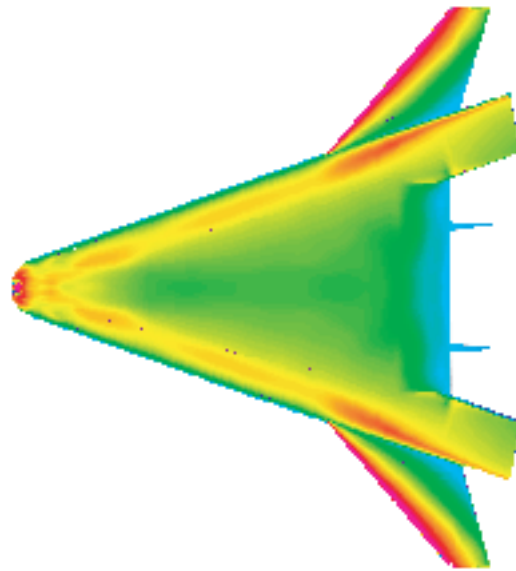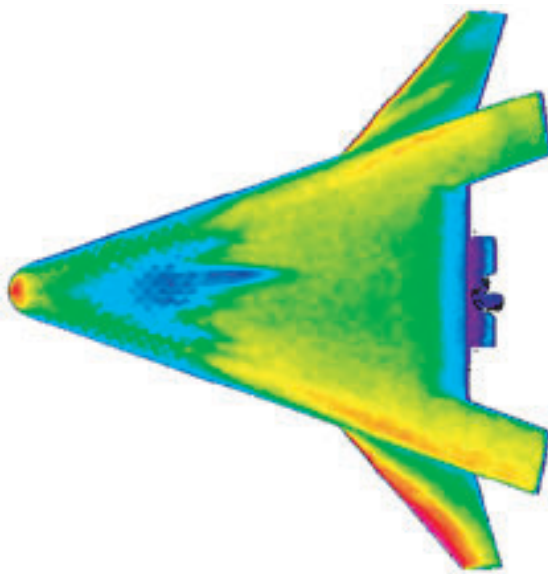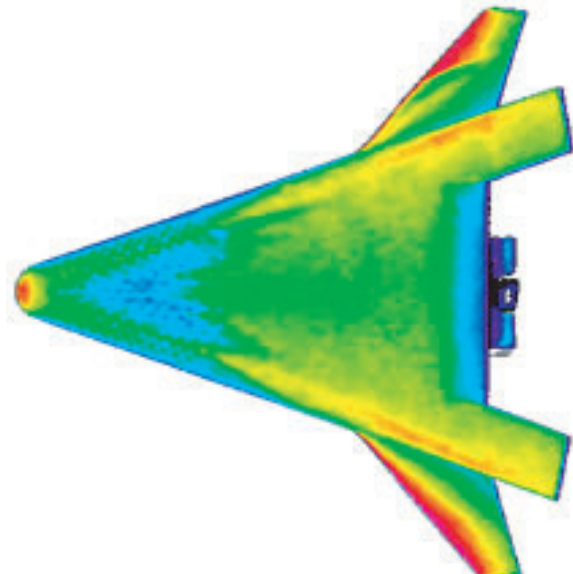
Figure 57. GASP turbulent computation versus heating data (on smooth models with trips) at Mach 6, $\alpha = 30°$, $\delta_{BF} = 0°$; centerline, chine, and axial cuts from $X/L = 0.60$ to $X/L = 0.90$.

GASP Turbulent Solution, Re_inf = 4E6/ft

Trip locations on models
shown by a "♦" symbol

Test 6763, Run 167, Re_inf = 4E6/ft,
5-Trip Array on Port Side

Test 6770, Run 114, Re_inf = 4E6/ft,
3-Trip Array

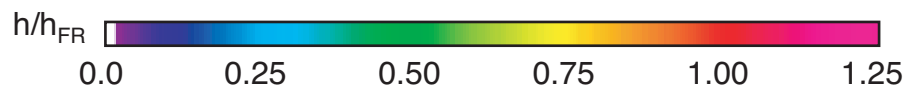h/h_{FR}

0.0   0.25   0.50   0.75   1.00   1.25
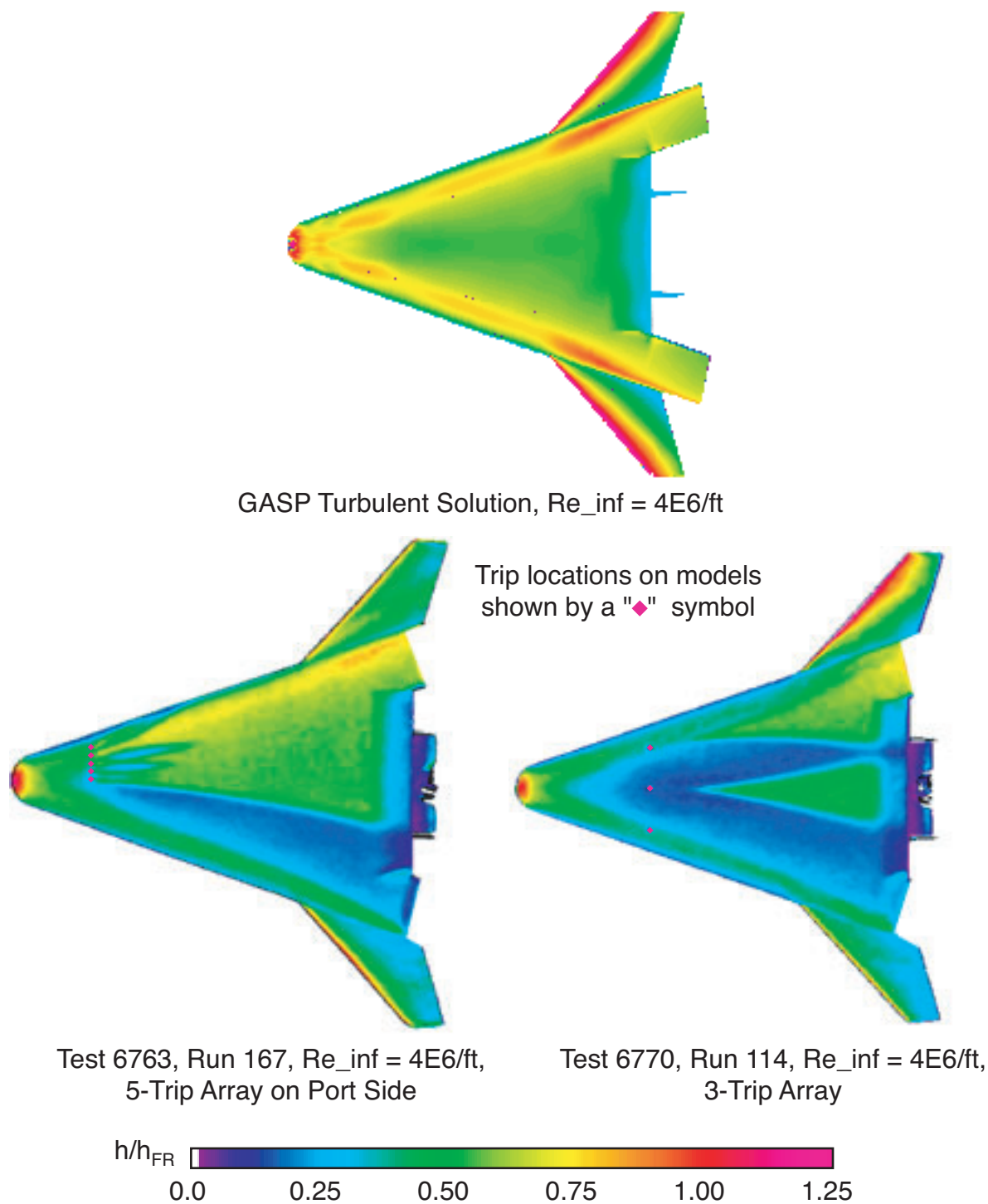
Figure 58. Graphical depiction of GASP turbulent solution and experimental heating data on smooth models with trips, windward surface, Mach 6, $\alpha = 40°$, $\delta_{BF} = 0°$.
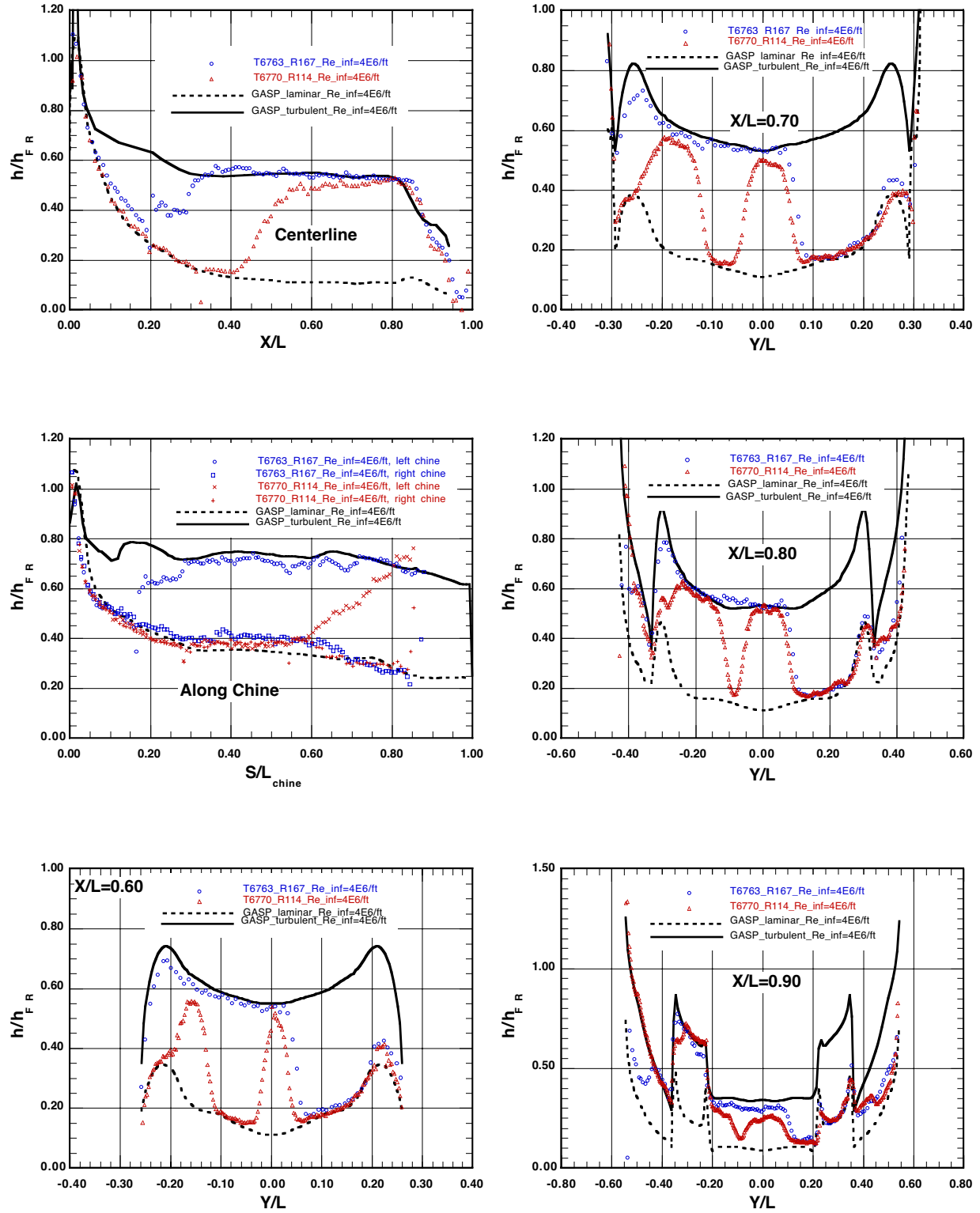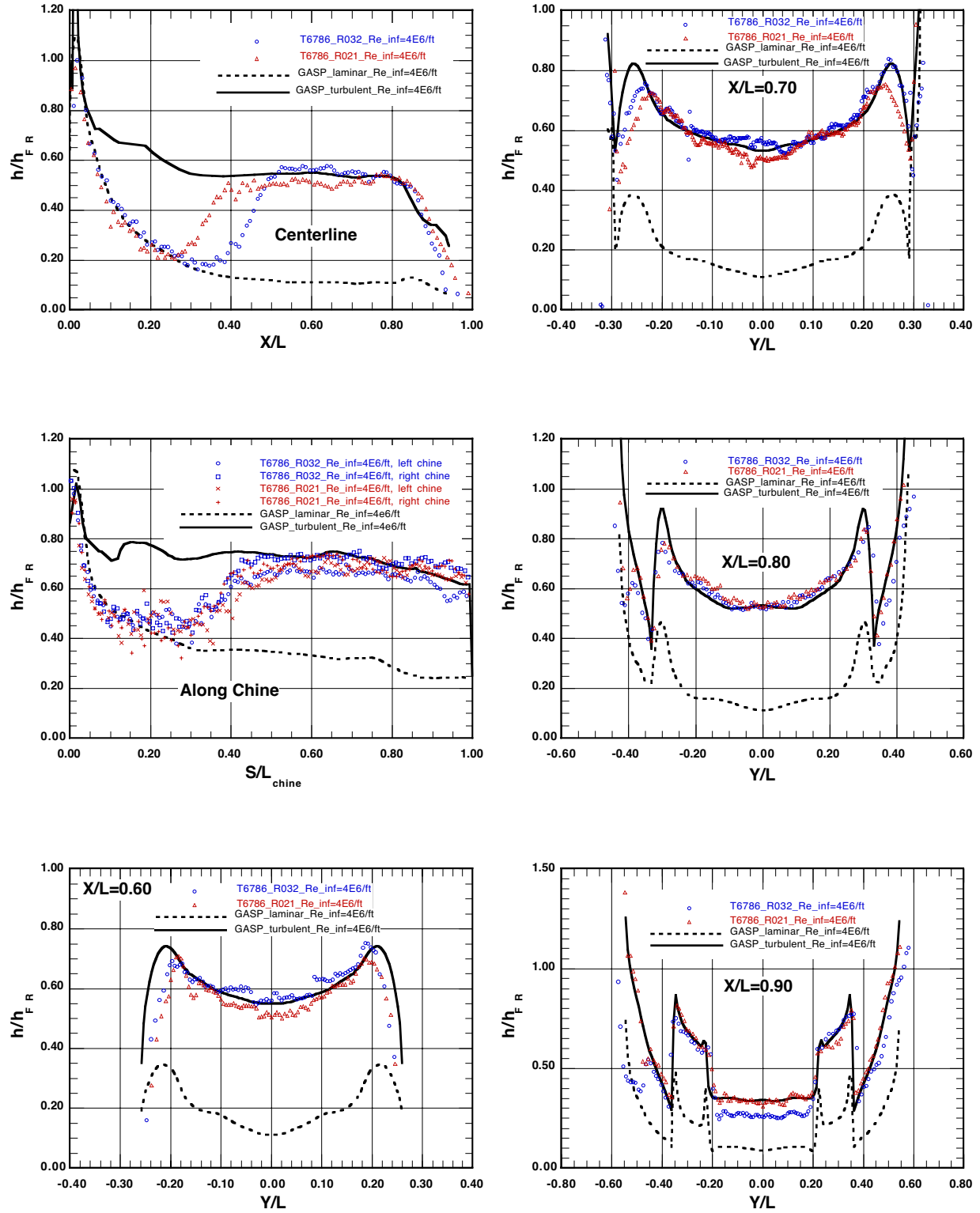
Figure 59. GASP turbulent computation versus heating data (on smooth models with trips) at Mach 6, $\alpha = 40°$, $\delta_{BF} = 0°$; centerline, chine, and axial cuts from $X/L = 0.60$ to $X/L = 0.90$.

Trip locations on models
shown by a "◆" symbol

GASP Turbulent Solution, Re_inf = 4E6/ft

Test 6770, Run 094, Re_inf = 4E6/ft,
3-Trip Array

Test 6763, Run 006, Re_inf = 4E6/ft,
No Trips

Test 6770, Run 125, Re_inf = 4E6/ft,
3-Trip Array

h/h_{FR}

| 0.0 | 0.50 | 1.00 | 1.50 | 2.00 |
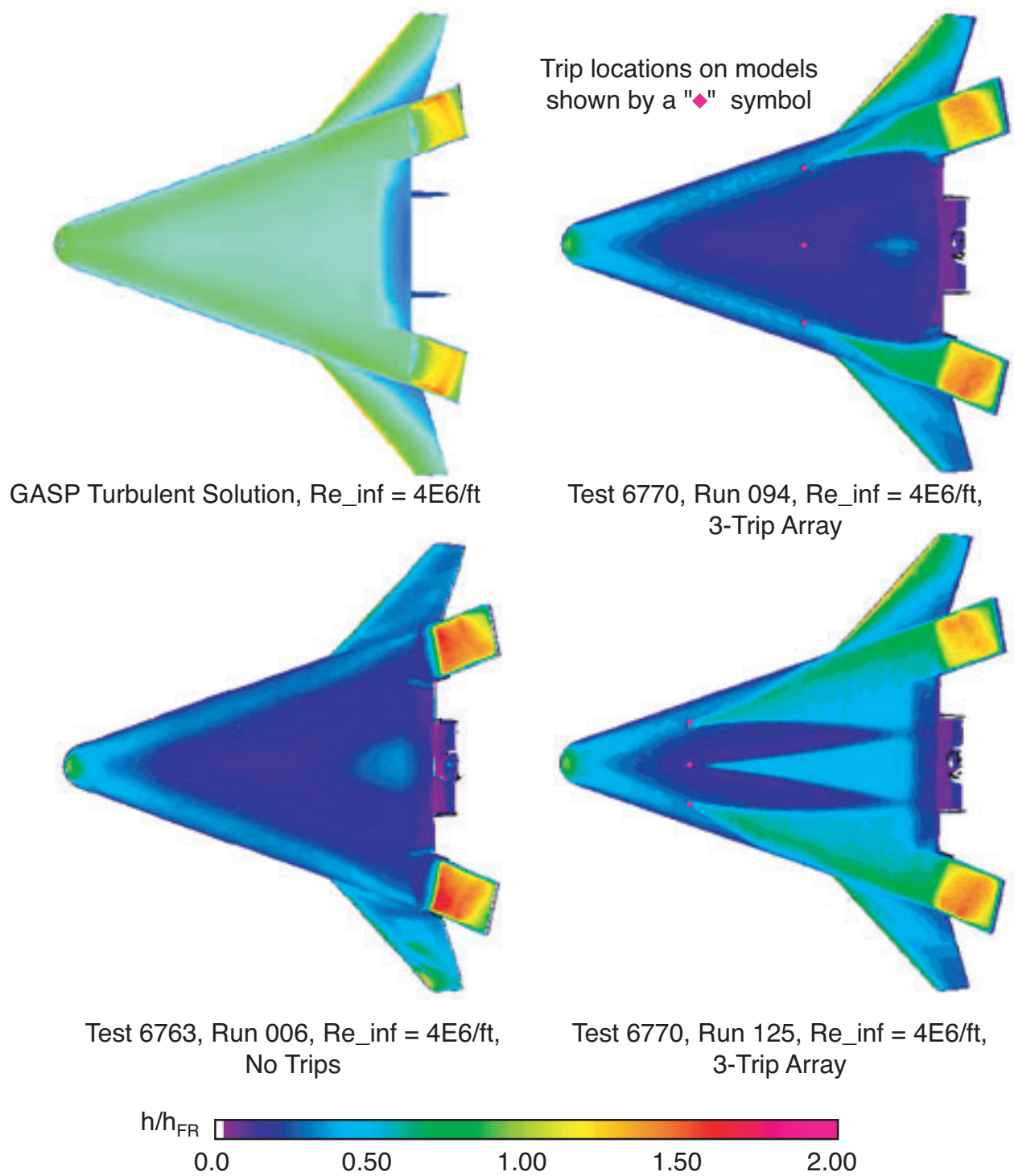
Figure 60. Graphical depiction of GASP turbulent solution and experimental heating data on models with trips, windward surface, Mach 6, $\alpha = 40°$, $\delta_{BF} = 20°$.
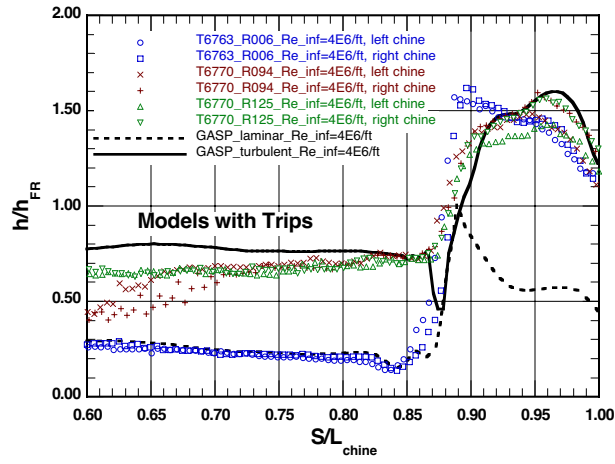
Figure 61. GASP turbulent computation versus heating data on models with trips at Mach 6, $\alpha = 40°$, $\delta_{BF} = 20°$; along chine and onto body flap.
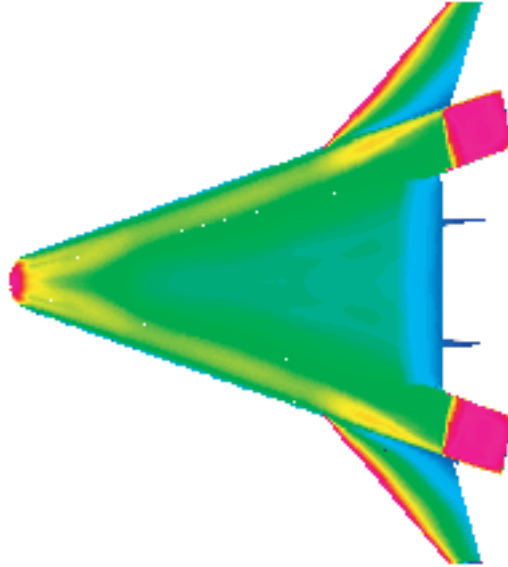
GASP Turbulent Solution, Re_inf = 4E6/ft (body flaps at δ_{BF} = +20-deg)
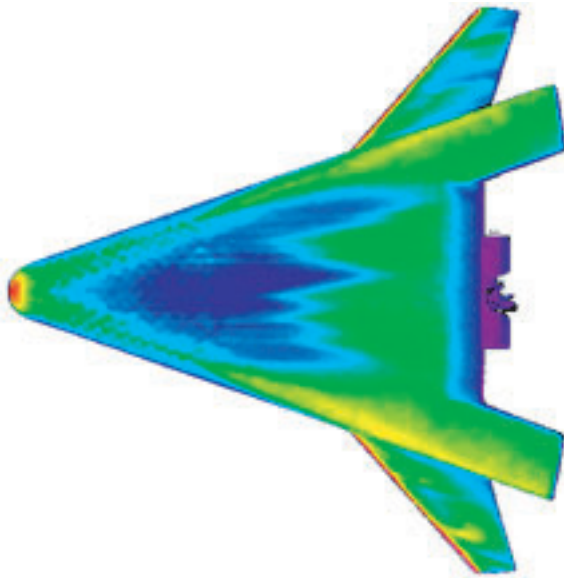
Test 6786, Run 037, Re_inf = 4E6/ft, 0.006" Bowed Panel Array

Test 6786, Run 046, Re_inf = 4E6/ft, 0.008" Bowed Panel Array

h/h_{FR}

| 0.0 | 0.25 | 0.50 | 0.75 | 1.00 | 1.25 |

Figure 62. Graphical depiction of GASP turbulent solution and experimental heating data on models with bowed panels, windward surface, Mach 6, $\alpha = 30°$, $\delta_{BF} = 0°$.

66

Figure 63. GASP turbulent computation versus heating data (on bowed panel models) at Mach 6, $\alpha = 30°$, $\delta_{BF} = 0°$; centerline, chine, and axial cuts from $X/L = 0.60$ to $X/L = 0.90$.

GASP Turbulent Solution, Re_inf = 4E6/ft

Test 6786, Run 032, Re_inf = 4E6/ft,
0.006" Bowed Panel Array

Test 6786, Run 021, Re_inf = 4E6/ft,
0.008" Bowed Panel Array

h/h_{FR}

0.0   0.25   0.50   0.75   1.00   1.25

Figure 64. Graphical depiction of GASP turbulent solution and experimental heating data on models with bowed panels, windward surface, Mach 6, $\alpha = 40°$, $\delta_{BF} = 0°$.

Figure 65. GASP turbulent computation versus heating data (on bowed panel models) at Mach 6, $\alpha = 40°$, $\delta_{BF} = 0°$; centerline, chine, and axial cuts from $X/L = 0.60$ to $X/L = 0.90$.
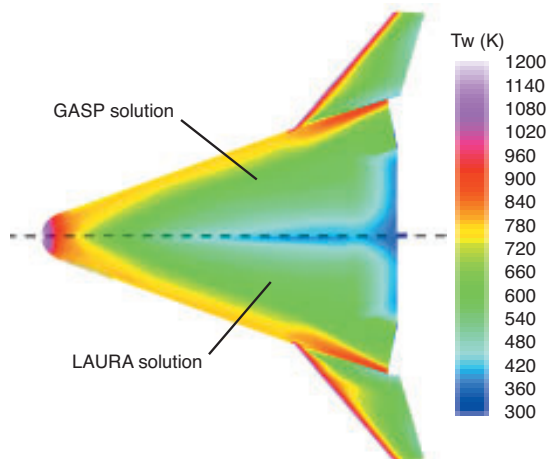
Figure 66. Computed windward surface temperatures for flight case 1; Mach 8.82, $\alpha = 10°$.
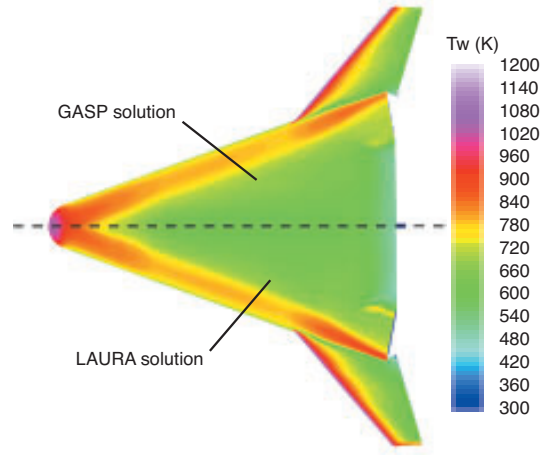
Figure 68. Computed windward surface temperatures for flight case 3; Mach 8.89, $\alpha = 30°$.
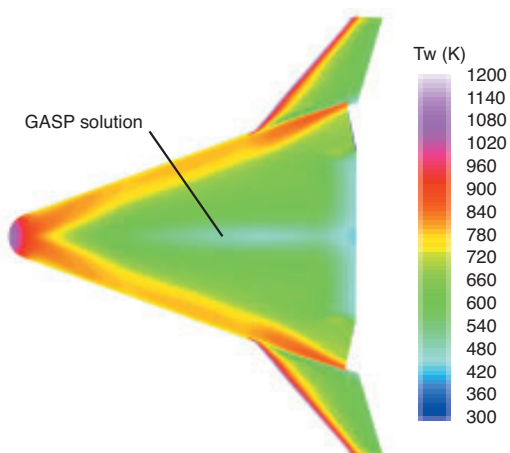
Figure 67. Computed windward surface temperatures for flight case 2; Mach 8.87, $\alpha = 20°$.
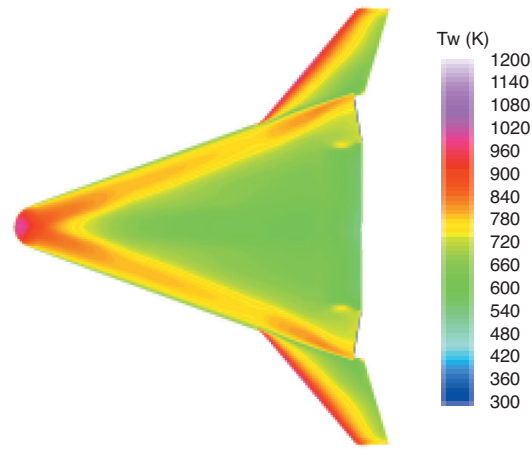
Figure 69. Computed windward surface temperatures for flight case 4; Mach 6.64, $\alpha = 40°$.
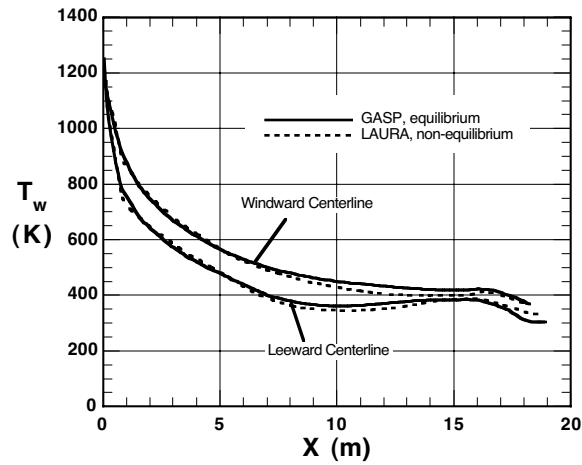
Figure 70. Computed centerline surface temperature distribution for flight case 1; Mach 8.82, $\alpha = 10°$.
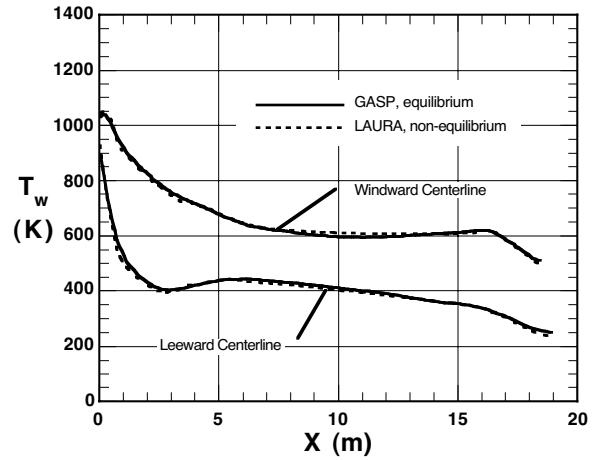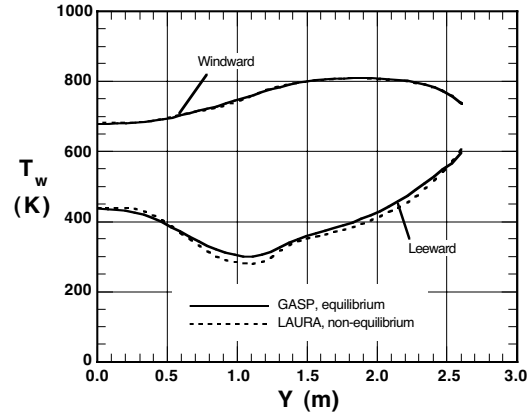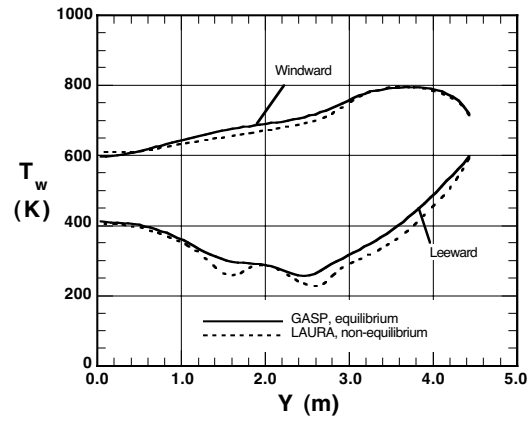

Figure 72. Computed centerline surface temperature distribution for flight case 3; Mach 8.89, $\alpha = 30°$.
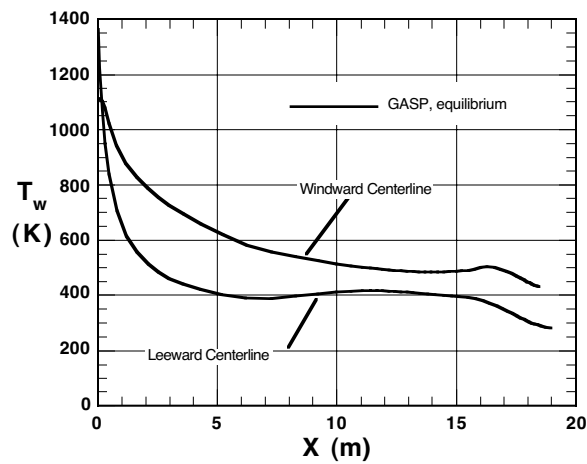
Figure 71. Computed centerline surface temperature distribution for flight case 2; Mach 8.87, $\alpha = 20°$.
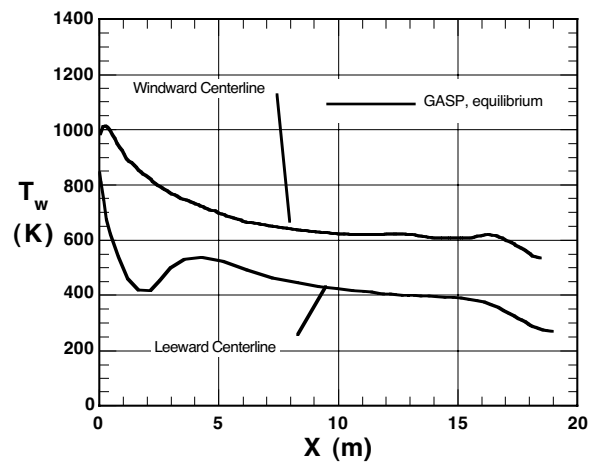
Figure 73. Computed centerline surface temperature distribution for flight case 4; Mach 6.64, $\alpha = 40°$.
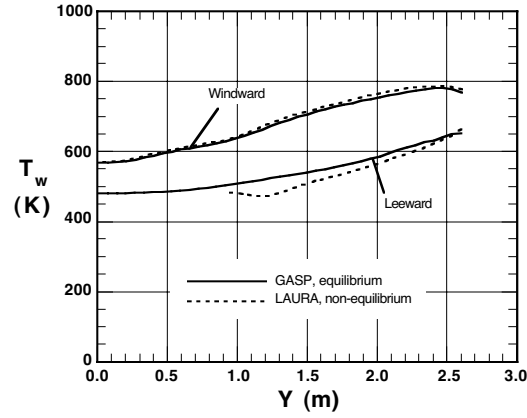
Figure 74. Computed lateral (X = 5.0 m) surface temperature distribution for flight case 1; Mach 8.82, α = 10°.
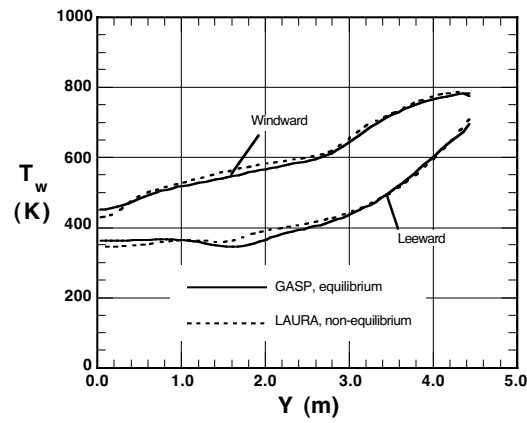
Figure 75. Computed lateral (X = 10.0 m) surface temperature distribution for flight case 1; Mach 8.82, α = 10°.
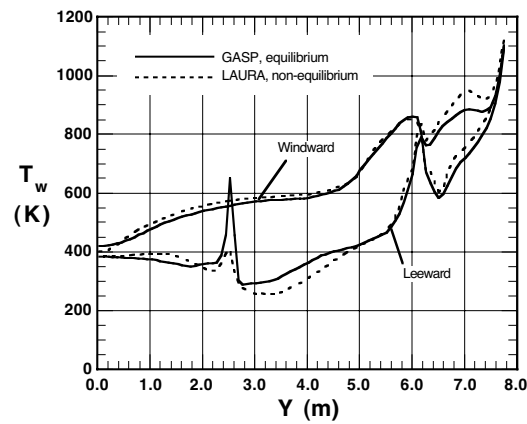
Figure 76. Computed lateral (X = 15.0 m) surface temperature distribution for flight case 1; Mach 8.82, α = 10°.

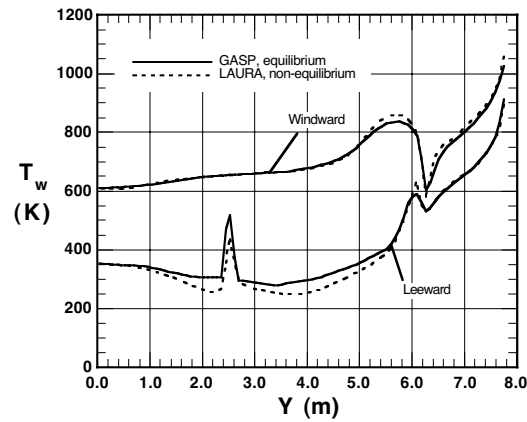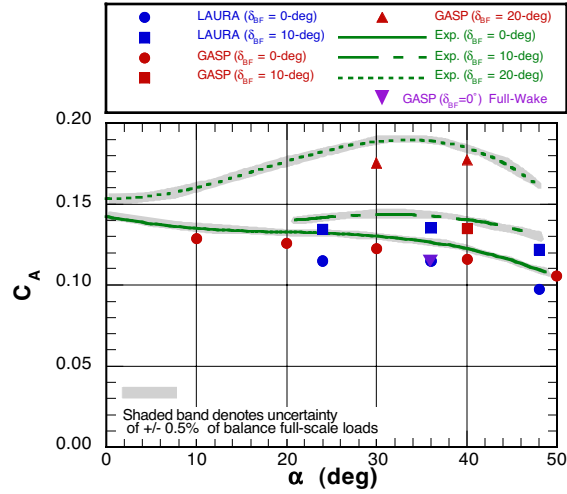Figure 77. Computed lateral (X = 5.0 m) surface temperature distribution for flight case 3; Mach 8.89, α = 30°.

Figure 78. Computed lateral (X = 10.0 m) surface temperature distribution for flight case 3; Mach 8.89, α = 30°.

Figure 79. Computed lateral (X = 15.0 m) surface temperature distribution for flight case 3; Mach 8.89, α = 30°.

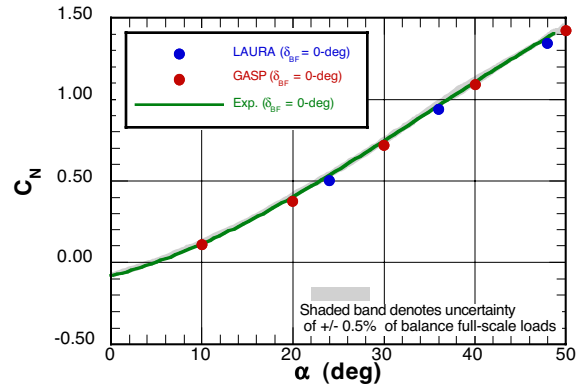Figure 80. Measured and predicted axial force coefficients for Langley 20-Inch Mach 6 Air Tunnel.

Figure 81. Measured and predicted normal force coefficients for Langley 20-Inch Mach 6 Air Tunnel.
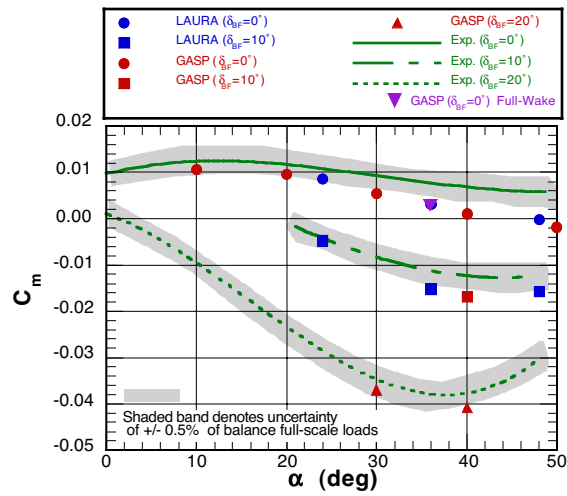
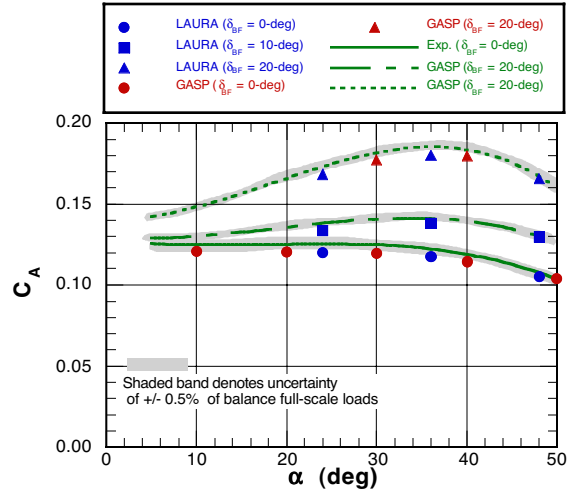Figure 82. Measured and predicted pitching moment coefficients for Langley 20-Inch Mach 6 Air Tunnel.

Figure 83. Measured and predicted axial force coefficients for Langley 31-Inch Mach 10 Air Tunnel.
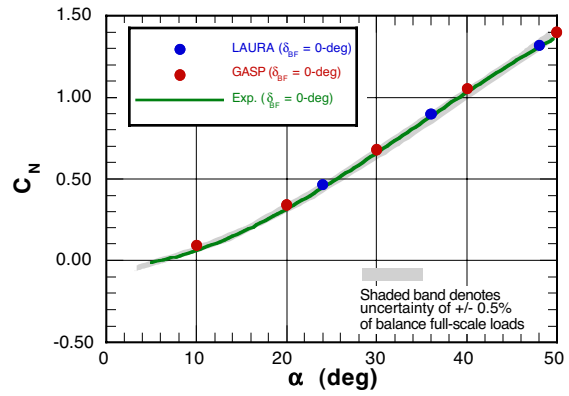

Figure 84. Measured and predicted normal force coefficients for Langley 31-Inch Mach 10 Air Tunnel.
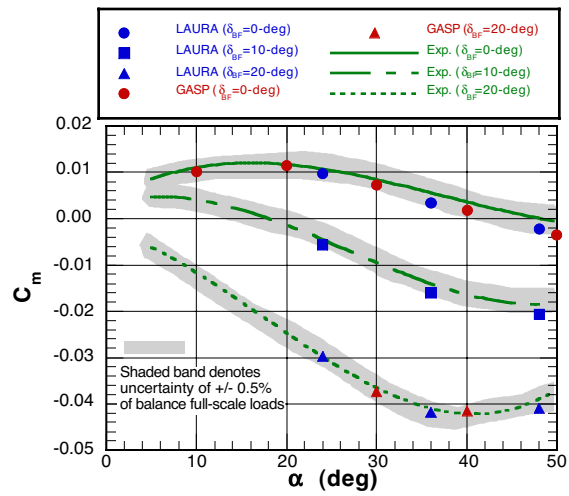

Figure 85. Measured and predicted pitching moment coefficients for Langley 31-Inch Mach 10 Air Tunnel.
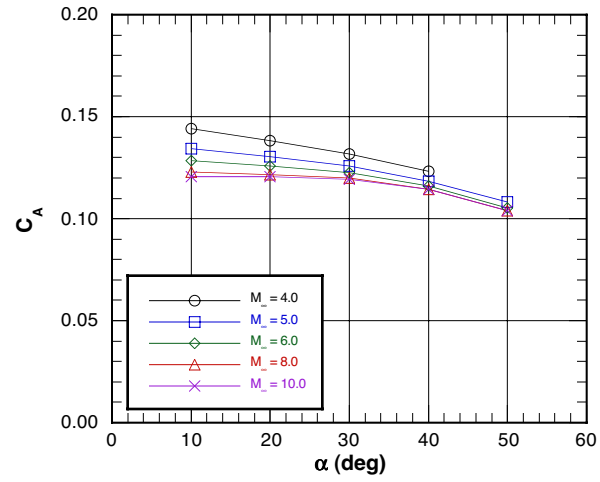
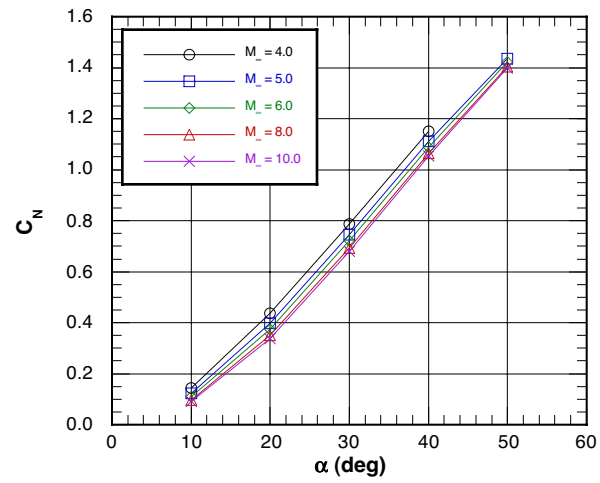Figure 86. Computed variation of axial force coefficient with Mach number and angle of attack.

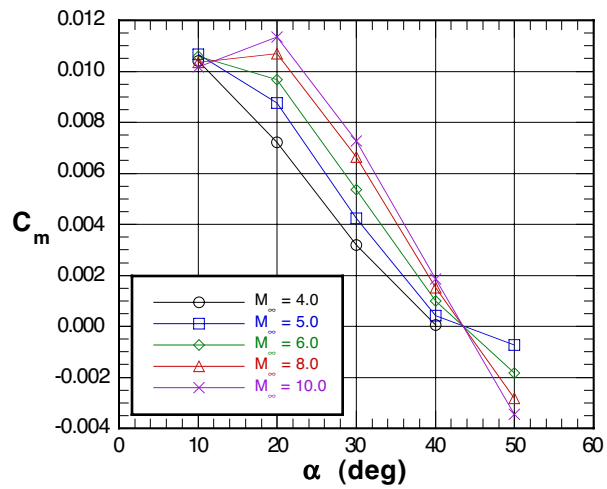Figure 87. Computed variation of normal force coefficient with Mach number and angle of attack.

Figure 88. Computed variation of pitching moment coefficient with Mach number and angle of attack.
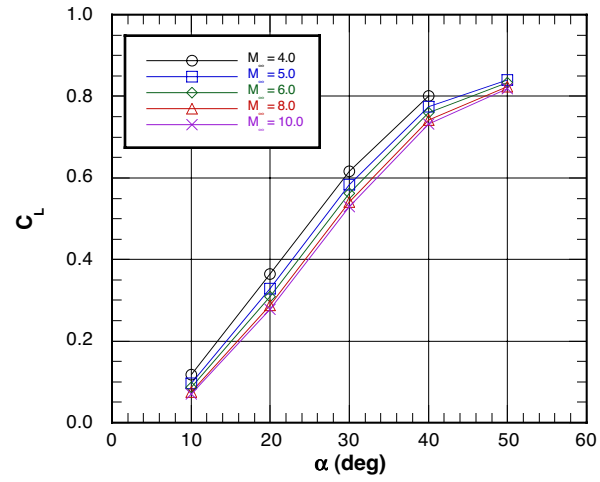
Figure 89. Computed variation of lift coefficient with Mach number and angle of attack.
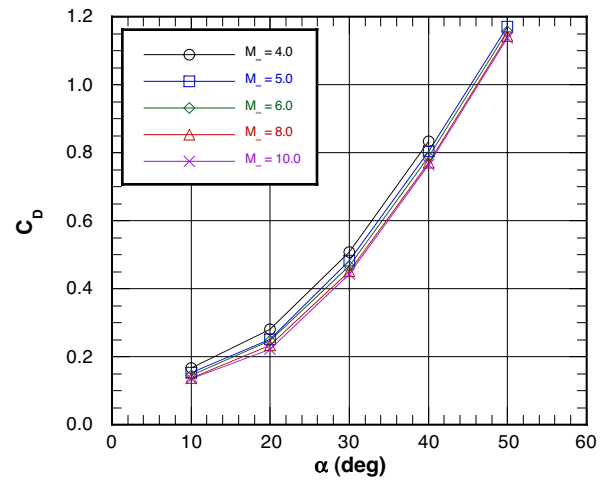

Figure 90. Computed variation of drag coefficient with Mach number and angle of attack.
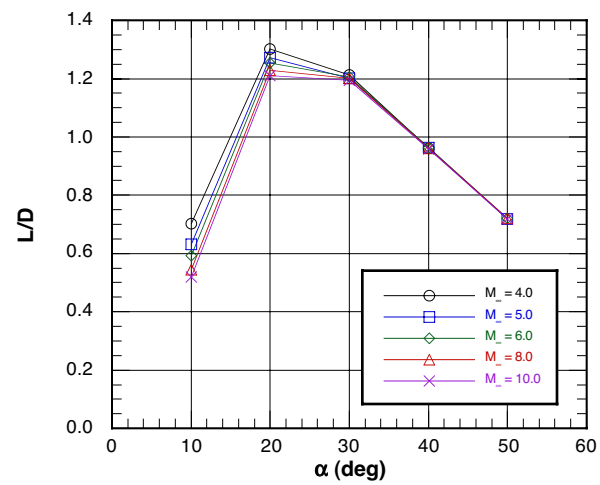

Figure 91. Computed variation of lift-to-drag ratio with Mach number and angle of attack.

77

REPORT DOCUMENTATION PAGE

Form Approved
OMB No. 0704-0188

1. REPORT DATE (DD-MM-YYYY)	2. REPORT TYPE	3. DATES COVERED (From - To)
01- 05 - 2003	Technical Publication	

4. TITLE AND SUBTITLE

X-33 Computational Aeroheating/Aerodynamic Predictions and Comparisons With Experimental Data

5a. CONTRACT NUMBER

5b. GRANT NUMBER

5c. PROGRAM ELEMENT NUMBER

6. AUTHOR(S)

Hollis, Brian R.; Thompson, Richard A.; Berry, Scott A.; Horvath, Thomas J.; Murphy, Kelly J.; Nowak, Robert J.; and Alter, Stephen J.

5d. PROJECT NUMBER

5e. TASK NUMBER

5f. WORK UNIT NUMBER

762-30-51-30

7. PERFORMING ORGANIZATION NAME(S) AND ADDRESS(ES)

NASA Langley Research Center
Hampton, VA 23681-2199

8. PERFORMING ORGANIZATION REPORT NUMBER

L-18254

9. SPONSORING/MONITORING AGENCY NAME(S) AND ADDRESS(ES)

National Aeronautics and Space Administration
Washington, DC 20546-0001

10. SPONSOR/MONITOR'S ACRONYM(S)

NASA

11. SPONSOR/MONITOR'S REPORT NUMBER(S)

NASA/TP-2003-212160

12. DISTRIBUTION/AVAILABILITY STATEMENT

Unclassified - Unlimited
Subject Category 34
Availability: NASA CASI (301) 621-0390   Distribution: Standard

13. SUPPLEMENTARY NOTES

Hollis, Thompson, Berry, Horvath, Murphy, Nowak, and Alter, Langley Research Center.
An electronic version can be found at http://techreports.larc.nasa.gov/ltrs/ or http://techreports.larc.nasa.gov/cgi-bin/NTRS

14. ABSTRACT

This report details a computational fluid dynamics study conducted in support of the phase II development of the X-33 vehicle. Aerodynamic and aeroheating predictions were generated for the X-33 vehicle at both flight and wind-tunnel test conditions using two finite-volume, Navier-Stokes solvers. Aerodynamic computations were performed at Mach 6 and Mach 10 wind-tunnel conditions for angles of attack from 10º to 50º with body-flap deflections of 0º to 20º. Additional aerodynamic computations were performed over a parametric range of free-stream conditions at Mach numbers of 4 to 10 and angles of attack from 10º to 50º. Laminar and turbulent wind-tunnel aeroheating computations were performed at Mach 6 for angles of attack of 20º to 40º with body-flap deflections of 0º to 20º. Aeroheating computations were performed at four flight conditions with Mach numbers of 6.6 to 8.9 and angles of attack of 10º to 40º. Surface heating and pressure distributions, surface streamlines, flow field information, and aerodynamic coefficients from these computations are presented, and comparisons are made with wind-tunnel data.

15. SUBJECT TERMS

X-33; Aeroheating; Aerodynamics; Reusable launch vehicles; Boundary-layer transition

16. SECURITY CLASSIFICATION OF:			17. LIMITATION OF ABSTRACT	18. NUMBER OF PAGES	19a. NAME OF RESPONSIBLE PERSON
a. REPORT	b. ABSTRACT	c. THIS PAGE			STI Help Desk (email: help@sti.nasa.gov)
U	U	U	UU	88	19b. TELEPHONE NUMBER (Include area code) (301) 621-0390

Standard Form 298 (Rev. 8-98)
Prescribed by ANSI Std. Z39.18